

# The Role of Uncompensated Spins in Exchange Biased Systems

INAUGURALDISSERTATION

zur

Erlangung der Würde eines Doktors der Philosophie

vorgelegt der

Philosophisch-Naturwissenschaftlichen Fakultät

der Universität Basel

von

Iris Schmid

aus Adelboden (BE)

Basel, 2006



Genehmigt von der Philosophisch-Naturwissenschaftlichen Fakultät  
auf Antrag der Herren Professoren:

Prof. Dr. H. J. Hug  
Prof. Dr. H.-J. Güntherodt  
Prof. Dr. G. Güntherodt

Basel, den 4. April 2006

Prof. Dr. H.-J. Wirz , Dekan

# Abstract

In the last century, the role of *magnetic materials* has changed drastically. Of all the electronic properties of solids, magnetism maybe became of interest to the widest range of scientists and technologists. In addition to fundamental interests in magnetic properties there is a large and growing technology based interest of the properties of magnetic materials. Quite small improvements in permeability, coercivity or saturation magnetisation can be of great economic significance.

On the other hand, the magnetic properties of *antiferromagnetic materials* were not of technological interest until 1956 where Meiklejohn and Bean reported: “*A new type of magnetic anisotropy has been discovered which is best described as an exchange anisotropy. This anisotropy is the result of an interaction between an antiferromagnetic material and a ferromagnetic material*”. Meiklejohn and Beans discovery was initiated by the observation that the hysteresis loop of a sample of nominal cobalt nanoparticles was shifted along the field axis after cooling in an applied field. It was subsequently established that the particles had been partially oxidised to CoO which is an antiferromagnet.

A biased magnetisation direction in a ferromagnet (FM) provided by an antiferromagnet (AFM), the so-called exchange bias (EB) effect, is nowadays essential to state-of-the-art magnetic read-head technology, highly sensitive magnetic field sensors and MRAM (magneto-resistive random access memory) devices. For the above mentioned technologies, the EB-effect plays a key role even though a complete description of the microscopic coupling mechanism is still missing. It is widely accepted that the origin of the EB-effect can be traced back to the existence of pinned uncompensated spins (UCS) in the antiferromagnet (AFM) or at its interface. Such UCS have been observed by various experimental techniques. In a simple extension of the model originally proposed by Meiklejohn and Bean, the observed small size of the exchange bias field could be related to pinned UCS. The compensated interfacial spins and the rotating (non-pinned) UCS were found not to contribute to the exchange bias effect. However, the understanding of the underlying mechanism is still clouded by contradictory reports: For example, both a parallel as well as an antiparallel orientation of the UCS relative to the magnetization direction of the ferromagnet were reported for systems containing the same AFM and FM materials.

In this thesis, two different EB-systems were investigated by low-temperature magnetic force microscopy (MFM) and vibrating sample magnetometry (VSM). These complementary experimental techniques allow us to image the spatial distribution, orientation and density of the UCS at nanometer scale (MFM) and to determine their orientation and density in various externally applied magnetic fields (VSM). Different magnetisation his-

tories in magnetometry and MFM measurements are used advantageously to demonstrate the co-existence of pinned UCS that are parallel and antiparallel to the cooling field in metallic (IrMn) and oxidic (CoO) EB-systems. We further conclude that the EB-effect is a result of pinned interfacial UCS, which are antiparallel to the FM spins. The often observed positive vertical shift of the magnetisation loop after field cooling is due to pinned UCS that align parallel to the cooling field, but are of little importance for the EB-effect itself.

Furthermore we present a MFM study of an AFM/FM bilayer which, for the first time, reveals that the UCS-density undergoes strong variations on single grain scale. The large variations of the UCS-density observed on single grain scale are explained within a simple statistical approach. The transmission electron microscopy (TEM) images reveal that our sample satisfies the conditions of the model proposed by Takano et al.: sharp grain interfaces with only few crystalline, atomic steps. The small number of steps per grain generates a limited distribution of terrace sizes which leads to poor statistics and as a consequence to a strong local variation of the UCSD, as indeed measured.

Quantitatively, three different areas can be distinguished: (1) regions with UCS aligned antiparallel to the FM. (2) regions where no UCS exist. (3) regions with UCS aligned parallel to the FM. Note that the regions (1) dominate such that on average the UCS are aligned antiparallel to the FM spins. It is interesting to see that in an applied field, the FM domains always “retract” to the regions (1), containing the UCS aligned antiparallel to the FM, avoiding the regions (3). The fact that the FM domains retract from these areas suggests that the locations with parallel coupling of the UCS exhibit a reduced exchange coupling strength compared to the antiparallel coupled UCS. In addition, they seem to weaken the overall exchange bias field and are thus defined as anti-biasing regions.

Microscopically, the observed anti-biasing regions are explained by a direct coupling between neighbouring AFM grains. TEM images show a wide range of grain boundary tilt-angles. We thus expect in some cases a strong direct coupling between AFM grains (small tilt angles), in others we expect decoupled or weakly coupled grains (large tilt angles). We suggest that a strong direct coupling between neighbouring AFM grains may lead to the observed anti-biasing regions. From this simple picture we conclude that sophisticated grain boundary engineering leading to decoupled AFM grains, is one possible way to increase the EB effect. For instance we propose the co-deposition of Cr and Co for the AFM layer. The segregation of Cr along the boundaries would then lead to decoupled grains.

This work may provide guidelines for the design of experiments which correctly determine the densities of those UCS that do contribute to the EB-effect. A considerably improved microscopic understanding of the exchange coupling in polycrystalline thin films raises the possibility of an enhancement of the EB-effect by an order of magnitude.

# Contents

<b>Abstract</b>	<b>ii</b>
<b>1 Introduction and Outline</b>	<b>1</b>
<b>2 Introduction to the Exchange Bias Effect</b>	<b>4</b>
2.1 History and Phenomenology . . . . .	4
2.1.1 Hysteresis Loop Shift and Unidirectional Anisotropy . . . . .	7
2.1.2 Rotational Hysteresis . . . . .	8
2.1.3 Training Effect . . . . .	9
2.1.4 Uncompensated Spins and Vertical Hysteresis Loop Shift . . . . .	10
2.2 Theoretical Models . . . . .	14
2.2.1 Rigid Antiferromagnet Model: Meiklejohn and Bean . . . . .	14
2.2.2 Uncompensated Interfacial AFM Spins Model: Takano et al. . . . .	16
2.2.3 Training Effect Model: Zhang et al. . . . .	18
<b>3 Instrumentation and Methods</b>	<b>21</b>
3.1 Magnetic Force Microscopy: MFM . . . . .	21
3.1.1 The Low Temperature Scanning Force Microscope: LTSFM . . . . .	22
3.2 MFM Operation Modes . . . . .	24
3.2.1 Modelling Dynamic Force Microscopy . . . . .	25
3.3 Contrast Formation in MFM . . . . .	27
3.3.1 Magnetic Stray Field Calculation . . . . .	28
3.3.2 Computing the Force on the Magnetic Tip . . . . .	30
3.3.3 Calibration of an MFM Tip . . . . .	32
3.4 Vibrating Sample Magnetometer: VSM . . . . .	33
3.5 Transmission Electron Microscopy: TEM . . . . .	35
<b>4 Improvement of Methods: Hardmagnetic MFM-Tips</b>	<b>36</b>
4.1 Experiment and Results . . . . .	37
4.1.1 Tip Preparation . . . . .	37
4.1.2 MFM Measurements on Harddisc Sample . . . . .	37
4.2 Characterisation of the Magnetic Coating . . . . .	42
4.2.1 Hysteresis Loop Measurements . . . . .	43
4.3 Simulation of the Modification of the Tip Magnetisation . . . . .	44

<b>5 Experiments and Results</b>	<b>47</b>
5.1 Introduction . . . . .	47
5.2 Model Systems and Sample Characterisation . . . . .	48
5.2.1 Macroscopic Sample Structure . . . . .	49
5.2.2 Microscopic Sample Structure by TEM . . . . .	52
5.2.3 Magnetometry Experiments . . . . .	52
5.3 The Role of Uncompensated Spins . . . . .	56
5.3.1 MFM on Multilayer Samples . . . . .	58
5.3.2 New Microscopic Model Based on our Experimental Data . . . . .	65
5.3.3 Verification of the New Microscopic Model . . . . .	67
5.3.4 Determination of the Averaged UCS-Density in the AFM . . . . .	69
5.4 The Local Distribution of the Uncompensated spins . . . . .	73
5.4.1 MFM Images of the CoO/CoPt-Singlelayer Sample . . . . .	73
5.4.2 Determination of the Local Uncompensated Spin Density in the AFM	76
5.4.3 Interpretation of High UCS-Density and Antibiasing Regions . . . . .	78
<b>6 Summary and Conclusions</b>	<b>81</b>
<b>Bibliography</b>	<b>95</b>
<b>List of Symbols &amp; Abbreviations</b>	<b>95</b>
<b>Acknowledgements</b>	<b>95</b>
<b>Scientific Publications</b>	<b>95</b>
<b>Curriculum Vitae</b>	<b>95</b>

# Chapter 1

## Introduction and Outline

It first started when ferrites were discovered thousands of years ago. Large deposits were found in the district of Magnesia in Asia Minor, giving the mineral's name of magnetite ( $\text{Fe}_3\text{O}_4$ ). The magnetic compass, an old Chinese invention, was probably first made in China during the Qin dynasty (221-206 B.C.). Chinese fortune tellers used magnetite to construct their fortune telling boards. Eventually someone noticed that magnetite was better at indicating real directions, leading to the first compasses which were designed on a square slab which had markings for the cardinal points and the constellations. The first person recorded to have used the compass as a navigational aid was Zheng He (1371-1435), from the Yunnan province in China, who made seven ocean voyages between 1405 and 1433. In 1600 William Gilbert published *De Magnete*, a paper on magnetism, about the use and properties of Magnetite. In 1819, Hans Christian Oersted reported that when an electric current in a wire was applied to a magnetic compass needle, the magnet was affected - and so electromagnetism was discovered.

In the last century, the role of magnetic materials has changed drastically: of all the electronic properties of solids, magnetism has become interesting to the widest range of scientists and technologists. In addition to fundamental interests in magnetic properties there is a large and growing technology based interest of the properties of magnetic materials. Quite small improvements in permeability, coercivity or saturation magnetisation can be of great economic significance.

On the other hand, the magnetic properties of antiferromagnetic materials were not of technological interest until 1956: Meiklejohn and Bean reported [1, 2] "*A new type of magnetic anisotropy has been discovered which is best described as an exchange anisotropy. This anisotropy is the result of an interaction between an antiferromagnetic material and a ferromagnetic material*". Meiklejohn and Beans discovery was initiated by the observation that the hysteresis loop of a sample of nominal cobalt nanoparticles was shifted along the field axis after cooling in an applied field. It was subsequently established that the particles had been partially oxidised to CoO which is an antiferromagnet [3].

In 1988, an effect called giant magnetoresistance (GMR) was discovered, independently by Baibich et al. in Paris [4] and Binasch et al. in Jülich [5]. The effect consists of a dramatic change of the resistance of certain materials as a magnetic field is applied. It is described as *giant* since it was a much larger effect than had ever been previously seen in metals. It generated interest from both physicists and device engineers, as there is new

physics to be investigated and huge technological applications in magnetic recording [6, 7] and magnetic field sensors [8]. IBM were first to market with read/write heads based on GMR technology although today all disk drives make use of this technology.

In 2000, IBM and Infineon established a joint MRAM (magnetoresistive random access memory) development program. MRAM is a method of storing data bits using magnetic charges instead of the electrical charges used by DRAM (dynamic random access memory). Conventional random access memory (RAM) computer chips store information as long as electricity flows through them. Once power is turned off, the information is lost unless it has been copied to a hard drive or floppy disk. MRAM, however, retains data after a power supply is cut off. Replacing DRAM with MRAM could prevent data loss, enable computers to start faster while consuming less battery power and permit the storing of greater amounts of data [9, 10]. For the above mentioned technologies, exchange biasing plays a key role and is widely applied. However, a complete description of the microscopic coupling mechanism and quantitatively satisfactory models are still missing. The spin orientation on each side of the antiferromagnet/ferromagnet interface is considered as a key element in exchange biased systems and is one piece of information which is still unclear. It is widely accepted that uncompensated spins (UCS) in the antiferromagnet or at the antiferromagnet/ferromagnet interface are responsible for the exchange bias effect [11, 12]. Several experiments have proven the existence of UCS [13, 14, 15, 16, 17, 18, 19]. However, these experiments give conflicting results on the orientation of the UCS relative to the ferromagnetic magnetisation.

In this work, we used high resolution magnetic force microscopy (MFM) [20] and classical magnetometry techniques to visualise and to quantify the uncompensated spins at the ferromagnet/antiferromagnet interface which are believed to play a key role in the exchange bias effect. The MFM is a member of the scanning force microscope (SFM) family [21], developed for the measurement of magnetic forces between a sensor and a magnetic sample. It uses a cantilever with a sharp tip carrying a magnetic moment as a force sensor. The first successful measurements with an MFM were performed only three years after the invention of the SFM [22, 23] and the first important results published were studies of magnetic recording media [24]. The improvement in quality of the instruments as well as the measurement methods have allowed the development of procedures to quantitatively understand the measurement contrast. A very reliable method for the calibration of an MFM tip was developed by van Schendel et al. [25, 26, 27] in order to determine the sample stray field from MFM data.

Based on the quantitative analysis of magnetic force microscopy data acquired on exchange biased ferromagnetic/antiferromagnetic sandwiches, a considerably improved fundamental understanding of magnetic exchange coupling raises the possibility of an enhancement of the exchange bias effect by an order of magnitude.

### **Outline of the Thesis**

In the first chapter of this thesis, a general introduction to the exchange bias effect is given. The experiments performed by Meiklejohn and Bean in 1956 are illustrated and the conclusions resulting from these experiments are summarised. Besides the observation of a horizontally shifted hysteresis loop, other typical observation such as rotational hysteresis, training effect and pinned uncompensated spins, were made in exchange biased systems



and are introduced. Finally, some of the leading theoretical models are summarised.

In chapter 3, the theory of contrast formation in MFM, the quantitative interpretation of MFM measurements and all experimental methods used in this thesis are introduced. Note that all MFM data presented in this thesis were acquired with a low temperature ultra high vacuum scanning force microscope (LTSFM).

A major concern in MFM is the stability of the magnetic tip when imaging samples exhibiting strong stray fields. For the first time an exchange coupled ferromagnetic layer was used to coat the MFM tips (chapter 4). This strongly increased the stability (i.e. coercivity) of magnetisation of the tip such that stable imaging became possible.

Finally, in chapter 5, the role of uncompensated spins in exchange biased systems is addressed by performing MFM and magnetometry experiments on two different types of ferromagnet/antiferromagnet samples. We show that the pinned UCS responsible for the exchange bias effect are aligned antiparallel to the ferromagnetic spins. Additionally, pinned UCS aligned parallel to the spins of the ferromagnet do also exist, but are not responsible for the exchange bias effect.

The MFM data obtained on ferromagnetic Co (CoPt-multilayer) coupled to antiferromagnetic CoO or IrMn surprisingly reveals an antiferromagnetic alignment of the net pinned uncompensated spins of the antiferromagnet (AFM) and the adjacent spins of the ferromagnet (FM). On the other hand, positive vertical shifts of the hysteresis loops found for both samples arise from pinned magnetic moments aligned parallel to the cooling field and thus to the adjacent ferromagnetic spins. Thus a contradiction becomes apparent: our MFM data indicate an *antiparallel alignment* of pinned uncompensated spins of the AFM with the spins of the ferromagnet, and our magnetometry data that reveal a *parallel alignment*.

This apparent contradiction can be resolved by introducing a new model in which two groups of pinned uncompensated spins exist in addition to the compensated antiferromagnetically ordered spins of the AFM and to the non-pinned uncompensated spins. A first group of pinned spins with a total magnetic moment  $m_{bulk}$  is located in the bulk of the AFM. These spins would couple to any magnetic field applied to the AFM. The field can be externally applied but also arise from a non-uniform magnetisation (i.e. domains) of the FM. The second group of pinned uncompensated spins has a total magnetic moment  $m_{int}$  and is exchange-coupled antiferromagnetically to the FM spins. These spins must thus be located at or near the FM/AFM interface. Clearly this second group would also couple parallel to an external magnetic field, but the antiferromagnetic exchange coupling to the FM will dominate and these uncompensated spin remain aligned antiparallel to the FM spins.

Most experimental data reported to date arises from both groups of pinned uncompensated spins in the AFM. In addition, in most cases, and particularly for magnetisation loops recorded after field cooling, the magnetic moment due to the uncompensated spins that align parallel to an external field, dominates. This has led to various misinterpretations of otherwise correct experimental data. We thus expect that our work will trigger a re-interpretation of some of the existing experimental data, and serve as a guideline to design experiments that correctly address a single specific group of uncompensated spins. New and systematic experiments could finally resolve the exchange bias puzzle that has now existed for 60 years.

## Chapter 2

# Introduction to the Exchange Bias Effect

The phenomenon of exchange bias is a topic that has been investigated over the last fifty years, beginning with its discovery by Meiklejohn and Bean in 1956. In this chapter, the most important experimental results concerning the exchange bias are described. Then, some theoretical models are illustrated which simulate some of the measured effects.

### 2.1 History and Phenomenology

In 1956, Meiklejohn and Bean reported the discovery of a horizontally shifted hysteresis loop. Furthermore, they observed an enhancement of the coercive field  $H_c$ . The amount of the loop shift is called the exchange bias field  $H_{EB}$  and was interpreted as a new *unidirectional exchange anisotropy* [2]. Compared to a *uniaxial anisotropy*, i.e. two equivalent easy configurations in opposite directions, a system exhibiting a unidirectional anisotropy has only one easy direction. The material exhibiting this exchange anisotropy was a compact of fine particles of cobalt with a cobaltous oxide shell. The effect only occurred if the system was cooled below the Néel temperature,  $T_N$ , of the antiferromagnetic oxide shell in presence of a static magnetic field. Above  $T_N$ , the presence of the antiferromagnet (AFM) only added a paramagnetic behaviour to the hysteresis loop of the ferromagnet (FM). The uniaxial anisotropy thus resulted from an interaction between an antiferromagnetic material and a ferromagnetic material [1].

Since its discovery, the exchange bias effect (EB-effect) has been observed in different kinds of materials. As already mentioned, *Fine particles* were the first type of material where the exchange bias effect was observed. In addition to the oxidised cobalt particles of Meiklejohn and Bean, other ferromagnetic particles covered with their native antiferromagnetic oxide layer like Ni/NiO and Fe/FeO show the same effects. Many *inhomogeneous materials* without clearly defined FM/AFM interface present a shifted hysteresis loop. To this category belong, amongst others, *spin glasses* and polycrystalline materials with a mixture of antiferromagnetic and ferromagnetic components. One of the most studied is Co sputtered in low oxygen pressure, where Co rich and CoO rich areas are formed. On the other hand, studies of *coated antiferromagnetic single crystals* were made: by polishing antiferromagnetic single crystals along a specific crystallographic direction, *com-*

*compensated* or *fully uncompensated* antiferromagnetic interfaces with well defined surface roughness are formed. Any ferromagnetic layer can then be deposited on top of such a well defined surface. Despite the controlled interface, the exchange bias exhibited in these systems is substantially smaller than the one obtained in small particles or thin films. Exchange bias materials in *thin film* form are the most widely studied type of system. Most of the technological applications are also based on thin films [28] where especially the *thickness dependence of ferromagnetic and antiferromagnetic layers* have been studied in detail. For all the systems studied, it has been observed that exchange bias is roughly inversely proportional to the thickness of the FM layer ( $t_{FM}$ ):

$$H_{EB} \propto \frac{1}{t_{FM}} \quad (2.1)$$

indicating that exchange bias is an interface effect. This relation holds for rather thick FM layers of several hundreds of nanometers. However, if the FM layer is too thin, the relation is no longer valid. The value of this “critical thickness” is usually a few nanometers with strong variations from one system to another. The dependence of  $H_{EB}$  on the thickness of the antiferromagnetic layer ( $t_{AFM}$ ) is more complicated: The general trend is that for rather thick antiferromagnetic layers, e.g. over 20 nm,  $H_{EB}$  is independent of the thickness of the AFM. As the thickness is reduced to only a few or below one nanometer,  $H_{EB}$  decreases abruptly and finally becomes zero, although the exact behaviour depends on the specific system studied. From Eq. 2.1 it directly follows that the EB-effect can be described in terms of a surface or interface anisotropy energy per unit area

$$\Delta E = M_{FM} t_{FM} H_{EB} \quad [J/m^2], [erg/cm^2] \quad (2.2)$$

where  $M_{FM}$  and  $t_{FM}$  are the saturation magnetisation and thickness of the ferromagnet and  $H_{EB}$  is the exchange bias magnitude. To compare different systems, independent of the ferromagnetic material and its thickness, the magnitude of the EB-effect is mostly given in terms of such a surface or interface anisotropy energy. Note that in most publications, the units [erg/cm<sup>2</sup>] are used. The typical range of values for  $\Delta E$  is 0.01 - 1 [erg/cm<sup>2</sup>]. The samples studied in this thesis exhibit a  $\Delta E$  of about 0.4 [erg/cm<sup>2</sup>] which is a typical value for the materials used.

Since 1964, systems containing *metallic antiferromagnets* as IrMn have also been investigated. When coupled to a FM, the magnetoresistance (change of resistance by the presence of a magnetic field) of such a system can increase drastically. This change in resistance is called “giant magnetoresistance” (GMR) and was first characterised by Baibich et al. in 1988 [4]. Most magnetic field sensors are nowadays based on GMR. A high Néel temperature  $T_N$  and good corrosion properties have further motivated the research for new metallic AFMs. In addition, several systems with *ferrimagnetic AFMs* have been reported in literature. These systems are even more difficult to analyse theoretically due to the added complexity of the different magnetic sublattices.

In the following we discuss how different structural factors, which disorder the interface (such as roughness, crystallinity and grain size), affect  $H_{EB}$ . It would be desirable to study structural effects on  $H_{EB}$  by varying one parameter (e.g. roughness) at a time while keeping all others constant. Unfortunately, this is very difficult for most exchange bias systems. However, in some cases one parameter changes significantly more than the

others, which are then assumed to be constant. Note that this problem is greatly reduced in AFM single crystals, where different degrees of roughness can be introduced without affecting grain size or crystallinity. In addition, the spin structure at the interface may be affected by structural effects. In section 2.1.4 it is shown how  $H_{EB}$  is strongly influenced by the spin structure at the interface.

Most investigations of the roughness dependence seem to agree that the magnitude of  $H_{EB}$  decreases with increasing roughness. However, some systems appear to be less sensitive to roughness or even behave in the opposite way. The latter, i.e. the magnitude of  $H_{EB}$  increasing with increasing roughness, has been observed for AFM single crystals coated with ferromagnetic layers.

Often in thin film bilayers, the AFM layers are textured and the degree of texture (crystallinity) affects  $H_{EB}$ . Generally, if the AFM is textured in a single orientation,  $H_{EB}$  increases with increasing texture although there are some exceptions to this trend. These results can be related, at least in part, to the spin structure at the interface, i.e. the angle between the FM and the AFM spins at the interface (see section 2.1.4).

The role of the grain size in exchange bias remains unclear. The results from different studies seem to depend on the specific system and conditions, probably because as the grain size changes other parameters are also affected substantially. While  $H_{EB}$  is reported to increase with increasing grain size for some systems, for others (or the same systems)  $H_{EB}$  decreases for larger grain size. It seems that the role of the grain size is related not only to the change in its size, but also to the degree of texture, the spin structure and the anisotropy of the AFM.

All investigations dealing with the role of the anisotropy of the AFM seem to agree with the theories that predict an increased  $H_{EB}$  for larger anisotropies. Certainly related to this is the fact that the exchange bias vanishes above a temperature often denoted as the *blocking temperature*  $T_B$ . In most cases  $T_B$  is much lower than the bulk Néel temperature  $T_N$  of the AFM. This seems to be related to the grain size and thickness of the antiferromagnetic layer through finite size effects [12, 11]. This assumption is further supported by the fact that systems based on single crystal AFM and thick AFM films with large grains tend to have  $T_B \approx T_N$ . Note that for a given sample there is not one single, well defined blocking temperature. Inevitably there is a distribution of blocking temperatures due to different grain sizes, roughnesses and local anisotropies of the sample.

Besides the horizontal shift of the hysteresis loop, other typical observations were made in exchange biased systems and are described in the following sections. First, the hysteresis loop shift and the equivalent unidirectional anisotropy are described in more detail.

Another observation which was already mentioned by Meiklejohn and Bean [3] is the so-called *rotational hysteresis loss*. It is exhibited by a torque curve displaced from the zero torque axis.

In 1966, Paccard et al. [29] first observed the now well known *training effect*. It shows that the exchange bias field decreases with increasing number of hysteresis loop measurements. Finally, with the increasing sensitivity of magnetometers, a small, usually positive *vertical hysteresis loop shift* could be detected in exchange biased systems. This vertical shift of the hysteresis loop is attributed to a small amount of pinned uncompensated moments in the antiferromagnetic layer. Today these uncompensated spins are believed to play a key role in the exchange bias mechanism and are one of the main subjects of this thesis.

### 2.1.1 Hysteresis Loop Shift and Unidirectional Anisotropy

Since their discovery by Meiklejohn and Bean, horizontally shifted hysteresis loops were observed in a large number of different FM/AFM systems. The transition from a shifted to a centred loop appears close to the Néel temperature of the AFM, confirming that it is the presence of the antiferromagnetic material which causes the EB-effect. In most systems, the horizontal shift is opposite to the cooling field direction and is therefore called *negative exchange bias*. Generally, the exchange bias field does not depend markedly on the amplitude of the cooling field. However, studies of FeF<sub>2</sub>/Fe and MnF<sub>2</sub> [30] bilayers revealed a rather unusual behaviour. For large cooling fields the loops, instead of shifting towards negative fields (when cooled in a positive field), shifted to positive fields, i.e. in the same direction as the cooling field. This effect is then called *positive exchange bias*. Different theoretical models have been proposed to explain this effect [30, 31] which are all based on the existence of an antiferromagnetic coupling at the interface between the FM and the AFM layers. Note that for conventional negative exchange bias a ferromagnetic interfacial coupling has usually been assumed.

Independent of the direction of the horizontal shift of the hysteresis loop, it is always accompanied by an increase of the coercivity  $H_C$  below the blocking temperature  $T_B$  which is linked to the anisotropy of the AFM layer. However, the coercivity is also affected by the thicknesses and microstructures of the FM and AFM layers. This increase of  $H_C$  is intuitively simple to understand. For an AFM with small anisotropy, when the FM rotates, it drags the AFM spins irreversibly, hence increasing the FM coercivity. For a large AFM anisotropy, the FM decouples because it cannot drag AFM spins, consequently the coercivity is reduced. A consequence of the influence of the anisotropy is a peak of coercivity that often appears close to  $T_B$  and is due to the decrease of the AFM anisotropy close to  $T_B$ . The width of the peak is related to sample homogeneity which reflects the distribution of AFM anisotropies. An analogous peak effect is found in the AFM thickness dependence of  $H_C$  [12]. The explanation is similar to the previous one: the effective AFM anisotropy is reduced with thickness. For thin enough AFM films, the EB-effect as well as the increase of  $H_C$  disappear.

Figure 2.1 (a), shows an FM/AFM system at a temperature  $T$  that is below the Curie temperature ( $T_C$ ) of the ferromagnet and above the blocking temperature  $T_B$  of the antiferromagnet ( $T_B < T < T_C$ ). The hysteresis loop of the FM/AFM system at this temperature is equal to the hysteresis curve of the pure ferromagnet plus a small paramagnetic part from the AFM and is shown in (b). The hysteresis loop is perfectly centred around the origin. The FM/AFM system is then cooled well below  $T_B$  in presence of a magnetic field  $H$  (or in a state where the FM has a remanent magnetisation), which is usually aligned parallel to an easy axis of the FM (d). The hysteresis loop of the FM/AFM system in this state is shifted along the field axis, generally in the direction opposite (negative) to the applied cooling field (e). Additionally, the hysteresis loop shows a strong increase of the coercivity  $H_C$ .

Meiklejohn and Bean realised that the horizontally shifted hysteresis loop and a unidirectional anisotropy are only different manifestations of the same effect. In other words, the setting of a bias direction while cooling transforms a uniaxial anisotropy, i.e. two equivalent easy configurations in opposite directions (i.e. cobalt), into an anisotropy which has only one easy direction and is often denoted as *unidirectional anisotropy*. Figure 2.1

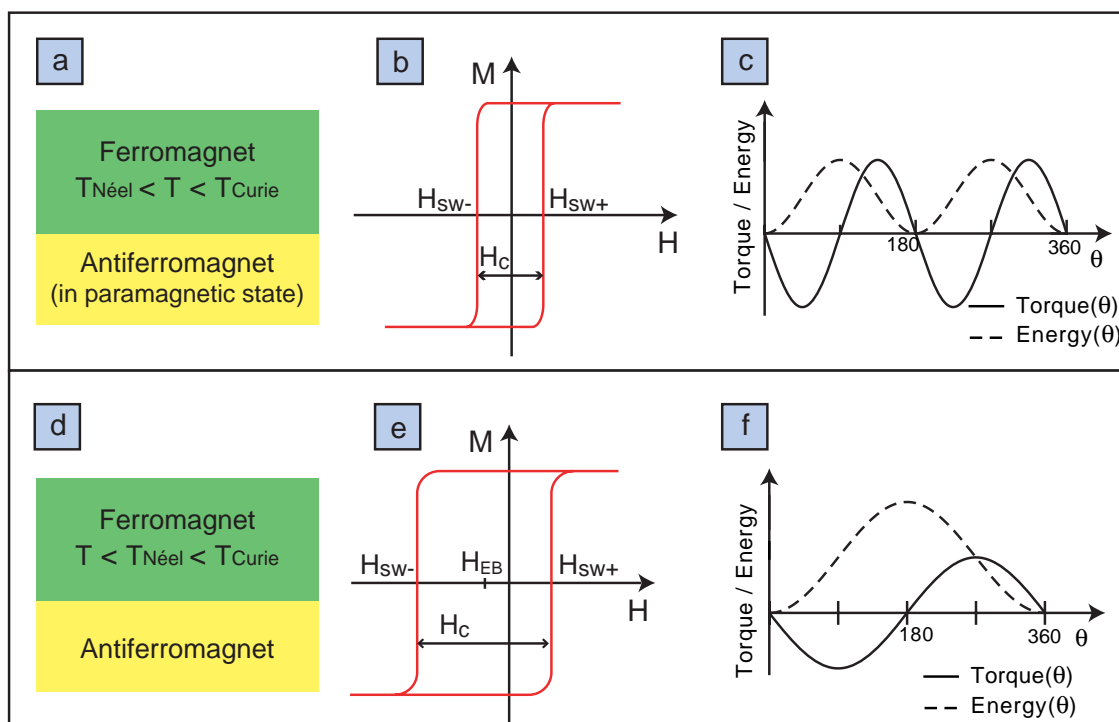


Figure 2.1: Comparison of the magnetic properties of an FM/AFM system at a temperature  $T$  with  $T_B < T < T_C$  (a), and the same system after field-cooling below the AFMs Neel temperature (d) (with  $T < T_B < T_C$ ). The system (a) shows a normal 'ferromagnetic' hysteresis loop (b) and an uniaxial anisotropy, indicated by a  $\sin(2\theta)$ -behavior of the torque measurements (d). System (d), after field cooling below  $T_B$ , shows a horizontally shifted loop with increased coercivity (e), and an unidirectional anisotropy with a  $\sin\theta$ -behaviour of the torque measurements.

(c) shows a typical torque magnetometry curve of a ferromagnetic material with uniaxial anisotropy whereas a torque curve of an exchange biased FM/AFM system is shown in (f). The uniaxial anisotropy of a ferromagnet gives rise to a  $\sin(2\theta)$ -behaviour of the torque signal (c), whereas the  $\sin(\theta)$ -behaviour of the FM/AFM system is a clear sign for a unidirectional anisotropy (f). The energy functions of both systems are represented by the dotted lines in (c) and (f). It is apparent that in (c) two energy minima occur at  $\theta = 0^\circ$  and  $\theta = 180^\circ$  and in (f) only one at  $\theta = 0^\circ$ .

### 2.1.2 Rotational Hysteresis

A further characteristic of exchange biased systems is a torque curve displaced from the zero torque axis due to a rotational hysteresis loss. This rotational hysteresis exists even at high magnetic fields which clearly differs from the behaviour of pure ferromagnets. In contrast to normal ferromagnetic materials in which this quantity approaches zero as the field becomes infinite or saturation becomes complete, the rotational hysteresis of an

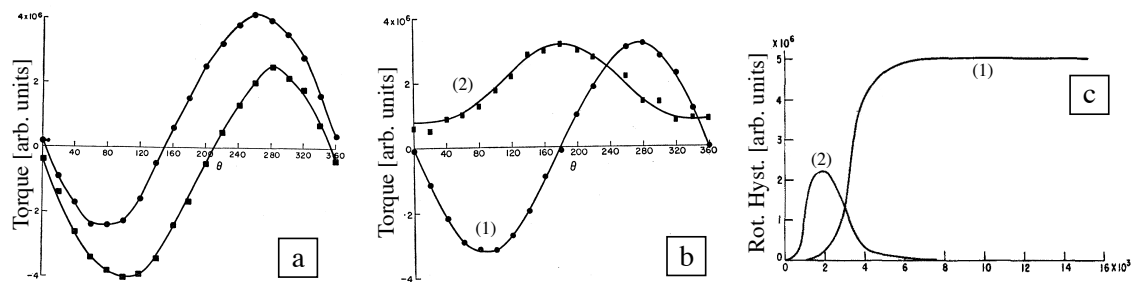


Figure 2.2: Rotational hysteresis of an FM/AFM system: (a) Torque curves taken for rotations of increasing and decreasing angles of  $\theta$ . The curve (1) in Fig. (b) shows a 'true' torque curve that can be calculated by averaging both directions of rotation. The "rotational hysteresis" (curve (2) in Fig. (b)) is the difference of the torque curves shown in (a). (c) shows the rotational hysteresis as a function of cooling field  $H_{cool}$ , taken below (curve (1)) and above the Néel temperature of the AFM (curve (2))

FM/AFM system approaches a finite value with increasing cooling field. It might be interesting to note that the rotational hysteresis is related to the increase of coercivity in exchange biased systems. It is even very probable that the increase of coercivity and rotational hysteresis are different manifestations of the same effect, i.e. the losses produced during the rotation of the FM layer by the AFM spin drag. This is supported by the observation of a peak in rotational hysteresis close to the blocking temperature  $T_B$  as it can be observed for coercivity as well. Rotational hysteresis in high magnetic fields is a distinct feature of exchange biased systems and was first identified by Meiklejohn and Bean [2, 3].

The upper and lower curve in Fig. 2.2 (a), correspond to rotations of increasing and decreasing angles of  $\theta$ , respectively. In order to get the 'true' torque curve, the average of both directions of rotation is plotted in (b). In addition, the difference in torque values, representing the rotational hysteresis, is also shown in (b). The rotational hysteresis as a function of applied field is shown in (c), for an FM/AFM system above and below the Néel temperature of the AFM. This singular behaviour can be qualitatively understood as a discontinuous reorientation of the spins in the AFM layer, which occurs because of its interaction with the magnetisation of the cobalt.

Fujiwara et al. [32] investigated the rotational hysteresis loss and the training effect for an IrMn/NiFe sample. They proposed a new model which is based on the incorporation of a direct exchange coupling between the AFM-grains (extended Fulcomer and Charp model, see section 2.2.3). This leads to the conclusion that the rotational hysteresis loss and the training effect have the same origin.

### 2.1.3 Training Effect

It is well known that in many exchange biased systems, the bias field  $H_{EB}$  depends on the number of consecutive hysteresis loop measurements performed. This property called *training effect* was first discovered in 1966 by Paccard et al.[29] shortly after the discovery

of the exchange bias shift by Meiklejohn and Bean. For instance, if several consecutive hysteresis loops are measured, the shift  $H_{EB}$  of consecutive loops will decrease. It can thus be characterised by the change of the switching fields,  $H_{sw-}$  and  $H_{sw+}$ , with the number of hysteresis cycles.  $H_{sw-}$  ( $H_{sw+}$ ) define the field at which the sample magnetisation switches from positive to negative (negative to positive) values (see Fig. 2.3). This empirical variation of the switching fields with the number of consecutive hysteresis loop measurements can be subdivided into three different types. In the first type of exchange biased systems, henceforth called Type I, the hysteresis loop shrinks from both sides, which means  $H_{sw-}$  increases ( $|H_{sw-}|$  decreases) and  $H_{sw+}$  decreases. This behaviour of the switching fields corresponds to the one observed by Paccar. If both switching fields,  $H_{sw-}$  and  $H_{sw+}$  increase, the training effect is denoted as Type II. It is not very surprising that an intermediate case between Type I and Type II systems was also found and is denoted as Type 0 training effect. In Type 0 systems  $H_{sw-}$  increases, as in Type I and II, and  $H_{sw+}$  stays constant. This behaviour could mainly be observed in systems with metallic AFMs, such as FeMn and IrMn. The behaviour of Type I, II and 0 training effect in FM/AFM systems is illustrated in Fig. 2.3 (a) to (c) respectively. For each Type, the first (red), the second (orange) and fifth (yellow) of the consecutively measured hysteresis loops are shown. Experimentally, it is often found that  $H_{EB} - H_{EB\infty} \propto 1/\sqrt{n}$  where  $n$  indicates the order consecutive loops measured. It is important to stress that the training effect is more important in polycrystalline AFMs and is very small or non-existent in systems based on single crystals.

A model based on AFM grain-grain interaction in polycrystalline samples [33, 32] which involves the three types of training will be introduced in section 2.2.3 The same model also predicts the rotational hysteresis loss as described in section 2.1.2.

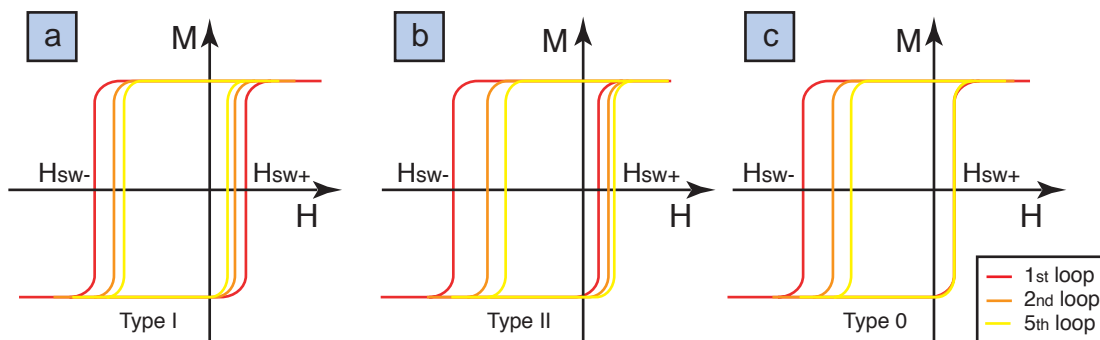


Figure 2.3: Type I, II and 0 training effect for the first (red), second (orange) and the fifth (yellow) hysteresis loop measurement

#### 2.1.4 Uncompensated Spins and Vertical Hysteresis Loop Shift

Due to the interfacial nature of exchange bias it may be expected that  $H_{EB}$  strongly depends on the spin configuration at the AFM/FM interface. To study this effect exchange bias systems have been investigated using different AFM orientations. Two main issues



concerning the orientation have been addressed: *compensated* versus *uncompensated* AFM surfaces and *in-plane* versus *out-of-plane* AFM spins. However, the main problem in this kind of studies is the difficulty to determine the exact spin configuration at the interface. It is customary to assume that the bulk spin configuration is preserved although it is possible that at the interface the AFM atoms relax or reconstruct.

In a *compensated* AFM interface the net spin averaged over a microscopic length scale is zero. Therefore, this kind of surface will have zero net magnetization. In contrast, if the spin arrangement is such that the surface magnetization is non-zero, the surface is *uncompensated*. Intuitively, one may expect that for compensated surfaces, the spins pinning the FM layer cancel giving rise to a net zero  $H_{EB}$ . Note that a compensated surface remains compensated in the presence of unit cell random roughness, however, more complicated roughness could result in uncompensated surfaces. It was found that all compensated surfaces investigated experimentally do exhibit exchange bias! Some of the investigated systems exhibit very large loop shifts, often even larger than the uncompensated orientation of the same AFM material.

Usually, the theories assume that the AFM spins at the interface lay on the interface plane, i.e. parallel to the adjacent FM spins. However, certain orientations of some AFM materials have spins pointing out of the interface plane, i.e. perpendicular to the FM spins, if the bulk spin structure is preserved. As an example, the exchange field for different  $\text{FeF}_2$  orientations exhibit a clear trend: when the AFM spins are in the plane ( $\text{FeF}_2(110)$ ),  $H_{EB}$  is maximum, but when the spins are completely out of the interface plane ( $\text{FeF}_2(001)$ ),  $H_{EB}$  is zero [30]. A similar trend was observed for different orientations of FeMn. An intuitive explanation for this effect comes from the FM/AFM spin-spin interaction strength which depends on the angle  $\alpha$  between both spins. If  $\alpha=0^\circ$ ,  $H_{EB}$  will be maximum whereas for  $\alpha=90^\circ$   $H_{EB}$  will tend to zero.

In order to understand exchange bias in terms of spin structure, there is compelling need to determine the distribution of uncompensated magnetization at the FM/AFM interface, in the AFM bulk and the response of uncompensated magnetization to applied magnetic fields. The determination of the orientation and the local density of the uncompensated magnetization of the AFM layer is one of the main objectives in this thesis.

The existence of pinned uncompensated spins in AFM layers has first been experimentally proven by Takano et al. [13]. They reported the measurement of thermoremanent moments (TRM) in CoO/MgO-multilayers. The CoO/MgO multilayers were zero field cooled then field cooled in 1 T to 10 K. Field cooling resulted in a stable magnetization, a TRM whereas zero field cooling resulted in no TRM. From the fact that the magnitude of the TRM scaled closely with the number of CoO layers and had no dependence on the net CoO thickness in the sample, it was concluded that the uncompensated moments must be an interfacial and not a bulk effect. The uncompensated moments corresponded to about 1% of the spins in a monolayer of CoO. The TRM was positive, i.e. the uncompensated moments were aligned parallel to the cooling field. In addition it was shown that the TRM of the CoO/MgO multilayer samples had the same temperature dependence as the exchange field of  $\text{Ni}_{81}\text{Fe}_{19}/\text{CoO}$  bilayers after field cooling. Thereof they concluded that the interfacial uncompensated spins (measured via TRM) were responsible for the unidirectional anisotropy. Finally they developed model based on a calculation of the density of these interfacial uncompensated spins which predicted the correct magnitude of the

exchange field.

The existence of pinned uncompensated spins in FM/AFM layers has first been shown by Nogues et al. [30]. They determined the uncompensated moments in  $\text{FeF}_2/\text{F}$  and  $\text{MnF}_2/\text{F}$  bilayers from the shift along the magnetization axis (vertical shift) of the hysteresis loop. The magnetization shift strongly depended on the cooling field and the microstructure of the AFM layer. For small cooling fields, the shift was in some cases opposite to the applied cooling field, indicating an antiferromagnetic coupling at the interface. The samples exhibiting negative vertical shifts of the hysteresis loops all showed large changes in  $H_{EB}$  as a function of the applied cooling field: for high enough cooling field these samples even change to positive exchange bias fields. Samples exhibiting positive magnetization shifts, i.e. ferromagnetic coupling, show almost no change in  $H_{EB}$  with cooling field and the exchange bias field remained always negative. However, the origin of the induced moment could not directly be assigned to either interface or volume magnetisation.

A systematic study of the change in AFM magnetisation with the number of introduced volume defects in the AFM layer was presented by Keller et al. [34]. They precisely determined the vertical hysteresis loop shift of a FM/AFM samples for both, unintentionally diluted and oxygen-diluted AFM layers. It was shown that at large cooling fields, the vertical shift is positive and overall increasing with dilution of the AFM layer. This increase can directly be linked to the creation of additional volume defects in the AFM layer. For cooling fields below 1 T they observed a strong reduction of the vertical shift for all samples. It is noteworthy that at very low cooling fields the vertical shift of diluted samples always remained finite and positive whereas it changed sign and became negative for unintentionally diluted samples. It was suggested that at low cooling fields the AFM magnetisation primarily originates from the AFM spins close to the interface which then would be antiferromagnetically coupled to the FM spins.

In 2001 Ohldag et al. [15] first proved the existence of a chemically produced interfacial layer in contrast to the previous assumption of abrupt FM/AFM interfaces. This interface layer naturally gives rise to uncompensated spins. They investigated a  $\text{NiO}(100)/\text{Co}$  sample using x-ray absorption spectroscopy. It was shown that uncompensated interfacial spins arose from an ultrathin  $\text{CoNiO}_x$  layer that was formed upon Co deposition through reduction of the NiO surface. The weak interfacial signal could thus be isolated from the bulk as it exhibits a unique chemical structure. The uncompensated spins at the interface were aligned parallel to the AFM spins in  $\text{NiO}(100)$  and thus collinear to the ferromagnetic spins in Co.

In 2003 Ohldag et al. [16] used high sensitivity x-ray magnetic circular dichroism (XMCD) spectroscopy in total electron yield (TEY) detection to identify uncompensated Ni or Mn spins in the three polycrystalline exchange biased systems  $\text{NiO}/\text{Co}$ ,  $\text{IrMn}/\text{Co}$  and  $\text{PtMn}/\text{CoFe}$ . The TEY method offers sensitivity to the interfacial regions because of the limited  $1/e$  probing depth as explained in detail in [15]. They measured element specific hysteresis loops of Ni and Mn and showed that about 4% of a monolayer of spins is tightly pinned and parallelly aligned to the AFM. The size of the pinned interfacial magnetization was found to be quantitatively correlated to the macroscopic magnetic exchange bias field, using a modified simple model, originally suggested by Meiklejohn and Bean.

If the magnetisation of the AFM is irreversible under field reversal, the uncompensated

spins are pinned and can be identified as a small vertical shift  $m_{vs}$  of the hysteresis loop of an FM/AFM-system. Figure 2.4 gives an overview over possible configurations of the antiferromagnetic layer in FM/AFM systems and show their effect on the vertical hysteresis loop shift. The AFM layer in 2.4 (a) has an even number of alternating spin planes and is therefore fully compensated. Independent of the coupling at the interface, such a system exhibits no vertical shift even though a negative horizontal shift is present. The antiferromagnetic layers in 2.4 (b) and (c) contain an odd number of alternating spin planes such that one layer remains uncompensated. For a ferromagnetic (parallel) coupling at the interface a positive vertical shift will be observed (b). For an antiferromagnetic (antiparallel) interfacial coupling the hysteresis loop shift is opposite to the cooling field direction (and the magnetisation direction of the FM). However, perfect antiferromagnetic layers as assumed in (a), (b) and (c) do not exist in nature. In reality, uncompensated spins created by defects also exist in the bulk of the AFM layer as indicated in 2.4 (d). These spins will most probably align with the cooling field and therefore be responsible for a positive vertical hysteresis loop shift. Depending on the number and orientation of uncompensated bulk or interfacial spins, a positive or a negative vertical shift can be observed.

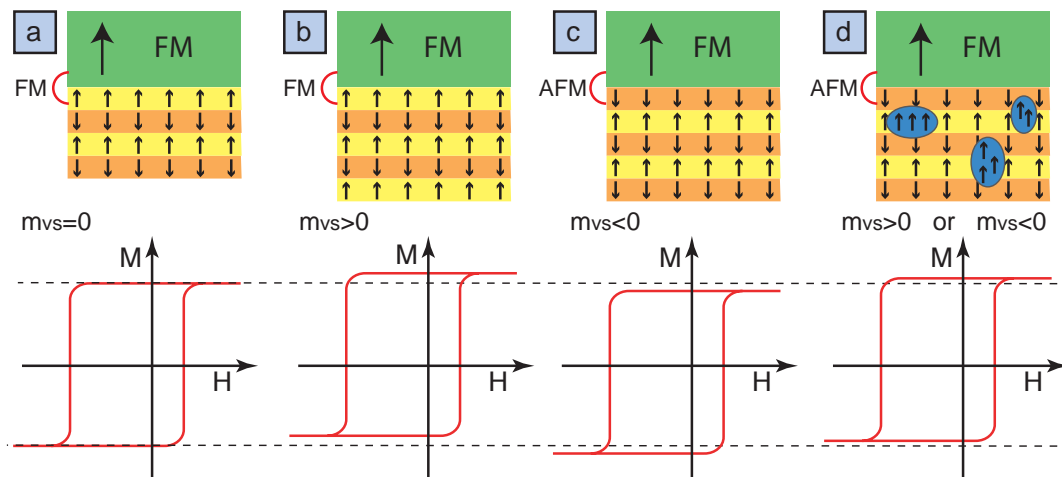


Figure 2.4: Vertical shift of different FM/AFM bilayers after cooling below  $T_N$  in a field applied parallel to the FM magnetisation: A fully compensated AFM layer will not generate any vertical loop shift (a). For uncompensated AFM layers ((b) and (c)) the vertical loop shift is positive (b) for a ferromagnetic and negative (c) for an antiferromagnetic interfacial coupling. In reality, uncompensated spins also exist in the bulk of the AFM (d). The vertical shift then strongly depends on the number and orientation of bulk and interfacial spins.

To resume, extensive research in the last decade has led to the notion that the exchange bias effect must originate from uncompensated interfacial spins that are anchored in the AFM and do not follow the external field. The existence of pinned uncompensated moments was shown using various experimental techniques. Most frequently highly sen-

sitive hysteresis loop measurements are performed in order to detect small vertical shifts. Furthermore XMCD techniques, soft x-ray resonant magnetic scattering [17], polarized neutrons [35] and MFM [19] was used to detect the UCS in EB-systems.

It is noteworthy that strong variations of UCS densities were found even for similar EB-systems. However, it is more surprising is that the orientation of the UCS relative to the FM is not found to be consistent even for similar EB-systems. For the majority of samples and techniques used, a parallel alignment between the pinned uncompensated spins of the AFM and the ferromagnetic spins was found. On the other hand, a small number of studies reported an antiparallel alignment of the UCS with the FM magnetisation. Thus the detection of the pinned uncompensated spins, the determination of their orientation, size and origin, as well as their quantitative link to the size of the exchange bias field remains forefront research problems.

## 2.2 Theoretical Models

Since the discovery of the EB-effect, great efforts have been made to explain the numerous experimental observation presented in section 2.1. Nevertheless, none of the proposed models is able to simulate all experimental facts. Thus, the EB-effect is still not fully understood. Most of them agree on the fact that pinned uncompensated moments in the AFM must be responsible for the exchange coupling to the FM and aim to successfully simulate the observed horizontal shift of the hysteresis loop. Some authors also elaborated models to explain less general observation such as the training effect. An incomplete overview of models that apply to polycrystalline thin film samples will be given in this section, starting with the originally proposed model by Meiklejohn and Bean.

### 2.2.1 Rigid Antiferromagnet Model: Meiklejohn and Bean

An intuitive but idealised picture of the exchange bias mechanism suggested by Meiklejohn and Bean [3] is shown in Fig. 2.5. For the temperature  $T$ , with  $T_N < T < T_C$ , the spins of the FM line up with an applied magnetic field and the antiferromagnetic spins remain random (a). When cooling to  $T < T_N$  in the presence of a field the AFM spins align ferromagnetically to those of the FM (assuming ferromagnetic coupling) due to the interaction at the interface (b). When the field is reversed (c), the ferromagnetic spins start to rotate. However, for sufficiently large AFM anisotropy, the AFM spins remain unchanged and the interfacial interaction between the antiferromagnetic and ferromagnetic spins tries to keep the FM spins aligned to the AFM spins. Microscopically seen, the antiferromagnetic spins at the interface exert a torque on the ferromagnetic spins. Therefore the ferromagnetic spins have only one single stable configuration, i.e. the anisotropy becomes *unidirectional*. Thus, the field needed to reverse the FM layer will be larger because an additional microscopic torque has to be overcome. However, the FM spins will start to rotate at a smaller field when returning to their original orientation due to the microscopic torque which is 'pulling' them back. The spin states (b)-(d) are indicated on the corresponding place of the hysteresis loop of the system (right side of Fig. 2.5) [12].

In this intuitive model, the energy per unit area on an exchange bias system, assuming

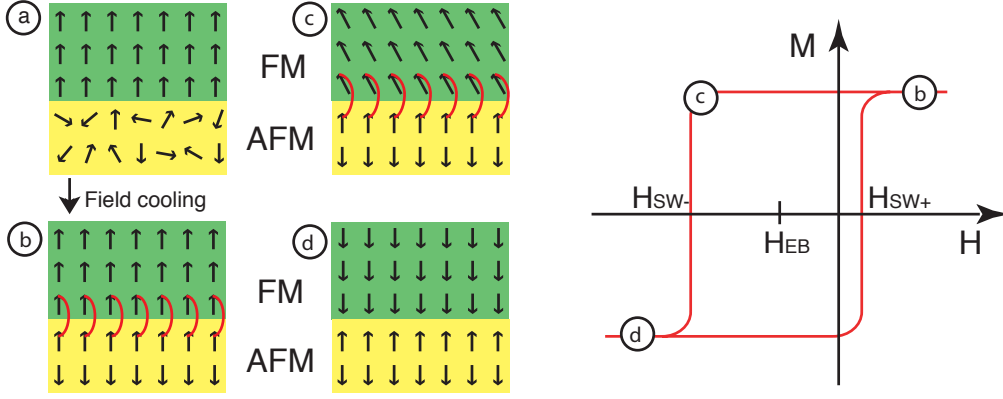


Figure 2.5: Schematic diagram of the spin configuration and the corresponding places on the hysteresis loop for an FM/AFM bilayer in the rigid antiferromagnet model: spin configuration for  $T_N < T < T_C$  in an applied magnetic field (a), state after field cooling below  $T_N$ , assuming a ferromagnetic coupling of AFM and FM spins at the interface (b), the reversed field starts to rotate the FM but not the AFM spins (c), the FM magnetisation has been completely reversed (d). The states corresponding to (b) - (c) are shown in the hysteresis loop of the FM/AFM bilayer on the right.

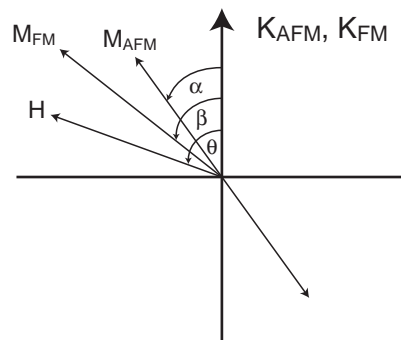
coherent rotation of the magnetization can be written [3] as

$$E = -HM_{FM}t_{FM}\cos(\theta - \beta) + K_{FM}t_{FM}\sin^2(\beta) + K_{AFM}t_{AFM}\sin^2(\alpha) - J_{FM/AFM}\cos(\beta - \alpha) \quad (2.3)$$

where  $H$  is the applied field,  $M_{FM}$  the saturation magnetisation,  $t_{FM}$  the thickness of the FM layer,  $t_{AFM}$  the thickness of the AFM layer.  $K_{FM}$  and  $K_{AFM}$  are the anisotropy constants of FM and AFM layers respectively.  $J_{FM/AFM}$  is the interface exchange anisotropy energy per unit area and  $\beta$ ,  $\alpha$  and  $\theta$  are the angles between the magnetisation and the FM anisotropy axis, the AFM sublattice magnetisation ( $M_{AFM}$ ) and the AFM anisotropy axis, and the applied field and the FM anisotropy axis (see Fig. 2.6). Note that the AFM and FM anisotropy axes are usually assumed to be in the same direction, i.e. collinear. The first term in the energy equation accounts for the effect of the applied field on the FM layer, the second term is the effect of the FM anisotropy, the third term takes into account the AFM anisotropy and the last term takes into consideration the interface coupling. However, the above equation assume parallel FM and AFM anisotropy axes, ferromagnetic coupling at the interface as well as the absence of AFM and/or FM domains[12]. Meiklejohn and Bean suggested that the horizontal hysteresis loop shift is due to a large anisotropy in the AFM and a weaker exchange energy coupling the FM and the AFM. Therefore the FM anisotropy is assumed to be negligible [3] (the condition  $K_{FM}t_{FM} \ll K_{AFM}t_{AFM}$  is often fulfilled experimentally), thus Eq. 2.3 simplifies to

$$E = -HM_{FM}t_{FM}\cos(\theta - \beta) + K_{AFM}t_{AFM}\sin^2(\beta) - J_{FM/AFM}\cos(\beta - \alpha). \quad (2.4)$$

Figure 2.6: Schematic diagram of angles involved in an exchange bias system. Note that the AFM and FM anisotropy axes are assumed collinear and that the AFM sublattice magnetization  $M_{AFM}$  has two opposite directions.



The loop shift is found by minimising the energy with respect to  $\alpha$  and  $\beta$ , [3],[36]

$$H_{EB} = \frac{J_{FM/AFM}}{M_{FM}t_{FM}}. \quad (2.5)$$

Another important result from this minimisation is that the condition  $K_{AFM}t_{AFM} \geq J_{FM/AFM}$  is required for the observation of exchange bias anisotropy. If  $K_{AFM}t_{AFM} \gg J_{FM/AFM}$  then the system is minimised by keeping  $\alpha$  small independently of  $\beta$ . However, if  $J_{FM/AFM} \gg K_{AFM}t_{AFM}$  it is energetically more favourable to keep  $(\beta - \alpha)$  small, i.e. AFM and FM spins rotate together. In other words, if the above condition is not satisfied, the AFM spins follow the motion of the FM layer, thus no loop shift would be observed, only an increase in coercivity. The exchange bias magnitude predicted by these calculations depends on the assumed value for  $J_{FM/AFM}$ . If  $J_{FM/AFM}$  is taken to be similar to the FM exchange,  $H_{EB}$  is predicted to be several orders of magnitude larger than the experimental result [37].

Clearly, this simple idealised model does not realistically represent the FM/AFM interfacial environment. Other studies attempt to account for different important parameters in EB-systems which are not considered in the basic formula of Meiklejohn and Bean. These include the formation of domains in the AFM and/or the FM layer, field effects on the AFM layer, grain size and roughness, non-collinearity of the AFM-FM spins, random anisotropy in the AFM layer, uncompensated surface spins and many others. Especially the interfacial roughness is often considered to account for the reduction of interfacial coupling strength. Polycrystalline films are composed of subunits or grains which possess a distribution of orientations which may reduce exchange bias effect. Yet, FM films coupled to polycrystalline AFM films often have higher exchange fields than FM films coupled to single crystalline AFMs [11].

### 2.2.2 Uncompensated Interfacial AFM Spins Model: Takano et al.

Takano et al. [13, 38, 11] first reported the measurements of thermoremanent moments (TRM) in CoO/MgO multilayers. Field-cooling the multilayers from  $T > T_N$  resulted in a stable magnetization, a TRM. The magnitude of the measured TRM scaled closely with the number of CoO layers and had no dependence on the net CoO thickness in the multilayers. Thereof it was concluded that the uncompensated moments are located at the interfaces. The measured uncompensated moments represented about 1 % of the spins in CoO monolayer. This low density is consistent with the low exchange fields observed

compared to the values predicted by the ideal interface model. (see Eq. 2.4). Furthermore the temperature dependence of the TRM was similar to the temperature dependence of the sublattice magnetisation for bulk CoO as determined by neutron diffraction [39], from which a strong coupling of the interfacial spins to the core spins of CoO was suggested. For comparison, permalloy/CoO bilayers were field cooled whereas the exchange bias field was measured. It was observed that the previously measured TRM of the CoO/MgO samples exhibited the same temperature dependence as the exchange field of the permalloy/CoO samples after field cooling. From this correlation the existence of a direct relationship between the interfacial density of uncompensated spins and the strength of the exchange bias field was suggested. Furthermore, they determined a linear relationship between the strength of the exchange field and the inverse of the CoO crystallite diameter, i.e.  $H_{EB} \propto L^{-1}$ , where  $L$  is the grain diameter. This suggests a structural origin for the density of uncompensated spins.

Based on these experimental facts, a model was elaborated which related  $H_{EB}$  with the interfacial density of uncompensated spins and predicted the inverse relationship between  $H_{EB}$  and the grain diameter. Further, the model presented the structural origins of the uncompensated spins in polycrystalline AFM films: The density of interfacial uncompensated spins was calculated as a function of grain size, orientation, and interfacial roughness of polycrystalline AFM films. Each CoO crystallite was assumed to be a single AFM domain. Fig. 2.7 (a) shows the interfacial cross section of an AFM crystal. It indicates that the orientation of the AFM determines the periodicity with which the [111] ferromagnetic spin planes intercept the interface. Fig. 2.7 (b) is a plan view of the same AFM crystal. The crystalline orientation is reflected in the periodic alternating pattern of four rows. An elliptical sampling region simulating a grain with a major axis length  $L$  has been superimposed onto the spin map. The number of uncompensated spins  $\langle \Delta N \rangle$  for a model crystallite was computed by simply adding the total number of spins in each direction contained within the boundaries of the model grain. The fundamental origin of uncompensated AFM moment is thus scale. Although the large spin map may represent compensated spin regions, one observes small densities of uncompensated spins when sampling small areas. Furthermore, interfacial roughness was incorporated onto the spin maps by superimposing elliptical “islands” of monoatomic thickness on the spin map (Fig. 2.7 (b) bottom image). The effect of adding one atomic layer is to reverse the direction of the spin at each site covered by the island. For the simulation, a series of large spin maps, several times larger than the model grain sizes was created. Statistical averages were obtained from sampling  $10^6$  model crystallites by varying the position, orientation of the major axis, and aspect ration of the crystallites. Two primary results of these calculations were: (1) a perfectly regular interface without any roughness features results in  $\langle \Delta N \rangle \propto L^{0.5}$ , (2) the addition of roughness results in  $\langle \Delta N \rangle \propto L^{0.9 \sim 1.04}$ . Since the exchange field is proportional to  $\langle \Delta N \rangle / L^2$ , the rough case gives  $H_{EB} \propto L^{-1}$  in agreement with the experimental results. Using realistic and experimental values, the observed exchange field for a 10 nm CoO biasing film was consistent with interfacial roughness of only a few extra atomic steps across the face of each crystallite. Fig. 2.7 (c) shows the different alignment of zero-field cooled and field cooled uncompensated spin moment of uniaxial AFM grains. The uncompensated AFM moments are randomly aligned in the zero field cooled case, whereas in the field cooled case, the uncompensated moments are aligned

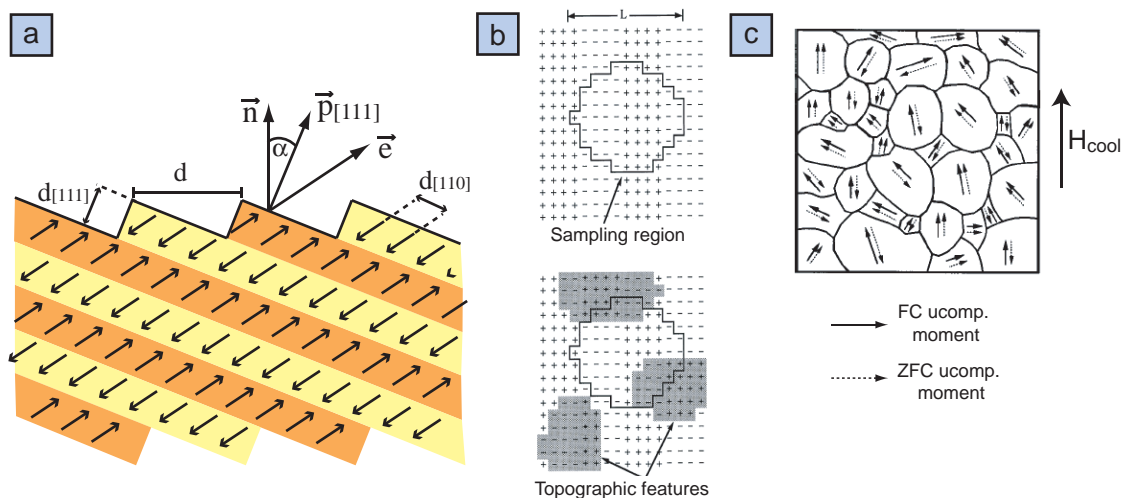


Figure 2.7: Schematic of the “Takano-model”: Panel (a) shows a schematic of the interface cross section of an AFM grain. The film normal is  $\vec{n}$ ,  $\vec{p}$  is the normal to the parallel [111] spin planes of the AFM and  $\vec{e}$  is the AFM spin axis. (b) shows a topographical representation of the interfacial plane as shown in (a) with a sampling region representing a model crystallite. At the bottom image of (b), elliptical “islands” of monoatomic layer thickness were superimposed on the spin map to simulate roughness. Note that adding one atomic layer reverses the direction of the underlying spin. The alignment of the net uncompensated moments in the zero-field cooled (ZFC) and field-cooled (FC) case is illustrated in (c).

along the uniaxial direction with a component in the cooling field direction.

To summarize, the model elaborated by Takano et al. correctly predicts the inverse dependence of the UCS on grain size and the correct magnitude of  $H_{EB}$ . Additionally it indicates that the origins of the uncompensated AFM interfacial moment are (i) the dimensions of the AFM grains and (ii) the presence of interfacial roughness features.

### 2.2.3 Training Effect Model: Zhang et al.

The two models presented in the previous sections aim to successfully simulate the horizontal shift of the hysteresis loop, i.e. the measured exchange field. However, these models are unable to simulate other experimentally observed phenomena like for example the training effect. Especially metallic, polycrystalline FM/AFM systems which are technically important for spins valves exhibit a substantial training effect. Zhang et al. [40, 32, 33] found that the training effect can be successfully modeled by introducing positive and negative interactions between the AFM grains constituting the AFM layer of FM/AFM systems.

Experimentally, three different types of training effect can be observed in EB-systems and are described in section 2.1.3. Zhang et al. observed that in sputtered NiFe/IrMn( $t_{AFM}$ ) bilayers the type of training changed from Type I to Type II with increasing thickness of



the AFM layer. In Type I training, the hysteresis loop shrinks from both sides with the number of cycles, while in Type II training it shifts toward the positive pinned direction accompanied by loop shrinkage (see Fig. 2.3). The thickness of the AFM layer was varied from 0 to 30 nm. Hysteresis loop measurements were performed using a VSM where the field was cycled continuously (20 times) starting from the positive saturation. An exchange bias field  $H_{EB}$  started to appear when  $t_{AFM}$  was about 3 nm, then it increased drastically with increasing  $t_{AFM}$  and finally started to decrease above a thickness of about 10 nm. The training effect started to appear with the appearance of  $H_{EB}$ , then it increased drastically to a peak and finally decreased quickly to almost zero at an AFM thickness of about 10 nm. It is important to note that with increasing  $t_{AFM}$ , the type of the training effect changed from Type I to Type II. The transition occurred when the training effect passes its peak at an AFM thickness of about 4 nm.

Zhang et al. were able to explain the above results by an extended Fulcomer and Charap's model [41] in which direct positive and negative exchange coupling between the AFM grains was incorporated. According to Néel's suggestion, they introduced the direct ex-

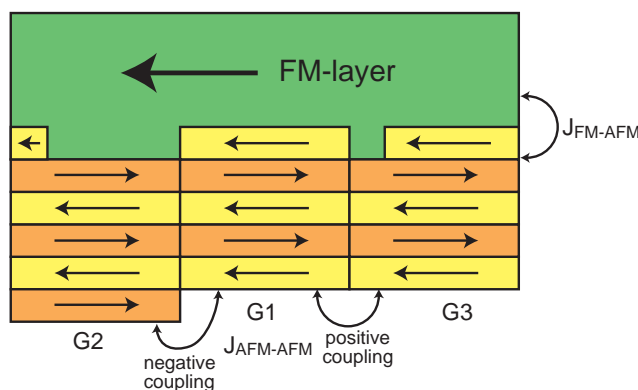


Figure 2.8: Positive and negative coupling between the AFM-grains: The sublattices of the neighbouring grains of the same spin orientation are aligned in the same plane. Then a positive coupling exists between the neighbouring grains with a parallel surface net moment orientation (Grain 1 and Grain 2) and a negative coupling between the neighbouring grains with an antiparallel surface net moment orientation.

change coupling  $J_{AFM-AFM}$  between the AFM grains. As an example, a negative coupling may exist between two AFM grains whose sublattices match each other but the net surface moment of each grain is pointing antiparallel to each other. This situation is illustrated in Fig. 2.8 between Grain 1 and Grain 2. Likewise, the case of positive coupling is defined by a parallel alignment of the net surface moment of neighboring grains and is illustrated in Fig. 2.8 between Grain 1 and Grain 3. The strength of the coupling between the AFM grains must have a wide range of distributions. For the simulation the following assumptions were adopted: (1) The magnetisation of the FM layer behaves coherently and the anisotropy is negligible. (2) The AFM layer is composed of densely aligned cubic grains of the same size. (3) The absolute values of  $J_{AFM-AFM}$  of positive and negative couplings between AFM grains have the same Gaussian distribution with peaks at a positive and a

negative value respectively and with the same mean value. A justification for the latter assumptions is that after sputtering the surface net spins are randomly orientated before the FM layer is deposited. (4) The coupling strength between FM and AFM,  $J_{FM-AFM}$ , is inversely proportional the diameter of the AFM grain. (5) The anisotropy of the AFM grains is uniaxial and their easy axes distribute in the plane symmetrically with respect to the pinned direction in some range of angle. (6) The distribution of the values of  $r$ , with  $r = J_{FM-AFM}/2K_{AFM}t_{AFM}$  where  $K_{AFM}$  is the anisotropy constant of the AFM grain and  $t_{AFM}$  is the thickness of the AFM layer, is Gaussian. The AFM-AFM coupling strength was restricted within a range of several times as large as the FM-AFM coupling strength.

The simulation of the training effect can be summarized as follows: For relatively weak coupling of the AFM grains ( $|J_{AFM-AFM}^{mean}|/J_{FM-AFM} = 0.4$ ) a Type I training effect was obtained. By increasing the coupling strength of the AFM grains to  $|J_{AFM-AFM}^{mean}|/J_{FM-AFM} = 0.04$ , a Type II behaviour of the training effect was simulated. As it is very likely that the coupling between AFM grain increases with the AFM film thickness, the simulations seem to agree with the experimentally found transition from a Type I to a Type II training effect by increasing the thickness of the AFM layer.

To resume, Zhang et al. were able to show that an independent AFM-grain model is not sufficient to describe the magnetic behaviour of EB-systems. The direct exchange coupling between the AFM-grain seems to be crucial for at least one of the often observed phenomena, the training effect.

## Chapter 3

# Instrumentation and Methods

All instrumental techniques and mathematical methods used to analyse MFM data are described in this chapter. The magnetic force microscopy images were acquired with a home built low temperature scanning force microscope illustrated in [42, 20]. Hysteresis loop measurements were performed with a *Quantum Design PPMS* at the EMPA in Dübendorf (Swiss Federal Lab for Materials Testing and Research). Transmission electron microscopy (TEM) images were taken at the EPF (Swiss Federal Institute of Technology) in Lausanne with a *Philips CM 300* high resolution TEM.

### 3.1 Magnetic Force Microscopy: MFM

Magnetic force microscopy is commonly understood as a scanning force microscopy technique that is devoted to the measurement of tip-sample forces mediated by a magnetic field. In fact, every scanning force microscope (SFM) can be used as a magnetic force microscope, if a tip with a magnetic moment is used. In this mode the SFM becomes sensitive to the magnetic field emanating from the surface of a sample. The first experiments to measure the forces between a ferromagnetic sample and a tip that carries a permanent magnetic moment were performed shortly after the invention of the SFM [23]. Most of this preliminary work was devoted to imaging written structures in magnetic recording materials. Since then, magnetic-field-mediated forces have been measured on a wide variety of samples and experiments were successfully performed under many different environmental conditions such as in ambient air, vacuum, ultra high vacuum (UHV), low temperatures and strong magnetic fields.

Although any SFM can be used as a magnetic force microscope, the measurement of magnetic forces remains challenging. While the tip-sample force is usually in the nN range in typical scanning force microscopy experiments dedicated to measuring the topography of a sample in both contact and non-contact modes of operation (see section 3.2), magnetic forces are typically two to three orders of magnitude smaller. Thus, in MFM experiments, the tip is scanned close to the surface of the sample, but the tip-sample distance must remain sufficiently large to avoid a strong non-magnetic tip-sample interaction due to topography-dependent forces. However, in this thesis a method originally developed by Foss et al. [43] was used to separate the magnetic and topographic contributions to an MFM image (see section 5.3.1).

The SFM used in this thesis operates under UHV, at low temperatures and in magnetic fields up to 7 T. Cantilevers and samples can be prepared in UHV in the connected preparation chamber and then be transferred to the microscope. The UHV-system with cryostat, the SFM, the interferometer system will be described in 3.1.1. The measurement modes and the mathematical interpretation of the obtained MFM images are illustrated in 3.2 and 3.3.2, respectively.

### 3.1.1 The Low Temperature Scanning Force Microscope: LTSFM

The LTSFM-instrument is designed for multimode SFM operation in UHV, at low temperatures and in high magnetic field using fiber-optic interferometry as a sensor for the cantilever deflection. The UHV-system consists of two main UHV-chambers which can be separated by a valve: The preparation chamber is used for sample/cantilever preparation and standard surface science analysis whereas the microscope chamber is used mainly for sample/cantilever exchange. The latter is attached to the cryostat and contains the microscope and a UHV-manipulator for sample/cantilever exchange. A schematic side-view of the whole UHV-system is shown in Fig. 3.1 (a). The microscope position can be changed from the measurement position in the cryostat to the manipulation position in the microscope chamber using a bellows-system. Prior to the measurement, samples and cantilevers can be prepared in the preparation-chamber which contains a coolable and heatable xyz-manipulator, a triple electron-beam evaporator, a sputter gun, a mass spectrometer and a crystal cleaver. All magnetic cantilevers used in this thesis have been prepared in situ by means of e-beam evaporation of a thin Co-layer. Samples can be analysed by low energy electron diffraction (LEED) and Auger electron spectroscopy. Using a transport system, samples and cantilevers can easily be transferred from one chamber to the other. The whole UHV-system is mounted on a passively and actively damped table in order to compensate for floor vibrations.

A cross section of the cryostat containing the SFM is shown in Fig. 3.1 (b). The cryostat was custom designed by Oxford Instruments and is a superinsulated bath cryostat with a UHV compatible, variable temperature insert. Additionally, it contains a superconducting magnet system producing magnetic fields up to 7 T perpendicular to the sample surface. Most frequently used measurement temperatures were around 8 K. To stabilise temperature, a temperature sensor and a heater element placed near the sample are connected to a digital feedback loop. This leads to a temperature stability of about 0.5 mK. All the electrical connections and the optical fibre are guided along the cryostat insert. The microscope is spring suspended at the end of the cryostat-insert and its spring-suspension is eddy current damped.

A schematic drawing of the microscope and its measurement principles is shown in Figure 3.2. The sample is mounted on a piezo tube that performs the scan motion in  $x$ ,  $y$  and  $z$  directions. Below the cantilever chip a dither piezo actuates the cantilever to oscillate at a given frequency  $f$  and amplitude  $A$ . The deflection of the cantilever is detected by means of a fiber-optic interferometer. Therefore a cleaved optical fibre-end has to be brought close to the backside of the cantilever. The interferometer electronics converts the optical signal into an electronic signal (measurement signal) which is sine-shaped and proportional to the laser intensity. The frequency of the sine wave corresponds to the cantilevers actual oscillation frequency whereas the amplitude of the sine wave is proportional to the

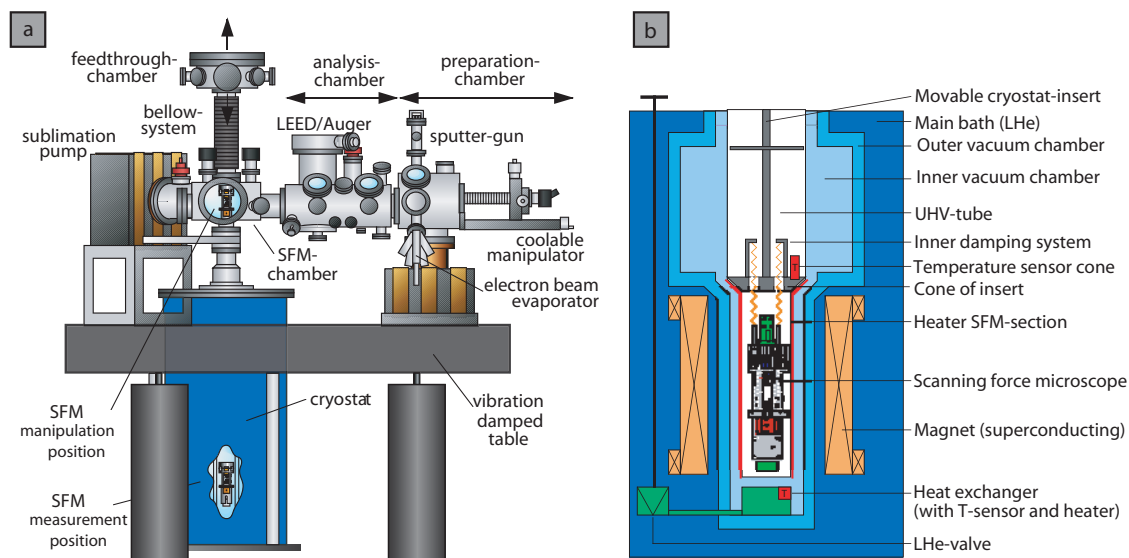


Figure 3.1: Schematics of the UHV system (a) and cross section of the cryostat (b): the UHV system consist of two separable chambers, the microscope chamber and the preparation chamber. The microscope is attached to the cryostat insert. Over the bellows-system it can be moved from the manipulation position to the measurement (cooling) position. The preparation-chamber is separated from the microscope chamber by a valve and contains several preparation tools and analysis methods (a). The cryostat (b) is a custom designed superinsulated bath cryostat. The microscope is shown in the measurement (cooling) position, where a copper cone attached to the cryostat insert is pressed into its cooled counterpart of the cryostat.

cantilevers oscillation amplitude  $A$ . The amplitude can be calculated from the wavelength of the laser light. However,  $A$  has to be smaller than a quarter of the laser's wavelength and the distance  $L$  between fibre end and cantilever has to be kept constant. This is done with a third piezo, the so-called fibre piezo which is operated in a feedback loop to keep the fibre-cantilever distanced constant. The system of cantilever and the optical fibre are tilted with respect to the sample surface by an angle of  $\theta = 12^\circ$  in order to not touch the sample surface with the cantilever chip.

The goal of the electronics is to drive the cantilever at its resonance frequency  $f_0$  with a constant amplitude  $A_0$  and to measure the frequency shift  $\Delta f$  of the cantilever induced by the force interaction. Many methods are used to determine the  $\Delta f$  of the oscillating cantilever and to control the distance between tip and sample. The present microscope is operated with a phase-locked loop (PLL) developed by Loppacher et al.[44] at the university of Basel. As the name of phase-locked loop implies, a PLL circuit keeps the phase between the cantilever and a reference oscillator locked. This is done by a feedback loop which compares the phases of the cantilever oscillation and the reference signal. The phase difference is then fed back with a loop gain  $g$ , to adjust the phase of the reference oscillator to the same phase as the cantilever. The resonance frequency of the cantilever can

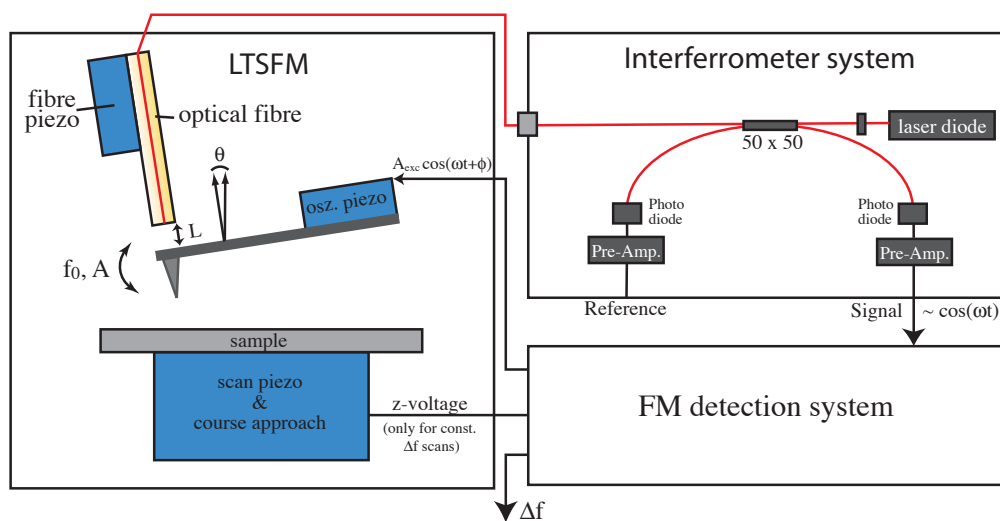


Figure 3.2: Principles of Scanning force measurements (SFM) (a) and interferometric detection of the cantilever motion (b): The cantilever is driven by the oscillation (dither) piezo at a the frequency  $f_0$  and the amplitude  $A$ . The fibre optical-interferometer system detects the cantilevers motion and converts the optical signal in an electronic one.

be measured with a relative accuracy exceeding 1 ppm (parts per million). In addition to the phase locked loop, an amplitude feedback loop is integrated in the electronics. The recorded data comprises the frequency shift  $\Delta f$ , the oscillation amplitude  $A$ , the cantilever excitation (voltage applied to the oscillation piezo) and the variation in tip-sample distance (voltage applied to z-piezo).

### 3.2 MFM Operation Modes

The LTSFM is well suited to perform measurements in various static (dc) and dynamic (ac) modes of measurement. In the dc modes the static deflection of the cantilever is detected. The feedback system then is either switched to the  $z$  direction of the scan piezo (constant-force mode) or to the fiber piezo (variable deflection mode). In the ac modes the cantilever is oscillated by a small piezo plate located inside the cantilever holder and below the cantilever. An FM detector [44] is used to detect the amplitude and phase of the forced cantilever oscillation. In this thesis, only dynamic operation modes have been used. A complete description of the two major dynamic force microscopy (DFM) modes, amplitude modulation and frequency modulation is given in [45]. The relationship between tip-sample forces and frequency shifts as recorded in the constant amplitude mode of DFM will be discussed in the following section (3.2.1).

In most SFM experiments, the tip-sample distance is controlled to keep the measured tip-sample interaction constant. However, magnetic forces are attractive and repulsive within the imaged sample area and therefore do not fulfil a condition of feedback stability of this mode which is that the derivative of the measured interaction must not change its sign

within the scanned image. Consequently, other methods for tip-sample distance control were developed. Here a group of operation modes will be presented which are based on a distance control relying on a non-magnetic interaction force.

In principle a wide variety of physical interactions, such as a constant tunnelling current, the tip-sample capacity or so-called lift-off techniques based on van der Waals forces (topography) can be used for distance control. In the nowadays widespread lift-off techniques, the topography of a magnetic sample is measured previous to the actual measurement of the magnetic signal. This is most simply achieved if the tip is brought into contact with the sample. Once the topography has been measured, the data can be used to keep the local tip-sample distance constant during a second scan of the sample area. Then the magnetic tip-sample interaction is recorded.

For rather flat samples, a magnetic image can also be acquired with the tip scanning parallel to the average tilt of the sample surface. All MFM images in this thesis were acquired in this way such that the image represents a frequency shift map taken at a constant average tip-sample distance  $z$ . Scanning parallel to the sample surface is achieved by adding an appropriate fraction of the  $x$  and  $y$  scan signals to the  $z$  direction. The exact fractions can be found by the previously measured topography or alternatively be found iteratively. A first MFM image is acquired at a sufficiently large tip-sample distance to avoid the tip crashing into the sample. Then the tip-sample distance is gradually reduced until a magnetic or van der Waals force induced signal appears in one of the corners of the image. The sample tilt and the tip-sample distance can then be adjusted to obtain an MFM image that shows an optimised homogeneous contrast. Furthermore, the tip-sample distance is adjusted to a sufficiently small negative frequency shift in order to avoid the mapping of topographic artefacts. This is done in the so-called true non-contact mode which usually requires a phase-locked loop to oscillate the cantilever on resonance with a constant amplitude (see 3.1.1).

### 3.2.1 Modelling Dynamic Force Microscopy

Some fundamental concepts needed to understand the dynamics of an oscillating cantilever in proximity of the surface will now be given. A suitable theoretical model for a vibrating cantilever is a damped, driven oscillator. Its equation of motion in one dimension is described by a non-linear, second-order differential equation

$$m\ddot{z} + \frac{m\omega_0}{Q}\dot{z} + c_L z = F_{ts}(z) + F_{exc} \cos \omega t \quad (3.1)$$

where  $F_{exc}$  is the driving force of the oscillation and  $\omega$  is the angular frequency of the driving force.  $Q$ ,  $\omega_0$  and  $c_L$  are the quality factor, angular resonance frequency and force constant of the free cantilever, respectively.  $F_{ts}$  is the tip-surface interaction forces. In the absence of tip-surface forces  $F_{ts}(z)=0$ , Eq. 3.1 is the equation of a forced harmonic oscillator with damping and its solution has a transient term and a steady state solution. The steady state term is a sinusoidal function with a phase lag with respect to the excitation force. The dependence of the oscillation amplitude  $A$  on the excitation frequency

is a Lorentzian expression

$$A(\omega) = \frac{F_{exc}/m\omega_0^2}{\sqrt{\left(1 - \frac{\omega^2}{\omega_0^2}\right)^2 + \left(\frac{\omega}{\omega_0 Q}\right)^2}} \quad (3.2)$$

where the amplitude for  $\omega = \omega_0$  is given by  $A(\omega = \omega_0) = F_{exc}Q/m\omega_0^2$ .

Let us assume that the tip is under the influence of a parabolic tip-surface interaction potential. Then the total force acting on the tip  $F$  can, for small displacements with respect to the equilibrium position, be expressed by

$$F = F_0 + \left(\frac{dF}{dz}\right)_{z_0} (z - z_0) \quad (3.3)$$

where  $F$  includes the elastic response ( $c_L z$ ) and the interaction force  $F_{ts}$ . It describes the motion of a harmonic oscillator with an effective spring constant  $c_{eff}$  given by

$$c_{eff} = -\frac{dF}{dz} = \left(c_L - \frac{dF_{ts}}{dz}\right)_{z_0}. \quad (3.4)$$

Out of this, the new effective resonance frequency can be calculated using

$$\omega_{eff} = 2\pi f_{eff} = \sqrt{\frac{c_{eff}}{m}} \quad (3.5)$$

$$f_{eff} = f_0 \cdot \sqrt{1 - \frac{1}{c_L} \left(\frac{dF_{ts}}{dz}\right)_{z_0}}. \quad (3.6)$$

In an MFM experiment the change in resonance frequency is seldom more than 1 % of the resonance frequency, so the above relation can be further simplified to

$$\frac{\Delta f}{f_0} = -\frac{1}{2c_L} \frac{dF_{ts}}{dz} \quad (3.7)$$

with  $\Delta f = f_{eff} - f_0$ . This shows that the resonance frequency of a perturbed harmonic oscillator depends on the gradient of the interaction force. A change in the effective resonance frequency implies a shift of the whole resonance curve according to Eq. 3.2 where  $\omega_0$  is replaced by  $\omega_{eff}$ . The resonance curve (Eq. 3.2) for a single harmonic oscillator and under the influence of attractive and repulsive forces is shown in Fig. 3.3. Note that the resonance curve of a perturbed harmonic oscillator is only shifted without introducing any shape or size modifications.

To resume, the limitations of harmonic models to describe dynamic AFM can be traced back to the implicit assumptions used to derive the Eq. 3.7. First it was assumed that tip-surface forces induce a frequency shift and not an energy transfer. In a MFM experiment, this is the case, as long as the magnetisation of the tip, and the distribution of the stray field of the sample do not change with the tip-sample position (see section 3.3). Second, the force gradient was assumed to be constant over all tip positions during the oscillation. This assumption is experimentally most often violated due to the use of too large oscillation amplitudes. Third, the force gradient has to be smaller than the cantilever force constant  $dF_{ts}/dz \ll c_L$ .



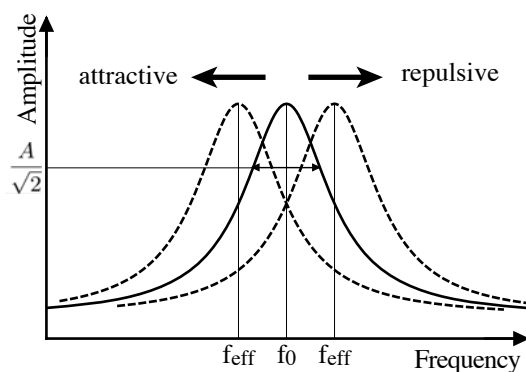


Figure 3.3: Resonance curve for a harmonic oscillator (solid line) and under the influence of attractive and repulsive forces (dashed lines). The force gradient of an external force shifts the free resonance curve without introducing any shape of size modification (weakly perturbed harmonic oscillator model).

### 3.3 Contrast Formation in MFM

The force acting on the tip in a MFM experiment is given by the convolution of the tip magnetisation distribution with the sample stray field. However, this is only true if the magnetisation patterns of the tip and the sample remain in their initial states after tip and sample have been brought into close proximity. In practice, the localised magnetic field produced by the magnetisation distribution of the tip may affect the magnetic structure of the sample and vice versa. For example, if the sample is a recording material, its micromagnetic state is not noticeably modified by the stray field of the tip, but the magnetisation of the tip may be influenced by the magnetic field of the sample. On the other hand, when imaging soft magnetic samples, the stray field of the tip often influences the magnetisation of the sample. Depending on the extent of modification of the tip magnetisation and the sample stray field, contrast formation processes in MFM can be divided into the following categories: (1) Negligible modifications, as long as the magnetisation of the tip and the stray field distribution of the sample do not change with the tip-sample position. (2) Reversible modification, if the distribution of the stray field of the sample or the magnetisation of the tip changes reversibly with the tip-sample position. (3) Hysteretic, or irreversible modifications are present if the magnetisation of the tip or the stray field distribution of the sample are changed irreversibly during the scan. The observed contrast does then not only depend on the actual tip-sample position but also on its history. Examples of MFM images exhibiting these modifications are shown in Chapter 4.

In the following section (3.3.1), the stray field distributions of a few simple magnetisation structures will be calculated. In addition, it will be shown that there is an infinite number of magnetisation patterns that generate the same stray field pattern. Thus, under the best conditions, only the stray field at the surface of the sample can be reconstructed from MFM data. A necessary condition for this is a sufficient knowledge of the magnetisation distribution of the tip. The tip magnetisation can be described either by simple point-pole

models or by geometrical models. Alternatively the response function of the tip can be determined from carefully designed calibration experiments (see section 3.3.2). If the stray field distribution of the sample and the magnetisation distribution of the tip are known, the force acting on the MFM tip can be computed (see section 3.3.2).

### 3.3.1 Magnetic Stray Field Calculation

The stray magnetic field emanating from the surface of any ferromagnetic sample can be calculated from [46]

$$\mathbf{H}(\mathbf{r}) = - \int_V \nabla \mathbf{M}(\mathbf{r}') \cdot \frac{\mathbf{r} - \mathbf{r}'}{|\mathbf{r} - \mathbf{r}'|^3} dV' + \int_A \mathbf{n} \cdot \mathbf{M}(\mathbf{r}') \cdot \frac{\mathbf{r} - \mathbf{r}'}{|\mathbf{r} - \mathbf{r}'|^3} dA' \quad (3.8)$$

where integrations are performed over the volume  $V$  and over the surface  $A$  of the sample, respectively.  $\mathbf{n}$  is the outward unit normal of the sample surface. It is noteworthy that a general vector field (e.g.  $\mathbf{M}(\mathbf{r})$ ) can be written as a sum of a divergence free ( $\nabla \mathbf{M}_{div} = 0$ ) and a curl free ( $\nabla \times \mathbf{M}_{rot} = 0$ ) part of  $\mathbf{M}$  i.e.  $\mathbf{M} = \mathbf{M}_{div} + \mathbf{M}_{rot}$ . Eq. 3.8 implies that only the divergence-free part of the magnetisation contributes to the stray field. Hence, MFM experiments will only provide information about the divergence-free part of the magnetisation field, the part of the magnetisation that generates the magnetic stray field. This is one reason, but not the only one, for the statement that there are an infinite number of magnetisation patterns which generate the same stray field pattern [47].

The area above the sample is current free and does not contain time-varying electrical fields, therefore the magnetic field is curl-free ( $\nabla \times \mathbf{H} = 0$ ) and can thus be expressed as the gradient of a scalar potential  $\phi$  with  $\mathbf{H} = -\nabla\phi$ . To calculate the magnetic scalar potential, it is useful to define the magnetic volume charge  $\rho_m$  and the magnetic surface charge  $\sigma_m$  in analogy with electrostatic fields by [47, 26]

$$\rho_m = -\nabla \mathbf{M} \quad (3.9)$$

$$\sigma_m = \mathbf{n} \cdot \mathbf{M}. \quad (3.10)$$

Outside the sample the magnetisation is zero, therefore the Laplacian of the scalar potential is equal to zero

$$\nabla^2 \phi = \Delta \phi = 0. \quad (3.11)$$

The magnetic scalar potential can then be calculated in 2D-Fourier space using the boundary conditions

$$\Delta \phi = -\rho_m \quad \text{inside the sample,} \quad (3.12)$$

$$\frac{\partial \phi_{-0}}{\partial n} - \frac{\partial \phi_{+0}}{\partial n} = \sigma_m \quad \text{on the surface of the sample} \quad (3.13)$$

and taking into account that the nabla operator in 2D-Fourier space is described as  $\nabla = (ik_x, ik_y, \partial/\partial z)$ . The solution of Eq. 3.11 is then

$$\phi(\mathbf{k}, z) = \phi(\mathbf{k}, 0) \cdot e^{-kz} \quad (3.14)$$

with  $k = \sqrt{k_x^2 + k_y^2}$ . Note that only the  $x$  and  $y$  coordinates of the coordinate triplet  $(x, y, z)$  are transformed. As a consequence the coordinates are given as  $(\mathbf{r}, z)$  where the

vector  $\mathbf{r} = (x, y)$  is two-dimensional and correspondingly  $(\mathbf{k}, z)$  with  $\mathbf{k} = (k_x, k_y)$ . In accordance with general practice, the same name and symbol will be used in direct space and in Fourier space, in spite of different units.

Outside the sample where the Laplace equation 3.11 holds, the nabla operator can be further simplified to  $\nabla = (ik_x, ik_y, -k)$ . Hence the  $z$  component of the Fourier transform of the stray field is simply given by [26]

$$\phi(\mathbf{k}, z) = -\frac{1}{k} H_z(\mathbf{k}, z). \quad (3.15)$$

Note that the Fourier transform of the scalar potential is fully determined by each of the components of the field. For example, it is fully sufficient to measure the  $z$  component of the magnetic field, because the  $x$  and  $y$  components can be calculated from

$$\mathbf{H}(\mathbf{k}, z) = -\frac{\nabla}{k} H_z(\mathbf{k}, z). \quad (3.16)$$

### Stray Field of a Thin FM Layer

In order to understand MFM image formation and hence also the interpretation of MFM images, it is instructive to calculate the stray field of a slab-like sample with thickness  $t$  but infinite planar dimensions. The top surface is at  $z = 0$  and the bottom surface is then at  $z = -t$ . The magnetisation will vary in  $x$  and  $y$  but remains perpendicular to the surfaces of the sample,  $\mathbf{M} = (0, 0, \pm M_z(x, y))$ . Such a sample has only magnetic surface charges on the top and bottom surfaces and these are equal to  $\pm M_z$ . The boundary conditions then become  $H_z|_{z=+0} = 1/2M(x, y)$  and  $H_z|_{z=-t+0} = -1/2M(x, y)$ . Note that the factor  $1/2$  arises from the fact that the magnetic surface charge generates a stray magnetic field above the upper surface of the sample (outside) and the demagnetising field of the same size but opposite direction below the upper surface of the sample (inside). Using Eq. 3.14 and the boundary conditions, the Fourier components of the stray field components become

$$H_{x,y}(\mathbf{k}) = \frac{e^{-k \cdot z} \cdot (1 - e^{-k \cdot d})}{2ki} \cdot M_z(\mathbf{k}) = HTF_{x,y}(z) \cdot M(\mathbf{k}) \quad (3.17)$$

and

$$H_z(\mathbf{k}) = \frac{e^{-k \cdot z} \cdot (1 - e^{-k \cdot d})}{2} \cdot M_z(\mathbf{k}) = HTF_z(z) \cdot M(\mathbf{k}) \quad (3.18)$$

where  $t$  is the sample thickness,  $M(\mathbf{k})$  is the Fourier transform of the magnetisation  $M_z(\mathbf{r})$  and  $HTF_{x,y}(z)$  and  $HTF_z(z)$  are transfer functions transforming the Fourier transform of the magnetisation to that of the  $xy$  and  $z$  components of the field, respectively.

### Stray Field of an Atomically Thin FM Layer

A perfect, thick antiferromagnet does not of course exhibit any magnetic stray field, because all magnetic moments are compensated. However, as explained in section 2.1.4, thin antiferromagnetic films may contain uncompensated magnetic moments which may generate a magnetic stray field. The most straight forward situation creating uncompensated

spins (UCS) in an AFM is an odd number of antiferromagnetically coupled spin planes as illustrate in Fig. 2.4 (b) and (c). Necessarily, one of these atomically thin spin planes will be uncompensated and therefore generate a magnetic stray field. Defects may also generate such uncompensated spins. The stray field  $H_z^{atomic}$  of such a atomically thin layer of ferromagnetically aligned spins is different from the one of the thin FM layer derived above and shall be derived here. In a first approach, the stray field of an atomically thin layer can be written in analogy to the stray field of a thin FM layer (see Eq. 3.18) as

$$H_z^{atomic}(\mathbf{k}) = \frac{e^{-kz} \cdot (1 - e^{-kd_{atom}})}{2} \cdot \left[ \frac{\sum_i m_i}{A \cdot d_{atom}} \right] (\mathbf{k}), \quad (3.19)$$

where  $m_i$  is the magnetic moment per atom,  $A$  the unit area,  $z$  is the distance and  $d_{atom}$  is the thickness of one atomic layer. As  $d_{atom}$  is only a few angstroms the equation can be simplified by using  $e^{-kd_{atom}} \approx 1 - kd_{atom}$  and Eq. 3.19 becomes

$$H_z^{atomic}(\mathbf{k}) = \frac{e^{-kz} \cdot k}{2} \cdot \left[ \frac{\sum_i m_i}{A} \right] (\mathbf{k}), \quad (3.20)$$

which can now be compared to Eq. 3.18: the so-called thickness-loss factor  $(1 - e^{-k \cdot d})$  was reduced to only  $k$ . Numerically it can be calculated that for a periodic stripe domain pattern with a wavelength of 200 nm the factors become almost equal below a thickness of  $d = 1$  nm. Furthermore the magnetisation distribution  $M_z(\mathbf{k})$  in Eq. 3.18 became the distribution of  $\sum_i m_i/A$ , the magnetic moments per unit area in Eq. 3.20.

### 3.3.2 Computing the Force on the Magnetic Tip

If a modification of the tip and/or sample magnetisation can be neglected, the force action of the magnetic tip is given by the convolution of the tip magnetisation distribution with the sample stray field. In real space this convolution is performed by a three-dimensional integration for each position of the tip above the sample. Although a study of the equations is useful for understanding MFM image formation, the practical use of these equations is rather limited. A more practical approach was developed in Fourier space and will be described in more detail in this section.

#### Calculation in Direct Space

The force acting on a magnetised tip can be calculated from the magnetostatic energy of the tip/sample system:

$$E(x, y, z) = \int_{-\infty}^{\infty} \mathbf{M}_{tip}(x', y', z') \cdot \mathbf{H}_{sample}(x + x', y + y', z + z') dV' \quad (3.21)$$

where the integration is performed in the primed coordinate system attached to the tip (the non-primed coordinate system is attached to the sample surface). The  $z$  component of the force acting on the tip then becomes

$$F_z(x, y, z) = -\mu_0 \int_{-\infty}^{\infty} \mathbf{M}_{tip}(x', y', z') \cdot \frac{\partial}{\partial z} \mathbf{H}_{sample}(x + x', y + y', z + z') dV'. \quad (3.22)$$

The other components of the force are easily evaluated by replacing the derivative in Eq. 3.22 by the corresponding lateral derivatives.

### Calculation in Fourier Space: Transfer-Function Theory

If one now calculates the force in 2D-Fourier space, the x-y-part of the correlation integral in Eq. 3.22 is replaced by a multiplication:

$$F(\mathbf{k}, z) = \mu_0 \int_{-\infty}^{\infty} \mathbf{H}_{sample}(\mathbf{k}, z') \nabla' \cdot -\mathbf{M}_{tip}^*(\mathbf{k}, z' - z) dz' \quad (3.23)$$

$$= \mu_0 \int_{-\infty}^{\infty} \mathbf{H}_{sample}(\mathbf{k}, z' + z) \nabla' \cdot -\mathbf{M}_{tip}^*(\mathbf{k}, z') dz' \quad (3.24)$$

with \* denoting the complex conjugate. Using Eq. 3.14, one gets:

$$F(\mathbf{k}, z) = \mu_0 \mathbf{H}_{sample}(\mathbf{k}, z') \int_{-\infty}^{\infty} e^{-kz'} \nabla' \cdot -\mathbf{M}_{tip}^*(\mathbf{k}, z') dz' \quad (3.25)$$

$$= \mu_0 \mathbf{H}_{sample}(\mathbf{k}, z') \cdot \sigma_{tip}^*(\mathbf{k}), \quad (3.26)$$

with  $\sigma_{tip}^*(\mathbf{k})$  being the Fourier transform of a tip-equivalent surface charge pattern, with the surface charges located in a plane at the apex of the MFM tip, parallel to the sample surface. The stray field of the tip below the plane containing the equivalent charge distribution can be calculated from  $\sigma_{tip}^*(\mathbf{k})$  using the expression:

$$\mathbf{H}_{tip}(\mathbf{k}) = -\frac{1}{2} \begin{pmatrix} -ik_x/k \\ -ik_y/k \\ 1 \end{pmatrix} \cdot e^{k(z'-z)} \cdot \sigma_{tip}(\mathbf{k}) \quad (3.27)$$

with  $z$  the distance of the tip to the sample, and  $z' < z$  the distance of the field to the sample. If one wishes to calculate the force on the tip from the field of the sample, one needs to know the behaviour of  $\sigma_{tip}$ . A procedure for determining  $\sigma_{tip}$  is given in section 3.3.3 and the tip-field at ( $z = z'$ ) of all the MFM tips used in this thesis is calculated in section 4.1.2 using the expression  $H_{tip}(z = z') = -1/2 \cdot \sigma_{tip}(\mathbf{k})$ .

### The Relation Between the Force and the Measured Contrast

From the force vector, one must now derive the measured quantity in the MFM experiment, which is either the force  $F_n(\mathbf{k})$ , or its derivative  $dF_n(\mathbf{k})/dn$  which is measured in DFM (see section 3.2.1), in the direction of the normal to the cantilever surface. This direction is characterised by the vector  $\mathbf{n} = (0, \sin\theta, \cos\theta)$ , with  $\theta$  the canting angle between the normal of the lever and the normal of the sample surface (see Fig. 3.2). In [24] it was derived that

$$\frac{d}{dn} F_n = \mathbf{n} \cdot \nabla(\mathbf{n} \cdot \mathbf{F}). \quad (3.28)$$

Inserting Eq. 3.26 and 3.16 into Eq. 3.28, one obtains

$$\frac{d}{dn} F_n = (\mathbf{n} \cdot \mathbf{F}) F_n(\mathbf{k}) = -k\mu_0\sigma_{tip}^*(\mathbf{k}) [LCF(\mathbf{k}, \theta)]^2 H_z(\mathbf{k}), \quad (3.29)$$

where  $LCF(\mathbf{k}, \theta)$  is the lever canting function, which describes the effect of the canting angle of the lever on the measurement.

### Instrument Calibration Function

It is useful to define an *Instrument Calibration Function*  $ICF(\mathbf{k})$  in addition to  $\sigma_{tip}(\mathbf{k})$  to describe the imaging properties of the instrument. The  $ICF$  gives the relation between the sample stray field derivative and the measured quantity (frequency shift:  $\Delta f$ ), and can directly be determined from calibration measurements. In addition,  $\sigma_{tip}(\mathbf{k})$  can only be determined from calibration measurements if one knows the canting angle and the mechanical properties of the cantilever. Here the  $ICF$  will be defined as the function which relates the stray field derivative to the measured resonance frequency shift and will therefore be called  $ICF_{dH_z}^{\Delta f}(\mathbf{k})$ . Using Eq. 3.7 and 3.29, one finds

$$ICF_{dH_z}^{\Delta f}(\mathbf{k}) = -\frac{f_0}{2c}\mu_0\sigma_{tip}^*(\mathbf{k})[LCF(\mathbf{k}, \theta)]^2, \quad \text{with} \quad (3.30)$$

$$\Delta f(\mathbf{k}) = ICF_{dH_z}^{\Delta f}(\mathbf{k}) \cdot \frac{d}{dz}H_z(\mathbf{k}), \quad (3.31)$$

which is used in the following section to calibrate the MFM tip.

### 3.3.3 Calibration of an MFM Tip

The calibration of the MFM tip is a prerequisite for the quantitative analysis of an MFM measurement. The aim of the procedure is the determination of the  $ICF$  defined in Eq. 3.30 which includes the magnetic imaging properties of the tip as well as the mechanical properties of the system. In addition, the calibration procedure developed by van Schendel et al [26, 27], does not need any assumptions about the distribution of the magnetic charges on the tip. However, the choice of the calibration sample is important for the calibration process developed by van Schendel et al. The magnetisation direction should be perpendicular to the sample plane and homogenous throughout the film thickness. In addition, the saturation magnetisation value has to be known precisely for various measurement temperatures. The tip/sample interaction must be negligible (see section 3.3). Finally, the size distribution of the magnetic domains should be homogenous for domain sizes ranging from a few hundred nanometers to less than 10 nm. The calibration samples used in this thesis were: (1) a perpendicular magnetic recording sample exhibiting a strong perpendicular anisotropy in which tracks of various bit densities have been written. The bit length ranges from 2  $\mu\text{m}$  down to 35 nm. Besides the tracks, very small domains are formed (see Fig. 3.4 (a)). (2) the samples presented in section 5.2.1 do also exhibit a strong perpendicular anisotropy and their saturation magnetisation could be determined from hysteresis loop measurements of various temperatures (see section 5.2.3). Therefore they could also be used for some of the calibration measurements.

The calibration procedure is based on Eq. 3.31. The  $ICF$  can be calculated from an MFM measurement if the stray field of the sample is known. The latter relies on the magnetisation distribution inside the sample and can easily be determined by applying a discrimination procedure to an MFM image (see Fig. 3.4 (b)). From the magnetisation pattern, the z-derivative of the stray field was computed (see Fig. 3.4 (c)) in a plane parallel to the sample surface, touching the apex of the tip (using Eq. 3.18). The  $ICF_{dH_z}^{\Delta f}(\mathbf{k})$  is then obtained by a division of the Fourier components of the measurement by those of the stray field derivative (Fig. 3.4 (d)). Calibration errors due to sample topography

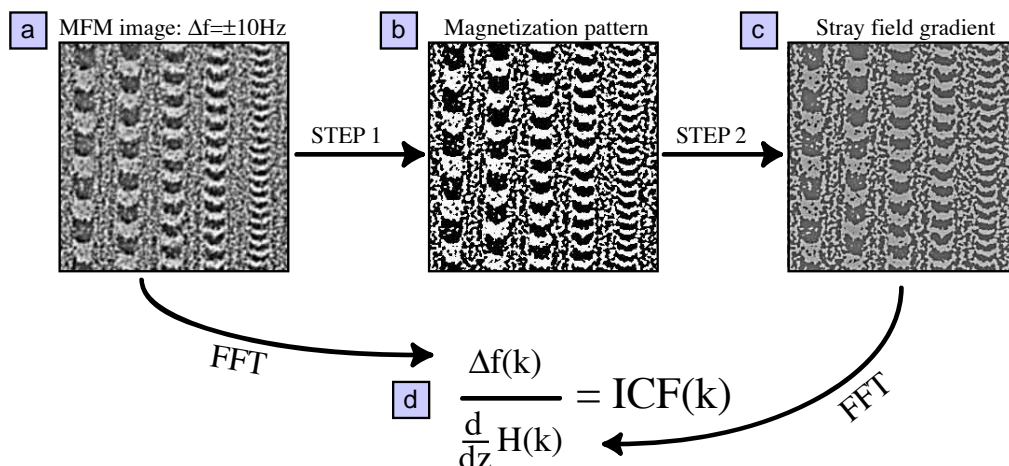


Figure 3.4: Procedure to calibrate an MFM tip: A calibration measurement is done on a sample exhibiting a perpendicular anisotropy and a large distribution of magnetic domain sizes. Furthermore the saturation magnetisation has to be well known (a). The magnetisation pattern is determined by a discrimination procedure (b). From the magnetisation pattern the stray field gradient is calculated using Eq. 3.18 (c). Finally the *ICF* is calculated by dividing the FFT of the MFM-image by the FFT of the stray field gradient (d).

and uncertainties in the magnetisation estimate can be reduced by averaging over several calibration functions obtained from different MFM measurements.

A useful representation of the *ICF* is shown in Fig. 4.4. It is calculated by a circular average of the frequency components having different directions but the same wave vector  $k$  in Fourier space. The resulting spectrum is called *sensitivity spectrum* and permits the comparison of the sensitivity of the tip for different wave vectors or wavelength contained in the magnetisation pattern of the sample.

### 3.4 Vibrating Sample Magnetometer: VSM

In this section we briefly discuss the method used for measuring the hysteresis loops of a magnetic sample, i.e. its magnetic moment as a function of applied magnetic field. The most important magnetic parameters that characterise a magnetic material are those related to its hysteresis loop. The shape of a hysteresis loop can be used to determine the usefulness of a material for a particular application. Furthermore the values of the saturation magnetisation, coercivity, remanence, permeability or susceptibility can be deduced. From temperature dependent hysteresis loops we may also deduce the Curie or the Néel temperature of a sample.

The methods of measuring magnetisation fall into two categories. In the first category are methods that detect a current or voltage induced in a circuit placed close to a magnetic material in motion. To this category also belongs the so called vibrating sample

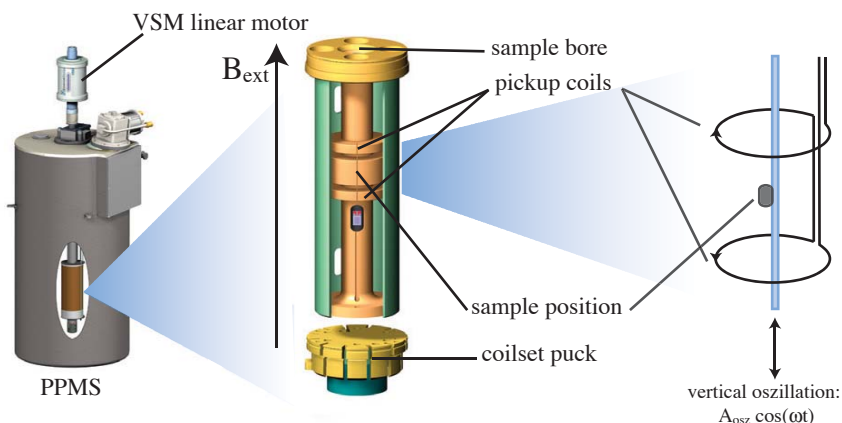


Figure 3.5: *Quantum Design Physical Properties Measurements System* (PPMS) with VSM option. The VSM option for the PPMS consists primarily of a linear motors transport head for vibrating the sample and a oppositely wound coil set for detection.

magnetometer (VSM) which was used to measure all hysteresis loops present in this thesis. In the second category fall measurements of the force on a magnetic specimen in an inhomogenous field. In a general sense even the MFM belongs to this group, even if it is not its actual aim to measure hysteresis loops.

The system used to measure all hysteresis loops presented in this sample is a *Quantum Design Physical Properties Measurements System* (PPMS) which contains among others a VSM option. The basic measurement is accomplished by oscillating the sample near a detection pickup coil and synchronously detecting the voltage induced. By using a first order gradiometer, consisting of two oppositely wound coils, a relatively large oscillation amplitude (1-3 mm peak) and a frequency of 40 Hz, the system is able to resolve magnetisation changes of less than  $10^{-10}$  A/m<sup>2</sup>. A superconducting coil, located in the cryostat operating from 300 K up to liquid helium temperatures, generates homogeneous field up to 14 T. A schematic of the PPMS with VSM option is shown in Fig. 3.5. The basic principle of operation of a VSM is that a changing magnetic flux will induce a voltage in the pickup coils. The definition of the magnetic flux is given by

$$d\phi = \vec{B}_S \cdot \vec{d}\vec{n} = B_S \cdot A \cos \alpha \quad (3.32)$$

where  $B_S$  is the magnetic field produced by the sample, and  $\vec{d}\vec{n}$  is the the vector perpendicular to the sample area  $A$ . For a sinusoidally oscillating sample position and  $\vec{B}$  parallel to  $\vec{d}\vec{n}$ , the magnetic flux becomes

$$d\phi = \underbrace{CmA_{osz} \cos \omega t}_{B_S} \cdot A \quad (3.33)$$

where  $C$  is a coupling constant,  $m$  is the magnetic moment of the sample,  $A_{osz}$  is the amplitude of oscillation, and  $\omega = 2\pi f$  is the angular frequency of oscillation. Applying Faradays law of induction  $U_{ind} = -\dot{\phi}$ , it is found that the induced voltage in the pickup



coils is given by

$$U_{ind} = \omega C m S A_{osz} \sin \omega t. \quad (3.34)$$

The acquisition of magnetic moment measurements involves measuring the coefficient of the sinusoidal voltage response from the detection coils. A hysteresis loop measurement consists in measuring the magnetic moment  $m$  as a function of externally applied field  $B_{ext}$  generated by a superconducting coil.

Prior to a hysteresis loop measurement, the sample is often brought into a demagnetised state. A frequently used method to demagnetise a material is to apply an oscillating magnetic field of gradually decreasing magnitude. However the surest method of all would be to heat the material above its Curie temperature and cool it down in zero applied field. A hysteresis loop then starts at zero magnetic moment in zero applied field. The magnetic moment then increases with increasing field until it reaches a constant value which corresponds to the saturation magnetisation  $M_s$ . This part of the hysteresis loop is called “juvenile loop”. Afterwards the field is decreased back to zero, where the magnetisation may still have a non-zero value, called remanent magnetisation  $M_{rem}$ . A field in the opposite direction is then applied until the magnetisation again reaches zero, this field is called coercive field  $H_C$ . If we continue to change  $H$  between large enough values in opposite directions,  $m$  will vary repeatedly along the a closed loop which is called *hysteresis loop*. Many examples of hysteresis loops measured in this thesis can be found in section 5.2.3.

### 3.5 Transmission Electron Microscopy: TEM

All the TEM images presented in this thesis were done by M. Parlinska-Wojtan with an *Philips CM 300* high resolution TEM at the EPFL. The transmission electron microscope operates on the same basic principles as the optical ‘light’ microscope but uses electrons instead of light. What you can see with a light microscope is of course limited by the wavelength of light. TEMs use electrons instead of a classical light source and their much lower wavelength makes it possible to get a resolution of a few Angstroms. The sample you want to look at must be of such low density that it allows electrons to travel through. Therefore only a few nanometer thick sample slices have to be prepared which can be a quite difficult task. Our samples were usually first mechanically polished and then ion beam milled. The images were taken in bright-field mode.

The electrons are emitted at the top of the microscope and travel through the vacuum column of the microscope. Instead of glass lenses focusing light, The TEM uses electromagnetic lenses to focus the electrons into a very thin beam. The electron beam then travels through the specimen you want to study. Some electrons are scattered and disappear from the main beam. At the bottom of the microscope the different kinds of images can be formed by using unscattered or some or all of the scattered electrons hitting a fluorescent screen. The image can be studied directly by the operator or photographed with a camera. The way how to choose which electrons will form the image is to insert an aperture into the back focal plane of the objective lens. If the direct beam is selected the resultant image is called a bright-field image. If we select scattered electrons of any form, it is called a dark-field image. All images presented in this thesis are bright-field images.

## Chapter 4

# Improvement of Methods: Hardmagnetic MFM-Tips

A key requisite of all MFM experiments is to fabricate a suitable MFM tip. One might think that the most important property of an “ideal” MFM-tip is to image the magnetic sample with a high spatial resolution. However, there are at least two other properties that an ‘ideal’ MFM-tip should have: a hard magnetic coating and a small magnetic flux emanating from the tip. The former is necessary because the magnetisation distribution of a magnetically soft tip can easily be modified by the stray field of the sample while imaging. The latter property prevents modification of the sample magnetisation distribution by the stray field of the MFM-tip. To fulfil the third property of an “ideal” tip, the flux density should be “large enough” in a small area close to the end of the tip, to obtain high resolution and sensitivity.

Three parameters can be varied in order to obtain the ‘ideal’ MFM tip: the shape of the non-magnetic tip, the material of the magnetic coating and its thickness. In this work high aspect ratio, cone shaped tips were used. They achieve a resolution which is reproducibly below 20 nm which is largely sufficient for most samples. More problematic is the “stability” of the magnetic coating of the tip: it can often be observed that the stray field of the sample is strong enough to induce changes in the magnetisation distribution of the tip during the scan motion (see section 3.3). A solution to this problem is to increase the coercivity of the magnetic coating of the tip. However, at the same time the magnetic flux should be kept approximatively constant in order to not induce modification of the magnetisation state of the sample. Therefore the thickness of the layer should not be increased.

As shown in section 2.1.1, the coercivity of a FM layer can be drastically increased by coupling it to a AFM layer. If cobalt is used to coat the MFM-tips, an antiferromagnetic CoO-layer can easily be formed by ambient air oxidation. It could be shown that the formation of a CoO layer on a cobalt coated tip clearly increases the stability of the tip magnetisation.

## 4.1 Experiment and Results

The assumption that an antiferromagnetic CoO layer would strongly increase the stability of the magnetic tips was verified in a simple experiment: an MFM image is first taken with a “normal”, cobalt coated, MFM-tip. Then, before taking a second MFM image, the cobalt layer is oxidised some minutes in air. A comparison of the MFM images and the dissipation signal (voltage applied to the dither piezo in order to keep the oscillation amplitude constant) before and after the oxidation clearly reveals a stabilisation of the tip magnetisation.

### 4.1.1 Tip Preparation

The silicon tips used in this study were *Improved Super Cone (ISC)* tips commercially available from *Team Nanotech GmbH* [48]. The tips are cone shaped with a full cone angle  $\alpha \leq 10^\circ$ , a tip radius smaller than 10 nm and a tip height of about 9  $\mu\text{m}$ . The lever has a spring constant  $c_L$  of about 0.35 N/m and its free resonance frequency  $f_0$  is around 40 kHz. The front end of the cantilever was reflex coated on the backside with 30 nm of aluminium. The magnetic coating is evaporated in situ at a pressure of  $10^{-9}$  mBar using an electron beam evaporator. Only one side of the cone shaped tip is coated by evaporating at an oblique angle. The tip preparation and the mechanical properties of all tips are summarised in Table 4.1. All evaporations on the tips were done at room temperature. The three tested tips, named Tip1 to Tip3, were first covered with a 1 nm titanium seed layer. The initial cobalt coating of all tips was oxidised to CoO exposing them to ambient air for 13 minutes then the tips were immediately put back in UHV. Before imaging, all cobalt coated tips were magnetised along the tip vertical tip axis in a field of 1.5 T

Tip1 was covered with 2 nm of cobalt then magnetised. MFM images were taken on the so-called calibration sample, a perpendicular recording media (see section 3.3.3). In order to guarantee a sufficiently high flux density emanating from Tip1 after the oxidation, 2 nm of cobalt were additionally evaporated on top of the initial 2 nm before the oxidation. The second tip, Tip2, was initially covered with a 4.5 nm thick cobalt layer, such that it was not necessary to put an additional magnetic layer before the oxidation. MFM images were performed on the calibration sample, before and after oxidation. Furthermore, the quality factor of this cantilever was determined before and after the oxidation process.

Tip 3 was coated with 4.5 nm of Co, then magnetised and finally oxidised. Note that no MFM images were performed with this tip before the oxidation.

### 4.1.2 MFM Measurements on Harddisc Sample

In this section all MFM measurements done with Tip1 to Tip3 before and after oxidation are shown and analysed. In order to be able to compare the imaging properties of the tips, all MFM images were taken on the well known “calibration sample”, a perpendicular recording media. Images taken before and after the oxidation process will be referred to as ‘Before’ and ‘After’. Furthermore, images were taken at different sample positions showing tracks with high and low bit densities. For each measurement, the frequency shift signal (MFM image) and the corresponding dissipation signal are shown. The dissipation signal

Cantilever	Preparation	$f_0$ [Hz]	$c_L$ [N/m]	Q-Factor
Tip 1: Before After	1 nm Ti + 2 nm Co, 1.5 T 2 nm Co, 1.5 T, 13 min. in air	43'491.8	0.35	Q1
Tip 2: Before After	1nm Ti + 4.5 nm Co, 1.5 T 13 min. in air	35'984.1 35'980.2	0.35	26'850 13'800
Tip 3: After	1nm Ti + 4.5 nm Co, 13 min in air	40000 Hz	0.35	Q3

Table 4.1: Mechanical properties and description of preparation of the MFM-tips used in this thesis

is a voltage which is proportional to the energy loss per oscillation cycle of the cantilever. For negligible or reversible modifications of the tip and/or sample magnetisation the dissipation signal is constant and does not depend on the scan motion (see section 3.3).

With Tip1,  $2 \times 2 \mu\text{m}^2$  sized MFM images were taken at two different sample position exhibiting low and high bit densities. The images taken before and after the oxidation process are shown in Fig. 4.1 (a),(c) and (e),(g) respectively. The horizontal lines along the fast scan direction in the MFM images taken before the oxidation are a clear sign for an irreversible modification of the magnetisation distribution of the tip. A modification of the magnetisation distribution of the sample can be excluded due to its strong anisotropy. The dissipation signals corresponding to the images taken before and after oxidation are shown in Fig. 4.1 (b),(d) and (f),(h) respectively. Before oxidation, the energy dissipation of the oscillating cantilever clearly depends on the relative tip-sample position and on the history of the tip-sample position. No horizontal lines are visible in the MFM images taken after the oxidation and their dissipation signal is perfectly constant indicating that no energy was lost in hysteretic or irreversible modifications of the tip magnetisation during the scanning motion. The tip-sample distance was not measured for these images. However, from a comparison of the resolution of the 'Before' and 'After' images it can be deduced that the tip-sample distance of the images taken after the oxidation is similar or even smaller than than the tip-sample distance of the images taken before oxidation. However, this experiment does not fully prove that the stabilisation of the tip magnetisation is only due to the formation of an antiferromagnetic CoO layer during the oxidation. As explained in section 4.1.1, an additional 2 nm thick cobalt layer was deposited after having done the 'Before' measurements in order to guarantee a sufficient magnetic flux density of the tip after the oxidation. The additional cobalt layer might also be responsible for an increased stability, i.e a increased coercivity, of the tip after the oxidation. To rule out this possibility the following tip experiment was designed more carefully.

Tip2 was initially coated with 4.5 nm of cobalt such that the tip could be oxidised after the first measurements without further treatment. The change in imaging properties can then be directly attributed to the formation of an antiferromagnetic layer on top of a ferromagnet.  $3 \times 3 \mu\text{m}^2$  sized MFM images taken before and after oxidation at similar imaging heights and sample positions are shown in Fig. 4.2 (a) and (c), respectively. The modification of the tip magnetisation (tip-changes) visible in (a) above the bit transitions completely disappeared in (c), the image taken after oxidation. The corresponding dissipation images are shown in (b) and (d) respectively. The linecuts of the dissipation images

corresponding to the positions of the identically coloured lines drawn in (b) and (d) are shown in (e). As the dissipation signal is proportional to the energy loss per oscillation cycle of the cantilever, the amount of energy used to modify the tip magnetisation distribution can be calculated. Therefore the quality factor of the cantilever was measured before and after the oxidation (see Table 4.1). The quality factor can be defined as the energy stored in the cantilever ( $E_{stored}$ ) divided by the energy loss per oscillation cycle ( $E_{loss/cycle}$ ). The energy stored in a harmonic oscillator is given by

$$E_{stored} = \frac{1}{2}c_L A_{osz}^2, \quad (4.1)$$

where  $c_L$  is the spring constant of the cantilever and  $A_{osz}$  is the oscillation amplitude. Using the definition of the Q-factor, the energy loss per cycle can be written as

$$E_{loss/cycle} = \frac{E_{stored}}{Q} = \frac{c_L A_{osz}^2}{2Q}. \quad (4.2)$$

The oscillation amplitude  $A_{osz}$  as a function of the dissipation signal (voltage applied to the oscillation piezo) has a linear behaviour and was determined prior to the measurements. From this function and Eq. 4.2 the energy loss per cycle as well as the stored energy can be calculated. The average energy loss per cycle  $E_{loss/cycle}^{avg}$  was calculated from the

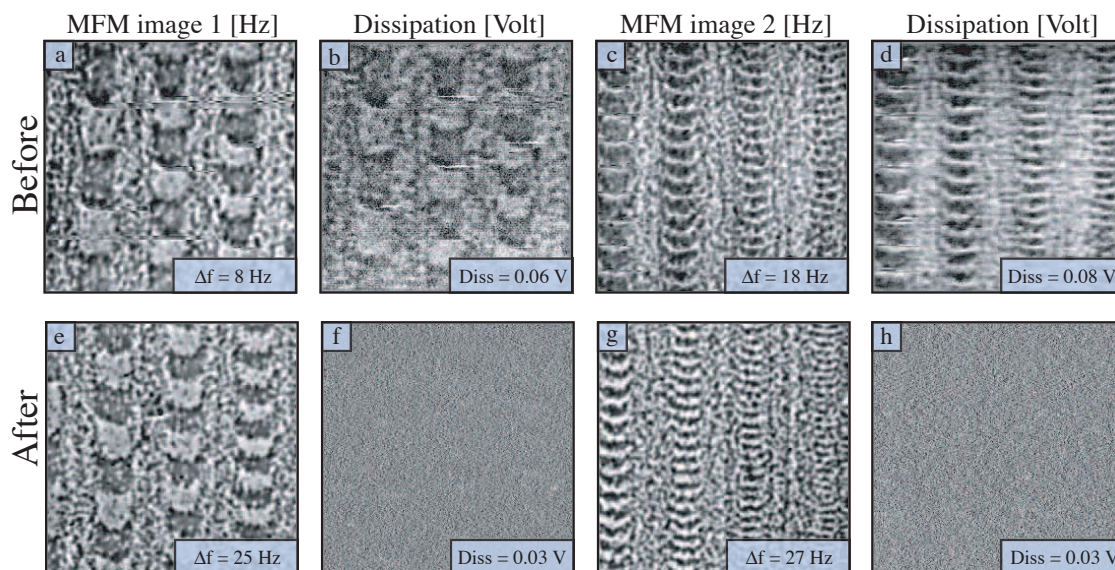


Figure 4.1:  $2 \times 2 \mu\text{m}^2$  sized MFM images taken before and after the oxidation of Tip1: the horizontal lines in the MFM images (a) and (c), taken before the oxidation are a clear sign of hysteretic or irreversible modifications of the tip magnetisation during the scan. The corresponding dissipation signal, in (b) and (d), reveals that the energy loss per oscillation cycle of the cantilever depends on the actual tip-sample position and its history. After the oxidation, the MFM images (e) and (g) do not show any horizontal lines and the corresponding dissipation images (f) and (h) are constant over the whole image.

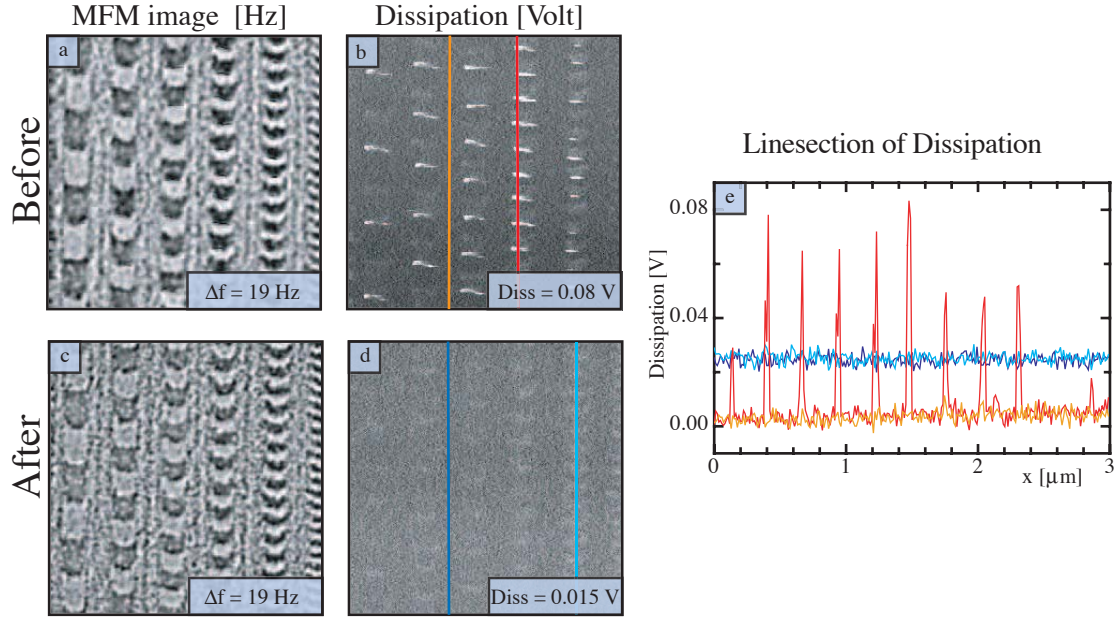


Figure 4.2:  $3 \times 3 \mu\text{m}^2$  sized MFM images taken before and after the oxidation of Tip2: the horizontal lines in the MFM image (a), taken before the oxidation are a clear sign of hysteretic or irreversible modifications of the tip magnetisation. The corresponding dissipation signal, in (b), reveals that the energy loss per oscillation cycle of the cantilever depends on the actual tip-sample position and its history. After the oxidation, the MFM images (c) does not show any horizontal lines and the corresponding dissipation images (e) is constant over the hole image. Panel (e) shows the linecuts through dissipation images indicated by the corresponding colour in (b) and (d).

linesections taken between two tracks (orange and dark blue lines in Fig. 4.2 (e)) assuming negligible modification of the tip magnetisation at this positions. Note that the average energy loss per cycle after oxidation was increased by about a factor of two, due to a decrease of the Q-factor by about a factor of two. The maximum energy loss per cycle  $E_{loss/cycle}^{max}$  was calculated from maximum values of the red and light blue coloured line sections in Fig. 4.2 (b),(d) and (e). All calculated energies are summarised in Table 4.2. The maximum energy dissipated before oxidation is about 22 times higher than the average energy loss per cycle. Comparing the average energy loss to the maximum energy

	$E_{stored}$ [meV]	$E_{loss/cycle}^{avg}$ [meV]	$E_{loss/cycle}^{max}$ [meV]
Tip 2: Before	12300	0.46	10.5
Tip 2: After	17100	1.24	1.24

Table 4.2: Calculated values of the stored and lost energies per cycle before and after the oxidation.

loss in MFM image done before the oxidation ( $E_{loss/cycle}^{max} - E_{loss/cycle}^{avg}$ ) one finds that about 10 meV are used to modify the tip magnetisation state during a tip-change. In section 4.3 this amount of energy is used to approximate the rotation angle of the tip magnetisation during a tip-change. After the oxidation, the magnetisation became stable such that the maximum energy loss is equal to the average energy loss during an oscillation cycle. Note that in this experiment the stability increase of the tip magnetisation can undoubtedly be accorded to the formation of the antiferromagnetic CoO, as no other parameters were varied.

For the sake of completeness, MFM images taken with the third tip used in this thesis shall also be presented even though measurements with this tip were only done after the oxidation process. They show a nice, stable tip, as expected from the previously prepared and tested tips. The  $3 \times 3 \mu\text{m}^2$  sized MFM images as well as their dissipation images are shown in Fig. 4.3.

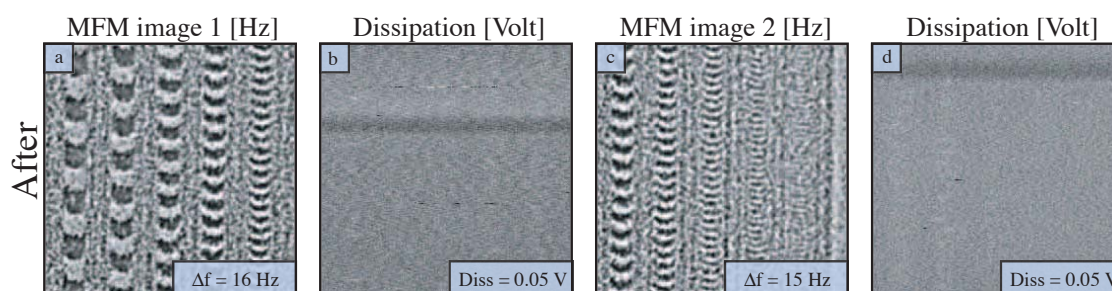


Figure 4.3: Control images ( $3 \times 3 \mu\text{m}^2$ ) taken with Tip3, after the oxidation process: as expected, there is no visible sign of a modification of the tip magnetisation.

### Calibration and Stray Field of the MFM-tips

In order to be able to do quantitative as well as qualitative analysis of future MFM measurements done with one of these three tips, they were calibrated as described in section 3.3.3. The instrument calibration function  $ICF(\mathbf{k})$  was calculated by dividing the Fourier components of the MFM image ( $\Delta f(\mathbf{k})$ ) by those of the stray field derivative  $d/dzH(\mathbf{k})$ . Note that the  $ICF$  is a two dimensional complex function. A useful representation of the  $ICFs$  of Tip1 to Tip3 is shown in Fig. 4.4. It is calculated by a circular average of the frequency components having different directions but the same wave vector  $k$  in Fourier space. The resulting spectrum is called *sensitivity spectrum* and permits the comparison of the sensitivity of the tip for different wave vectors or wavelength contained in the magnetisation pattern of the sample. Calibration errors caused by topography artefacts and inaccuracies in the magnetisation pattern determination can be reduced by averaging  $ICFs$  obtained from different MFM measurements. Note that the  $ICF$  of Tip1 and Tip3 result from an average over several  $ICFs$  obtained from different MFM images. Also note that the values of the  $ICFs$  above a spatial wavelength of 1000 nm do not have a physical meaning due to the lack of these frequencies in the original MFM images.

Another interesting characteristic in order to compare magnetic tips is their stray field

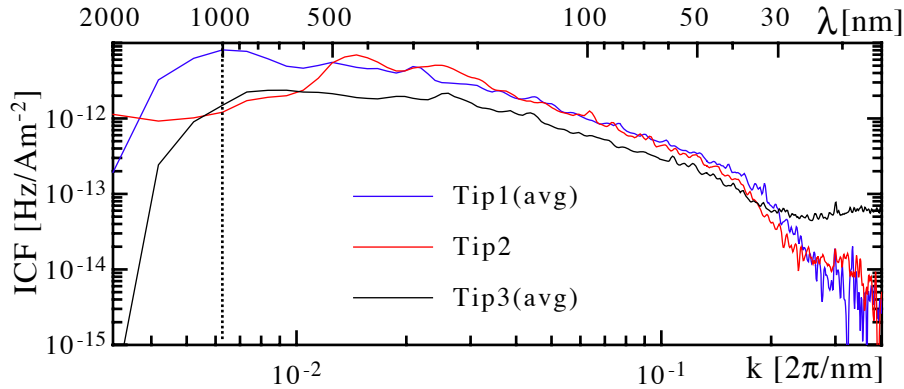


Figure 4.4: Sensitivity spectrum of the MFM tips used in this thesis calculated from the  $ICF$ : the values above 1000 nm do not have a physical meaning due to the lack of these frequencies in the MFM images.

distribution. It can be calculated from the Fourier transform of the tip-equivalent surface charge pattern, denoted as  $\sigma_{tip}(\mathbf{k})$  (see Eq. 3.26). The surface charges are located in a plane at the apex of the tip, parallel to the sample.  $\sigma_{tip}(\mathbf{k})$  itself can easily be calculated from the corresponding  $ICF$  if the canting angle and the mechanical properties (free resonance frequency  $f_0$ , spring constant  $c_L$ ) of the cantilever are known. Figure 4.5 (a) shows the calculated stray field distribution of Tip1 in a plane parallel to the sample touching the tip apex. Panel (b) shows a cross section through the stray field distribution (in x-direction) of all used tips. The stray fields of Tip1 and 2 are very similar, they both have a maximum field at the tip apex of about 10 mT. The stray field of Tip3 is a bit weaker, it measures about 7 mT. All fields are characterised by a sharp decrease from their maximum value, an indication for a high magnetic resolution.

## 4.2 Characterisation of the Magnetic Coating

The experiments described in the previous section clearly show that the tip magnetisation became more stable after the oxidation of the initial cobalt layer. This proves that the formation of an antiferromagnetic CoO layer on top of a cobalt layer has increased the coercivity of the initial cobalt layer. However, it would be desirable to get a more quantitative result. A way to quantify the results would be to measure the hysteresis loop of a coated tip before and after the formation of an oxide layer. However, the VSM described in section 3.5 is not sensitive enough to measure the magnetic moment deposited on a MFM tip. In order to get enough magnetic material for a hysteresis loop measurement, the tip coatings were 'imitated' on a simple flat silicon substrate. Two pieces of silicon were coated with a cobalt layer, one was directly coated with a protection layer against oxidation the second was oxidised then capped with a protection layer. During the evaporation on the silicon plates, the distance from the electron beam evaporator and the evaporation angle was exactly adapted to match that used during the evaporation on the



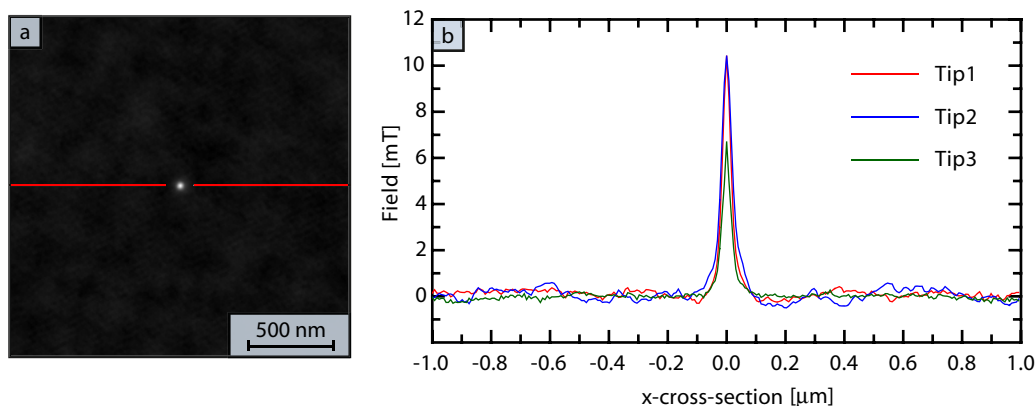


Figure 4.5: Stray field distribution of the MFM tips used in this thesis: panel (a) shows the stray field distribution of Tip1 in a plane parallel to the sample touching the tip apex. Panel (b) shows the cross section, indicated in (a), through the stray field distribution of Tip1, 2 and 3.

tip. Evaporation rate, pressure and temperatures were also chosen equal to the conditions used for the tip coating. The thickness of the evaporated cobalt layer was about 5 nm. The protection layer consisted of about 5 nm of Titanium. Hysteresis loop measurements of both coated silicon plates were taken at room temperature and at 8.3 K and are presented in the following section.

#### 4.2.1 Hysteresis Loop Measurements

Hysteresis loop measurements with the field applied parallel to the sample plane of both films were taken at 300 K and at 8.3 K. The corresponding hysteresis loops are shown in Fig. 4.6. At room temperature, the non-oxidised cobalt film exhibits a very 'square' hysteresis loop (black curve in (a)), which shows that the magnetising field is applied parallel to an easy direction of the magnetisation. Characteristic is a high remanence ratio (remanence divided by saturation magnetisation:  $M_{rem}/M_s$ ) close to 1. In comparison, the remanence ratio of the oxidised film (red curve in (a)) is slightly lower. This might be due to a small in plane anisotropy induced by the evaporation at a grazing angle. However, the coercive fields ( $H_{300K} \simeq 9$  mT) of the films are equal at room temperature. After field-cooling in 500 mT applied parallel to the sample plane to 8.3 K, the hysteresis loops were again measured (Fig. 4.6 (b)). The coercive field of the non-oxidised film increased from 9 to about 11 mT, whereas the one of the oxidised film increased by more than a factor of two, namely from 9 to 19 mT. The results of section 4.1.2 could be reconfirmed: MFM and VSM measurements show an increase of the coercive field of a thin Cobalt film when exchange coupled to an antiferromagnetic CoO layer. The field loops of the oxidised film did not show any EB-effect (i.e. horizontally shifted loop).

However, one should keep in mind that the demagnetising energy strongly depends on the 3-dimensional shape of the substrate. Therefore, the magnetic properties of a film evaporated on a cone shaped substrate might be quite different from the same film on top

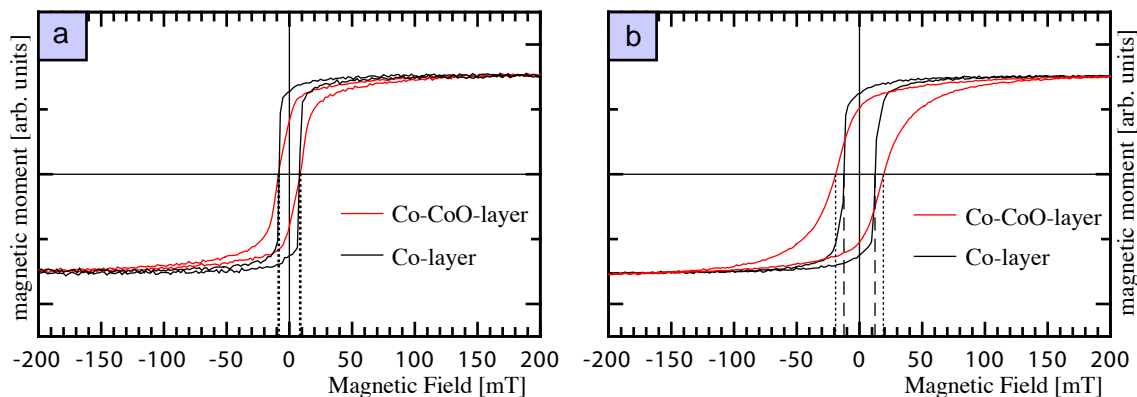


Figure 4.6: Hysteresis loop measurements of oxidised (red curves) and non-oxidised (black curves) tip coating 'imitations' on a flat silicon substrate. Loops taken at room temperature are shown in (a). Panel (b) shows the loops taken after field-cooling the samples in 500 mT to 8.3 K. No exchange bias shift was measured for the oxidised sample, however its coercive field increased by more than a factor of 2.

of a flat surface. Especially the situation at the tip apex might be strongly different from the one on a flat substrate.

### 4.3 Simulation of the Modification of the Tip Magnetisation

In section 4.1.2 the maximum energy loss per cycle during a typical tip-change event was calculated. Comparing this energy to the average energy loss per cycle, it was found that a maximum of 10 meV is provided for the modification of the magnetisation of the tip.

In order to get a feeling about the size of this energy we first approximated the maximum energy  $E_{loss/cycle}^{theo}$  that can theoretically be lost per oscillation cycle. This energy should of course be greater than 10 meV. A maximum energy loss per oscillation is realised in the following hysteresis process, assuming only magnetic forces acting on the tip: during the 'approach' of the tip (from  $z_0 + A_{osz}$  to  $z_0 - A_{osz}$ ) the magnetisation vector  $\mathbf{M}$  is supposed to be parallel to the symmetry axis of the cone, resulting in an attractive tip-sample force. The tip is considered to be at an average distance  $z_0$  from the sample surface, oscillating with an amplitude  $A_{osz} = 2.5$  nm. At the closest distance to the sample surface the tip magnetisation direction flips by  $180^\circ$  which results in a transition from an attractive to a repulsive force regime. At the farthest position (at  $z_0 + A_{osz}$ ) the magnetisation direction flips back to its original direction. The process is illustrated in Fig. 4.7 where the force acting on the magnetic tip is plotted as a function of the tip-sample distance  $z$ . The yellow area then corresponds to the maximum energy loss per oscillation and is calculated by integrating the force  $F(z)$  from  $z_0 - A_{osz}$  to  $z_0 + A_{osz}$  and multiplying by two :

$$E_{loss/cycle}^{max} = 2 \cdot \int_{z_0 - A_{osz}}^{z_0 + A_{osz}} F(z) dz. \quad (4.3)$$

Note that the force versus distance curve was calculated using a measured frequency shift versus distance curve  $\Delta f(z)$  which is related to the force gradient via

$$\frac{dF}{dz}(z) = \Delta f(z) \frac{c_L}{f_0}, \quad (4.4)$$

where  $c_L$  and  $f_0$  are the cantilever spring constant and its free resonance frequency respectively.  $F(z)$  is then found by integration of the above equation. As described above, the maximum energy loss was calculated to be  $E_{loss/cycle}^{max} = 100meV$ , ten times more than the measured energy loss per cycle. This confirms that the measured value of 10 meV does make sense as it is well below the maximum value that can be expected.

From MFM measurements we know that the tip magnetisation becomes stable if the measurement distance is increased by about 10 nm. Therefore we assume that only the 10 front most nanometers of the tip are affected by the magnetisation change. The volume of magnetic material evaporated on the front most 10 nm of the cone shaped MFM-tip  $V_{Tip}$  can be calculated using

$$V_{Tip} = h^2 d \tan \alpha. \quad (4.5)$$

where the tip shape is approximated by a perfect cone with a full opening angle  $\alpha \simeq 10^\circ$ , a tip height  $h$  of 10 nm and  $d$  the thickness of the magnetic layer. The magnetic coating is supposed to have a thickness of  $d = 4$  nm and to cover only half of the cone as it was evaporated from a direction about perpendicular to the cone surface.

In addition, the cobalt layer is supposed to be single crystalline with the corresponding

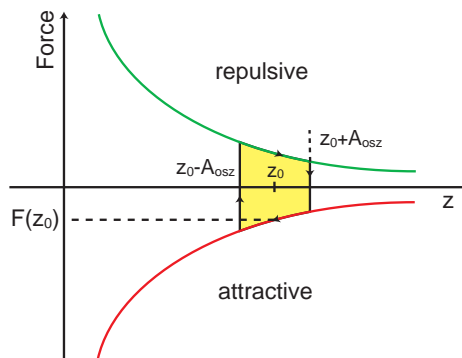


Figure 4.7: A maximum energy loss per oscillation is realised in a hysteresis process, assuming only magnetic forces acting on the tip: The force distance curve for a magnetic tip which flips its magnetisation at position  $z_0 - A_{osz}$  and  $z_0 + A_{osz}$  by  $180^\circ$ , results in attractive and repulsive forces acting on the tip. The yellow area represents the energy loss per oscillation cycle of this process.

uniaxial anisotropy lying in plane. For hexagonal crystals such as cobalt, the anisotropy energy can be described by [49]

$$\frac{1}{V_{Tip}} E_{aniso}^{uniax} = K_1 \sin^2 \theta + K_2 \sin^4 \theta, \quad (4.6)$$

where  $K_1 = 6.8 \times 10^5$  [J/m<sup>3</sup>] and  $K_2 = 1.7 \times 10^5$  [J/m<sup>3</sup>] are anisotropy constants at 8 K [50] and  $\theta$  is the angle between the magnetisation vector  $\mathbf{M}$  and the easy axis. Using Eq. 4.6 we then calculated the effective rotation angle  $\theta$  assuming  $E_{aniso}^{uniax} = 10$  meV and found that the magnetisation of the front most 10 nm of the tip can only rotated by  $\theta = 10^\circ$  with this energy.

This shows that the hysteretic modifications of the tip magnetisation, which do have a quite strong influence on the contrast formation in MFM images, are indeed due to a rather small rotation of the magnetisation in front most 10 nm of our MFM-tips.

## Chapter 5

# Experiments and Results

From a careful analysis of existing work about the exchange effect one realises that many open questions remain in this field. The subject of uncompensated spins in the AFM is often addressed in literature as it seem to play a key role in the exchange coupling between FM and AFM layers. Several experiments have proven the existence of uncompensated spins in the AFM. However, these experiments give conflicting results on their density, their orientation relative to the FM magnetisation and their role for the EB-effect.

In this chapter, “new” light is shed on the role of the uncompensated spins in the AFM by combining high resolution, quantitative MFM techniques with classical magnetometry methods applied to carefully selected samples. From a diligent design and analysis of MFM and magnetometry experiments performed on three different FM/AFM samples we conclude that pinned UCS in the AFM are responsible the EB-effect and are aligned antiparallel to the ferromagnetic spins in all our samples. Additionally, pinned UCS aligned parallel to the spins of the FM do also exist but are not responsible for the EB-effect. This chapter presents all experimental work carried out and the resulting conclusions.

### 5.1 Introduction

An overview over the most important experimental phenomena observed in exchange biased systems was given in chapter 2. In addition some theoretical models trying to elucidate the measured effects were presented. Most of them claim that uncompensated spins in the AFM are responsible for the exchange bias phenomena. However, the models differ severely in the reasons for the appearance of these uncompensated spins as well as about their locations in the AFM, their orientation and their density. Various experimental techniques are able to detect small amounts of uncompensated spins. In magnetometry experiments, pinned UCS lead to a vertical shift of the magnetic hysteresis loop, as explained in section 2.1.4. Several groups [38, 34, 51] have argued that the UCS observed via a positive vertical shift are responsible for the exchange bias effect. Ohldag et al. [16] argued that the height of such a loop corresponds to UCS that rotate with the FM spins, whereas the vertical loop shift corresponds to pinned UCS that are responsible for the exchange bias effect. Both, the rotating and the pinned UCS of the AFM were found to align parallel with the spins of the FM. Although about 50 % of a monolayer of spins is found to be uncompensated only a few percent thereof was found to be pinned. The size of the

exchange bias field could be understood in terms of a simple extension of the Meiklejohn and Bean model (see section 2.2.1): The measured exchange fields corresponded well to the density of pinned UCS.

A part of the performed experiments seem to give conflicting results: Magnetic force microscopy results obtained on a CoO/CoPt-multilayer AFM/FM system have shown an antiparallel alignment of the pinned UCS with the ferromagnetic spins [19]. However, earlier magnetometry data on a CoO/Co system [34] revealed a positive vertical shift of the hysteresis loop that was attributed to UCS that align parallel to the spins of the FM. Element specific magnetization loops measured by x-ray magnetic circular dichroism - (XMCD) on a IrMn/Co-system [16] also revealed a positive vertical loop shift, but recent XMCD photoemission electron microscopy (PEEM) experiments [18] showed an antiparallel alignment of the UCS Mn spins of the CoFeB/IrMn interface with the Co spins of the FM.

Based on these conflicting results we decided to design our samples and experiments in order to address two open questions: The first question can be summarised as '*What is the role of uncompensated spins in exchange biased systems?*' and will be addressed in section 5.3. To answer this question the existence of UCS is confirmed, the relative arrangement of the FM spins and the UCS of the AFM and the density of the latter were determined. Note that in literature, values ranging from only 1 % [13] up to about 80 % [14] of a fully uncompensated monolayer of spins were reported.

The second open question addresses the spacial distribution of UCS on the scale of single grains (section 5.4). So far, the spacial distribution of the UCS could be imaged on scale of magnetic domains which are mostly in the the micrometer range. A resolution on single grain scale (nanometer scale) has not yet been achieved so yet. According to the model of Takano et al. (see section 2.2.2), the density of UCS at the FM/AFM interface is expected to be not homogeneous on the scale of single grains. The observation of the alignment of the pinned uncompensated spins of the AFM by the FM spins is not sufficient to prove a true correlation between number of UCS and the strength of the EB-effect. A true correlation between the UCS-density and the strength of the EB-effect can be confirmed if the regions of high UCS-density can be correlated to a local "strengthening" of the FM domain. The local "strengthening" of the FM domains (i.e. the local strength of the exchange bias field) can be deduced from studies of the FM domains versus externally applied field.

In order to carry out the tasks outlined above, carefully designed samples were prepared by sputter deposition techniques. The criteria for the sample design are discussed in the following section. For the experimental analysis of the samples two methods were used: The macroscopic magnetic properties were analysed by VSM and for the investigations on the nanometer scale, Magnetic Force Microscopy techniques were used. The crystalline structure of the samples was analysed by transition electron microscopy (TEM).

## 5.2 Model Systems and Sample Characterisation

In order to confirm the existence of pinned UCS, a small pinned magnetic moment must be detected in a large background. This measurement may be facilitated by means of a sample that contains several FM/AFM interfaces but keeps the total volume of the FM

and AFM small. Hence, FM/AFM multilayer samples were fabricated. As an FM a CoPt-multilayer with a strong perpendicular magnetic anisotropy was chosen. This simplifies the analysis of the measured MFM data.

For a first multilayer sample CoO was chosen as an antiferromagnet. The decision was reasoned by three points: (1) the interfacial anisotropy energy (Eq. 2.2) of FM/AFM systems with CoO as an AFM exceeds the one of all other FM/AFM systems containing other antiferromagnetic materials [12]. (2) The pinned UCS at the CoO/CoPt interfaces are difficult to investigate with techniques which are sensitive to chemical species. The atoms carrying the magnetic moments in FM and the AFM are identical, therefore they can hardly be separated. (3) Earlier MFM measurements performed on a CoO/CoPt-multilayer sample [19] proved that the UCS in the AFM can be imaged using MFM techniques and found an antiparallel alignment of the UCS with the FM spins. This finding could be further confirmed by the observation of a negative vertical shift of the hysteresis loop.

For further confirmation, all the measurements will be repeated on a FM/AFM-multilayer system with a different AFM layer. A metallic antiferromagnet, IrMn, was chosen for the second multilayer sample. Due to its electrical conductivity and inertness to oxygen it is often used in spin valves and is therefore of importance in practical devices such as magnetic field sensors [52]. Soft x-ray resonant magnetic scattering experiments performed on a NiFe/Cu/Co/IrMn spin valve structure [17] revealed a small magnetic moment on the antiferromagnetic IrMn-layer. It could be shown that this moment lies antiparallel to the Co moment.

To be able to image the spacial distribution of the UCS in a AFM on single grain scale, an FM/AFM-singlelayer sample was produced. Here, the term “singlelayer” denotes a sample containing only one AFM layer. Still, the antiferromagnetic layer can be “sandwiched” between two ferromagnetic layers. As ferromagnetic and antiferromagnetic materials we used a CoPt-multilayer and CoO respectively, which already gave promising results in the multilayer sample.

### 5.2.1 Macroscopic Sample Structure

In this section the macroscopic sample structure as well as the sample preparation processes are described. Furthermore the crystalline and magnetic structures of the FM and AFM layers are illustrated.

#### Multilayer Samples

All samples presented in this section were prepared at *Hitachi Global Storage Technologies* (HGST, San Jose, USA) by DC magnetron sputtering on a Si wafer covered with its native oxide layer ( $\text{SiO}_2$ ) and are similar to those described in [53]. The deposition was performed at room temperature under an argon pressure of  $2.3 \times 10^{-3}$  mbar.

The exact composition of the CoO/CoPt-multilayer sample is  $\text{Si:Pt}(20\text{nm})\text{CoO}(10\text{\AA})\text{-}\{[\text{Co}(4\text{\AA})/\text{Pt}(7\text{\AA})]_4 \text{Co}(6\text{\AA})\text{CoO}(10\text{\AA})\}_{10}$ . The CoO layers were formed by natural oxidation of  $16 \text{\AA}$  thick Co layers left in air for 10 minutes. Thereof a bilayer system of  $10 \text{\AA}$  CoO and  $6 \text{\AA}$  Co resulted. Figure 5.1 (a) and (b) presents a schematic of the complete sample structure and of the structure of the FM layers, respectively. The crystalline structure of CoO is shown in Fig. 5.1 (c). It exhibits a so-called rocksalt structure (NaCl

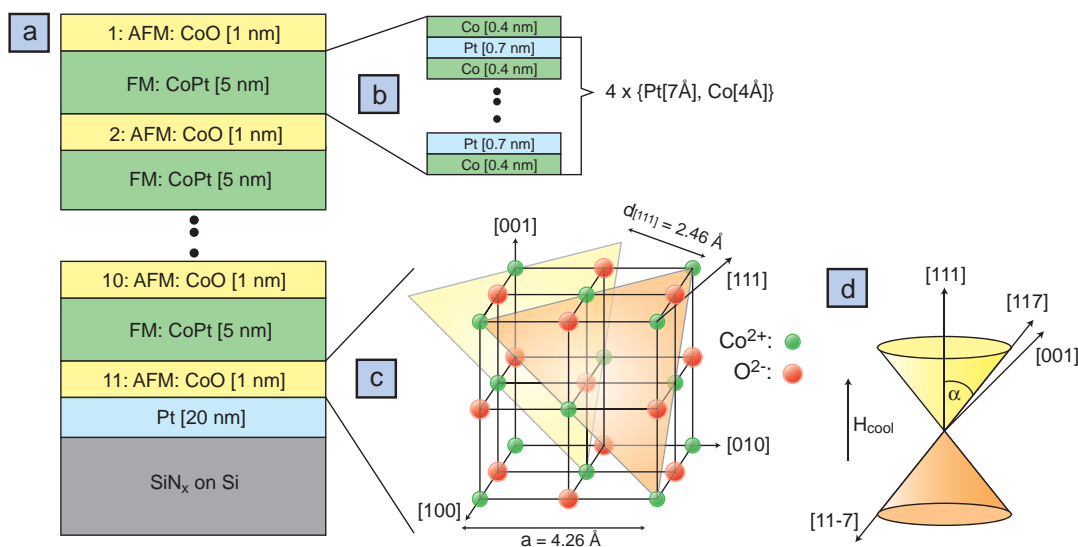


Figure 5.1: The CoO/CoPt-multilayer sample: Schematic drawing of the CoO/CoPt-multilayer sample structure (a). It consists of 11 antiferromagnetic CoO layers interspaced with 10 ferromagnetic Co/Pt layers (b). Panel (c) shows the primitive cell (rocksalt structure) of CoO. The magnetic moments of the Co ions are parallelly aligned in the  $[111]$ -planes. Neighbouring  $[111]$ -planes (yellow and orange planes) couple antiferromagnetically by superexchange coupling over the O-atom. The parallelly aligned spins point into the  $[117]$ -direction. If the cooling field  $H_{cool}$  is parallel to  $[111]$ -direction, the CoO spins freeze into their easy axis which is closest to  $H_{cool}$ . Thus the CoO spins of independent domains will be distributed on a cone defined by the  $[111]$ - and  $[117]$ -directions ( $\alpha = 43.3^\circ$ ) (d).

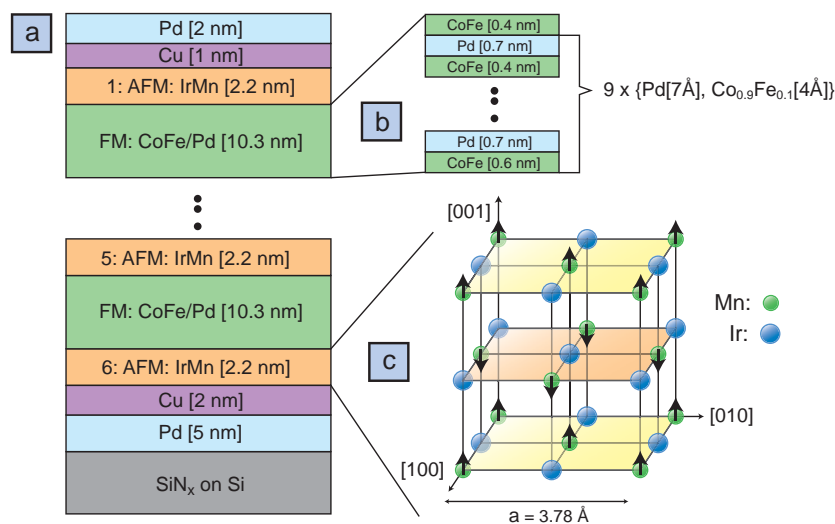


Figure 5.2: The IrMn/ $\text{Co}_{0.9}\text{Fe}_{0.1}\text{Pt}$ -multilayer sample: Schematic of the IrMn/ $\text{Co}_{0.9}\text{Fe}_{0.1}\text{Pt}$ -multilayer sample structure (a). It consists of 6 antiferromagnetic IrMn layers interspaced with 5 ferromagnetic  $\text{Co}_{0.9}\text{Fe}_{0.1}/\text{Pd}$  layers (b). Panel (c) shows the primitive cell (rocksalt structure) of IrMn. The spins point into  $[001]$ -direction and are ferromagnetically aligned in the  $[001]$ -planes. Neighbouring  $[001]$ -planes (yellow and orange planes) are antiferromagnetically stacked.



structure) which is formed from two fcc sublattices of  $\text{Co}^{2+}$  and  $\text{O}^{2-}$  ions. The lattice constant is  $a = 4.26 \text{ \AA}$ . The spins in the [111]-planes are ferromagnetically aligned and point into the [117]-direction [54, 55, 56]. The spins of successive [111]-planes (yellow and orange planes in Fig 5.1 (c)) are antiferromagnetically coupled by superexchange interaction via the oxygen ions (see section 5.3.2). Upon cooling through  $T_{Neel}$  in a magnetic field applied perpendicular to the sample surface, the spins freeze into the anisotropy axis closest to the applied field. If a perfect [111]-texture of the CoO grains is assumed (i.e. the [111]-direction is perpendicular to the surface), the spins of the various antiferromagnetic domains will be distributed on a cone surface with a half cone angle of  $\alpha = 43.3^\circ$  (see Fig. 5.1 (d)). However, as determined from XRD and confirmed by TEM, the CoO/CoPt-multilayer is [111]-textured with an off-axis distribution (mosaicity) of about  $10^\circ$  from the [111]-direction.

The IrMn/Co<sub>0.9</sub>Fe<sub>0.1</sub>Pt-multilayer has a similar structure. Its exact composition is Si:Pt (5nm) Cu(2nm)IrMn(2.2nm){[Co<sub>0.9</sub>Fe<sub>0.1</sub>(6Å)/Pd(7Å)]<sub>9</sub> Co<sub>0.9</sub>Fe<sub>0.1</sub>(4Å) IrMn(2.2nm)}<sub>5</sub> Cu (1nm) Pd(2nm), and is shown in Fig. 5.2 (a) and (b). The IrMn was sputtered from an Ir<sub>0.2</sub>Mn<sub>0.8</sub>-alloy target. The crystalline structure of IrMn is equal to the one of CoO (rock-salt structure). The magnetic structure could still not be determined unambiguously: A complex four-lattice magnetic structure gives the identical magnetic structure factor as the simpler two-sublattice magnetic structure shown in Fig. 5.2 (c). However, a two-sublattice magnetic structure seems to be slightly favored by some neutron diffraction experiments [57, 58]. Therefore it will serve as a model for all future analysis in this thesis: The ferromagnetic [001]-planes (yellow and orange) are antiferromagnetically stacked. The spin axis is parallel to the [001]-direction within  $4^\circ$ . No further measurements were done to determine the texture of this multilayer. Other authors [59] found that their IrMn films grown on CoFe are [111]-textured like the CoO/CoPt-multilayer film.

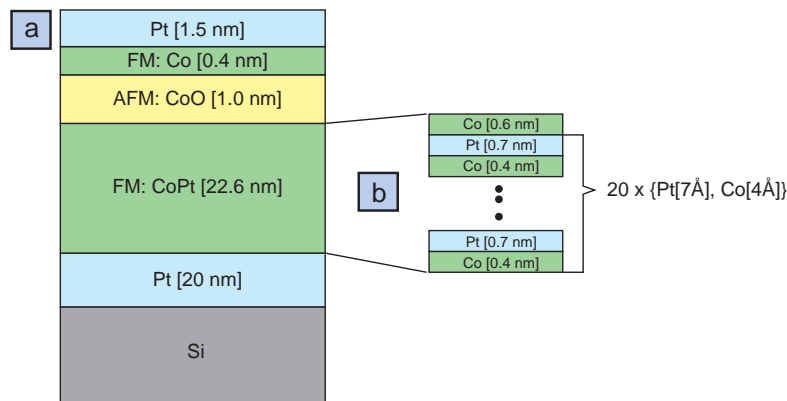


Figure 5.3: The CoO/CoPt-singlelayer sample: Schematic of the CoO/CoPt-singlelayer sample structure (a). It consists of only one antiferromagnetic CoO layer which is sandwiched between two ferromagnetic CoPt-multilayers (b). The microscopic sample structure is supposed to be equal to the one of the CoO/CoPt-multilayer sample shown in Fig. 5.1

### Single-AFM-layer Sample

The CoO/CoPt-singlayer sample was grown under the same conditions as the multilayer samples described above. Its exact structure is Si:Pt(20nm)[Co(4Å)/Pt(7Å)]<sub>20</sub> Co(6Å)/CoO(10Å)/Co(4Å)/Pt(1.5 nm), where the CoO and the CoPt-multilayer are supposed to have the same properties and structure as the ones in the CoO/CoPt-multilayer. A schematic of the sample structure is shown in Fig. 5.3.

### 5.2.2 Microscopic Sample Structure by TEM

The microscopic structure and crystallinity of the sample was further investigated using a high resolution transmission electron microscope (Philips CM 300) at the EPF in Lausanne. The images were taken by Dr. M. Parlinska-Wojtan. The samples were prepared using the so-called tripod wedge sample polishing method: two small pieces of about 1 x 3 mm<sup>2</sup> were cut, glued face to face and attached to the underside of a tripod holder. Using a wet grinding technique, they were polished into a wedge with an opening angle of less than 5°. After the treatment, the thin end of the wedge had a final thickness of less than 150 nm, determined from light microscope inference fringe measurements on the Si-substrate. The samples were then introduced into an Ar<sup>+</sup>-ion milling machine and further thinned to about 50-80 nm.

Figure 5.4 (a) shows an overview of the CoO/CoPt-multilayer sample imaged by TEM in bright field mode. The antiferromagnetic CoO-layer visible in bright contrast can be well separated from the CoPt multilayer (dark contrast). The Co and Pt layers could not be resolved individually due to their metallic nature. In the overview image, single grains with diameters of 20 to 40 nm are visible and protrude through the whole multilayer (cf. red contour line). This indicates a good epitaxy of the multilayer system. Fig. 5.4 (b) shows a high resolution zoom on CoO embedded between two CoPt layers. The atomic row contrast visible in the image indicates, that the CoO grows crystalline on the CoPt-multilayer and vice versa. No line dislocations or stacking faults can be seen even at the interface between the CoO and the CoPt. In addition, the interface roughness at the FM/AFM interface is very small, on the order of a few atomic steps per grain. These terraces are playing a crucial role in the explanation of the exchange bias effect on a nanometer and sub-nanometer lengthscale (see section 5.4.2). Two types of grain boundaries could be identified: large and small angle grain boundaries. The first and most common type comprise large angle grain boundaries. As can be seen from Figure 5.4 (c), the angle between the lattices in adjacent grains is so large that it is not possible to resolve both grains with atomic contrast. It is clearly visible, that the CoO layer is disrupted between the two grains. The second type of grain boundaries is of small angle nature. Figure 5.4 (d) shows an example of this type. It is clearly visible in the image, that the growth of the CoO layer from the left to the right grain is not disrupted. The strain occurring due to the small tilt angle between the grains is released by incorporation of several line dislocations at the boundary.

### 5.2.3 Magnetometry Experiments

The macroscopic magnetic properties of the samples are determined in a series of VSM measurements performed at temperatures ranging from 300 K to 8.3 K. For all hysteresis

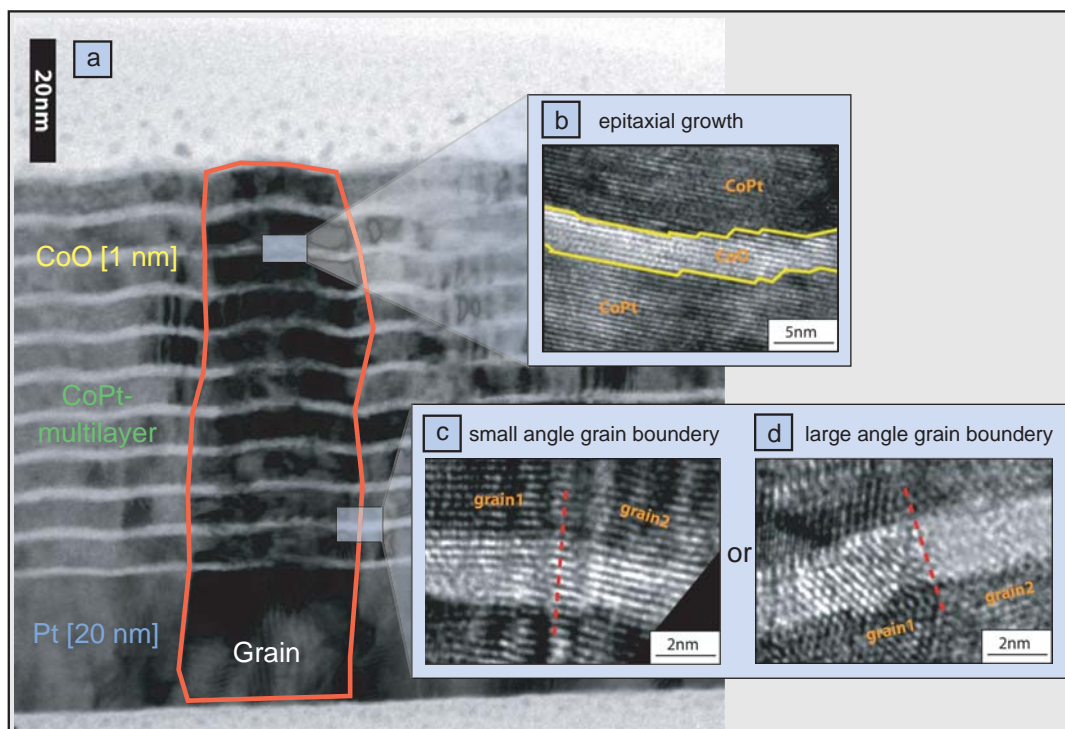


Figure 5.4: TEM image of a CoO/CoPt-multilayer sample: (a) shows an overview in bright field mode. The CoO layers (bright contrast) can well be distinguished from the CoPt-multilayers (dark contrast). Grains protruding the whole layer thickness can be identified (red outline). The growth of CoO on CoPt (and vice versa) is epitaxial (b) with only atomic scale roughness. Small- and large angle grain boundaries depicted in (c) and (d) can be identified in the system, the first type being the most common one.

loops shown in this section, the magnetic field is applied along the easy axis, i.e. perpendicular to the sample plane. For better comparison, all hysteresis loops are normalised.

For the CoO/CoPt-multilayer sample, hysteresis loops are measured at room temperature (300 K), at low temperature (8.3 K) after zero-field and after cooling in a 2 T field (see Fig. 5.5 (a), red, green and blue loop, respectively). The room temperature loop (red) is characterised by a low coercivity and a low remanent magnetisation. The zero-field cooled hysteresis loop shows a strong increase of the coercivity but no horizontal shift. After field-cooling in 2 T to 8.3 K, the hysteresis loop (blue) is horizontally shifted by  $H_{EB} = -147$  mT, whereas the coercive field increased from about 5 mT to  $H_C = 395$  mT. Additionally, several hysteresis loops were measured at temperatures ranging from 300 K to 8.3 K after cooling in a 2 T field. From these loops the exchange field  $H_{EB}$  and the coercive field  $H_C$  were extracted and plotted versus temperature in Figure 5.5 (b), red and black curves, respectively. As expected do both quantities strongly depend on temperature. The disappearance of the exchange field at a temperature of about 200 K identifies the blocking temperature  $T_B$  of the CoO in this sample. To compare, the Néel temperature of bulk CoO is 290 K [12]. Finally, the saturation magnetisation of the

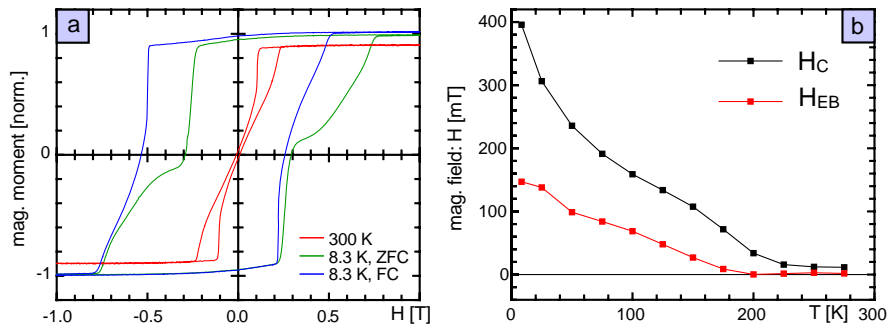


Figure 5.5: Hysteresis loops of the CoO/CoPt-multilayer sample: panel (a) shows the hysteresis loop taken at 300 K (red), the hysteresis loop of the zero-field cooled sample at 8.3 K (green) and the horizontally shifted loop (blue) after field cooling in 2 T to 8.3 K. The exchange field  $H_{EB}$  and coercivity  $H_C$  as a function of temperature are shown in (b), for the cooling field of 2 T.

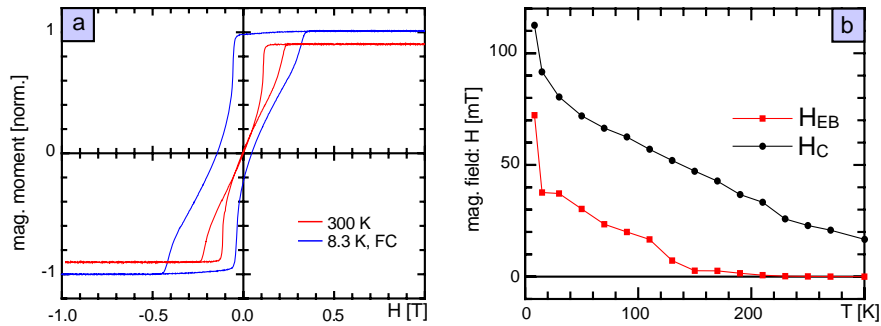


Figure 5.6: Hysteresis loops of the IrMn/CoPd-multilayer sample: panel (a) shows the hysteresis loop taken at 300 K (red) and the horizontally shifted loop (blue) after field cooling in 1.5 T to 8.3 K. The exchange field  $H_{EB}$  and coercivity  $H_C$  as a function of temperature are shown in (b), for a cooling field of 1.5 T.

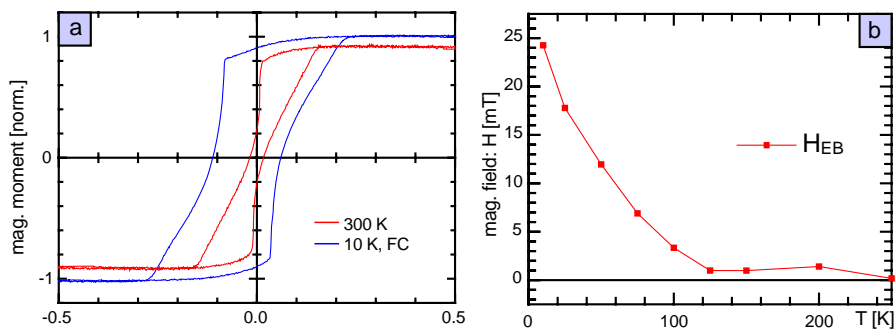


Figure 5.7: Hysteresis loops of the CoO/CoPt-multilayer sample: panel (a) shows the hysteresis loop taken at 300 K (red) and the horizontally shifted loop (blue) after field cooling in 500 mT to 10 K. The exchange field  $H_{EB}$  as a function of temperature are shown in (b), for a cooling field of 500 mT.

sample at 8.3 K was determined to be  $M_{CoO-multi}^{8.3K} = 517$  kA/m.

Figure 5.6 (a) shows the hysteresis loop measurements of the IrMn/CoPd-multilayer sample. The room temperature loop (red) strongly resembles the one of the CoO/CoPt-multilayer sample shown in Fig. 5.5 (a). The low temperature loop (blue) is taken after field-cooling in 1.5 T to 8.3 K and exhibits an exchange field  $H_{EB} = -72$  mT and a coercivity of 112 mT. Again, a series of M(H) loops is acquired after cooling to various temperatures in a field of 1.5 T. From these loops, the values of  $H_{EB}$  and  $H_C$  are determined and plotted as a function of temperature in Fig. 5.6 (b). The blocking temperature of the antiferromagnetic IrMn-layers in this sample was found to lie around 180 K. This is far below the Néel temperature of bulk IrMn which is well above room temperature, at about 690 K [12]. The magnetisation of the FM layers at 8.3 K was determined to be  $M_{IrMn-multi}^{8.3K} = 630$  kA/m.

Finally, the hysteresis loops of the CoO/CoPt-singlelayer sample are presented in Fig. 5.7 (a) and the dependence of  $H_{EB}$  on temperature in (b). The low temperature loop was measured after field-cooling in 500 mT to 10 K. It exhibits a horizontal loop shift of  $H_{EB} = -24$  mT and an increase of the coercivity from 20 mT to 80 mT. The blocking temperature of the CoO layer is identical to the one measured for the multilayer sample and thus is about 200 K. The magnetisation of the FM layers in this sample was determined to be  $M_{CoO-single}^{8.3K} = 622$  kA/m at 8.3 K.

In order to be able to compare the strength of the exchange coupling of the samples described above, the interface anisotropy energy per unit area is calculated from Eq. 2.2. For the CoO/CoPt-multi- and singlelayer sample we find  $\Delta E_{CoO-multi} = 3.8 \times 10^{-4}$  J/m<sup>2</sup> and  $\Delta E_{CoO-single} = 3.4 \times 10^{-4}$  J/m<sup>2</sup>, respectively. These values correspond to the values reported in literature for similar systems [12]. For the IrMn/CoPt-multilayer sample we calculate  $\Delta E_{IrMn-multi} = 4.7 \times 10^{-4}$  J/m<sup>2</sup> which is a rather high value for IrMn coupled to various FMs. However, no values were found for IrMn coupled to CoPt.

With respect to section 2.1.4, the vertical shift of the loops taken after field cooling is determined. Small, positive vertical shifts of the hysteresis loop were found for both multilayer samples. The shifts of the hysteresis loops thus arise from pinned magnetic moments aligned parallel to the cooling field. For the CoO/CoPt-singlelayer sample, no vertical shift could be detected with the sensitivity of about  $1 \times 10^{-6}$  emu/T of our VSM. Thereof, one can calculate the pinned uncompensated moments per FM/AFM interface using the vertical shift and the sample area. The magnetic moment  $m_{vs}$  of the CoO/CoPt-multilayer sample (sample area =  $7.04 \times 10^{-6}$  m<sup>2</sup>) and the IrMn/CoPd-multilayer sample (sample area =  $6.17 \times 10^{-6}$  m<sup>2</sup>) is determined to be  $3.2 \pm 0.5 \times 10^{-9}$  Am<sup>2</sup> and  $2.0 \pm 0.5 \times 10^{-9}$  Am<sup>2</sup>, respectively. The total pinned magnetic moment is then divided by the total number

Sample	$H_{EB}$ [mT]	$\Delta E$ [J/m <sup>2</sup> ]	$T_B$ [K]	$T_N$ [K]	$M_{LT}$ [kA/m]	UCS/int. [%]
CoO-multi	-147	$3.8 \times 10^{-4}$	200	290	517	+5 %
IrMn-multi	-72	$4.7 \times 10^{-4}$	180	690	630	+9 %
CoO-single	-24	$3.4 \times 10^{-4}$	200	290	622	-

Table 5.1: Magnetic properties of the samples studied in this thesis, determined from VSM experiments.

of FM/AFM interfaces and compared to the magnetic moment contained in a monolayer of spins in CoO or IrMn. For the CoO/CoPt-multilayer and the IrMn/CoPd-multilayer sample about  $+5\pm 0.8\%$  and  $+9\pm 1.8\%$  of a fully uncompensated monolayer were measured, respectively.

The magnetic properties of the samples determined from VSM experiments are summarised in Table 5.1.

### 5.3 The Role of Uncompensated Spins

The existence of uncompensated spins in antiferromagnetic layers was proven by various methods (see section 2.1.4). Mostly, the measurement of a vertical hysteresis loop shift or element specific methods such as XMCD were used to determine the uncompensated spins in the AFM. Most often, a parallel alignment of the uncompensated spins in the AFM and the spins of the FM was found. Indeed, our own VSM measurements also revealed a positive vertical shift of the hysteresis loop. However, our earlier MFM measurements performed on the CoO/CoPt-multilayer sample [19, 60] clearly showed an antiparallel alignment of the uncompensated spins in the AFM relative to the FM.

All MFM data described in [19] were acquired with the LTSFM system described in section 3.1.1 and [42]. Prior to the MFM experiments, the FM layers of the CoO/CoPt-multilayer sample were demagnetized at room temperature which resulted in a stripe domain state of the FM. The MFM images taken after zero-field cooling to 8 K thus showed a regular stripe domain pattern (FM-contrast) and is shown in Fig. 5.8 (a). Regions of white or black contrast denote areas with the magnetisation antiparallel or parallel to that of the tip, respectively. The size of the MFM image shown in Fig. 5.8 (a) is  $5 \times 5 \mu\text{m}^2$  and the frequency shift range is 29.2 Hz. The images were taken at an average tip-sample distance of 30 nm to avoid any contribution of the sample topography to the magnetically induced frequency shift signal.

As confirmed by XMCD PEEM experiments [15, 16, 18] the domains of the FM generate a local EB-effect. Figure 5.8 (b) shows MFM data acquired at 8 K in +800 mT field, applied parallel to the magnetisation of the MFM tip, where the ferromagnetic layers were completely saturated. Surprisingly, stripe domains were still visible although at +800 mT the FM layers were completely saturated. However, the image was more granular and the measured frequency shift contrast was about 30 times smaller than that of image 5.8 (a). The saturated FM layers do not contribute to the contrast observed in +800 mT as their magnetization is homogeneous. Therefore, the weak contrast shown in Fig. 5.8 (b) has to be attributed to stray fields emanating from pinned UCS of the AFM (AFM-contrast). Note, that the AFM-contrast remains visible even in magnetic fields of up to 7 T (not shown). Note that the freely rotating UCS of the AFM remain invisible for the MFM: they align parallel to the external field and form a homogeneous distribution of spins inside the AFM that does not contribute to the measured stray field.

Magnified sample areas of Fig. 5.8 (a) and (b) are shown in (c) and (d), respectively. A contrast inverted image of the FM-contrast (c) is shown in (e). A comparison of the magnified MFM image shown in Fig. 5.8 (d) with the contrast inverted image (e) clearly reveals an antiferromagnetic coupling between pinned UCS of the AFM and the adjacent spins of the FM.

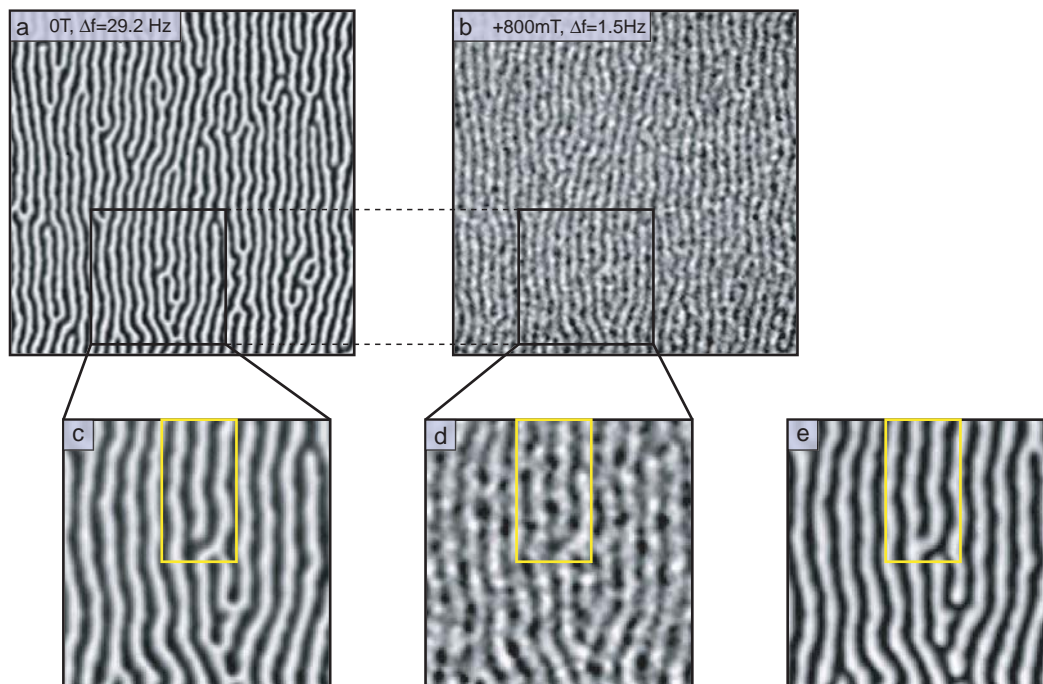


Figure 5.8: MFM images of the CoO/CoPt-multilayer sample: Panel (a) shows a  $5 \times 5 \mu\text{m}^2$  sized image taken directly after zero-field cooling the sample in a demagnetised stripe domain state. Panel (b) shows an image of exactly the same sample area in field of +800 mT (applied parallel to the tip magnetisation) which completely saturates the ferromagnetic layers. The weak and grainy stripe contrast persists even in fields up to 7 T (not shown). Magnified regions of the images (a) and (b) are shown in (c) and (d), respectively. A contrast inverted image of the FM-contrast (c) is shown in (e). A comparison between (d) and the contrast inverted image (e) clearly reveals an antiferromagnetic coupling between the USC of the AFM and the adjacent spins of the FM.

In order to calculate the magnetic charge density arising from the UCS at the AFM/FM-interfaces, Kappenberger et al. performed a quantitative analysis of the AFM-contrast. Therefore the MFM tip was first calibrated as explained in section 3.3.3. Then a discrimination procedure was used to determine a black and white magnetization pattern from the AFM-contrast shown in Fig. 5.8 (b). The magnetic charge density attributed to the black and white domains of the magnetisation pattern was then adjusted to obtain the best agreement between the measured and the simulated images. The best agreement was obtained for a surface charge density of 118 kAm which corresponds to about 7 % of the surface charge density of a fully uncompensated monolayer of spins in a [111]-plane of CoO. This result [19] agreed well with the estimates of 0.04 monolayer of UCS in the Co/NiO-system found by Ohldag et al. [16] and the 0.01 monolayer observed by Takano et al. [13, 38] in a  $\text{Ni}_{81}\text{Fe}_{19}/\text{CoO}$  system.

Thus a contradiction between the MFM data measured earlier by Kappenberger et al. and the recently performed magnetometry experiments described in section 5.2.3 becomes

apparent: The former clearly revealed an antiparallel alignment of the pinned UCS of the AFM with the adjacent spins of the FM layer whereas the latter magnetometry data indicate a parallel alignment. In this thesis, additional MFM and magnetometry data are measured in order to understand the contradictory results obtained so far.

### 5.3.1 MFM on Multilayer Samples

To further confirm the earlier results obtained on the CoO/CoPt-multilayer sample, we decided to first redo MFM measurements with higher spatial resolution but on the same sample. After cooling in an as-grown domain state, the average domain size of the as-grown FM domains is about twice as large as the average width of the stripe domains obtained after demagnetising the FM layers at room temperature. Images of smaller sample areas and taken at closer tip-sample distances increase the resolution and give therefore more information on the local distribution of the UCS. However, imaging at closer tip-sample distances has on main disadvantage: Van der Waals forces start to increase such that topography artefacts become visible. As the magnetic contrast arising from UCS in the AFM is very weak, the contribution of the topographic signal to the measured frequency shift signal even may become comparable to the contribution of the magnetic signal. It exists a method, originally developed by Foss et al. [43], that permits the separation of magnetic and topographic contributions in MFM measurements. The method consists in taking two MFM images of the same sample area and at the same tip-sample distance but with opposite tip magnetisation direction. For ferromagnetic samples this is usually a difficult task, as the tip magnetisation directions has to be flipped by 180 degrees without modifying the magnetic sample state. In practice this often means that the tip has to be moved from the sample, by removing the tip-holder for the time of the tip magnetisation reversal, and then putting it back to the exactly the same sample area. To retrieve the original sample area is not completely impossible but surely very time consuming. By adding the images taken with inverted tip magnetisation, the magnetic contributions are cancelled out. As the topographic contributions do not change sign by inverting the tip magnetisation direction they will add up to twice the topographic signal. On the other hand, the difference of the images will consist of twice the contribution of the magnetic signal as the topography contributions are subtracted. This method was successfully applied in [61].

#### Separation of Magnetic and Topographic Contributions to MFM Images

As mentioned above, it is technically rather difficult to perform two MFM measurements with opposite tip magnetisation but under otherwise equal conditions. However, for the special case of imaging the UCS of an AFM the procedure can be simplified. As the magnetic moment of the UCS is pinned it will not be affected by a externally applied field inverting the magnetisation direction of the MFM tip. Explained in more detail, when the FM/AFM sample is zero-field cooled, the domain state of the UCS of the AFM will be determined by the domain state of the FM. At temperatures below  $T_N$ , the domain state of the FM can still be modified by an magnetic field whereas the domain state of the AFM remains unaffected. Only extremely strong magnetic fields or repeated field cycling (training) would be able to change the uncompensated spins of the AFM.



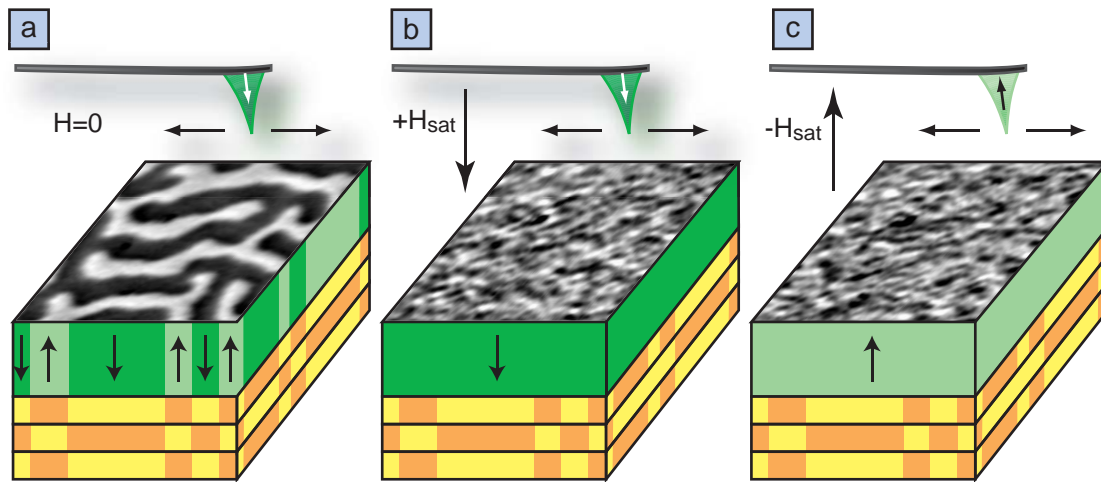


Figure 5.9: Separation of topographic and magnetic contributions to MFM images of the uncompensated AFM magnetisation: After zero-field cooling the sample below  $T_N$ , the ferromagnetic domains (green) are 'imprinted' in the AFM (yellow-orange) (a). The ferromagnetic layer is saturated in a field  $+H_{sat}$  applied parallel to the tip magnetisation (b). An MFM image of this sample state then only contains contributions of the uncompensated magnetization in the AFM and topography due to van der Waals forces. As the state of the AFM magnetisation does not change in an applied field (c), the tip magnetization can be reversed without changing the magnetic sample state. By adding and subtracting the MFM images obtained in (b) and (c), pure topographic and magnetic signal can be obtained, respectively.

Figure 5.9 (a) shows the domain state of the ferromagnetic (green) and antiferromagnetic layer (yellow-orange) after zero-field cooling. When a positive field  $+H_{sat}$  saturating the FM layers is applied parallel to the initial tip magnetisation direction, the FM does not contribute to the frequency shift signal any more (Fig. 5.9 (b)). The measured MFM signal then only arises from the magnetic contribution of the UCS in the AFM and the sample topography via van der Waals forces. Finally, the magnetization of the tip is reversed by a negative field  $-H_{sat}$  driving the FM layer into negative saturation (Fig. 5.9 (c)). As the uncompensated magnetization of the AFM remains unaffected by the field reversal, a separation of magnetism and topography becomes possible using the procedure described above. This technique was applied to most of the high resolution images presented in this thesis and was found to be an extremely reliable.

### High Resolution MFM Images of the CoO/CoPt-Multilayer Sample

After zero-field cooling the CoO/CoPt-multilayer sample in its as-grown magnetisation state, maze like domains are observed (Fig. 5.10 (a)). From the measured  $2 \times 2 \mu\text{m}^2$  sized image, a  $1 \times 1 \mu\text{m}^2$  sized subimage is further investigated. Panel (b) shows the MFM data measured in a field of +400 mT applied parallel to the initial direction of the

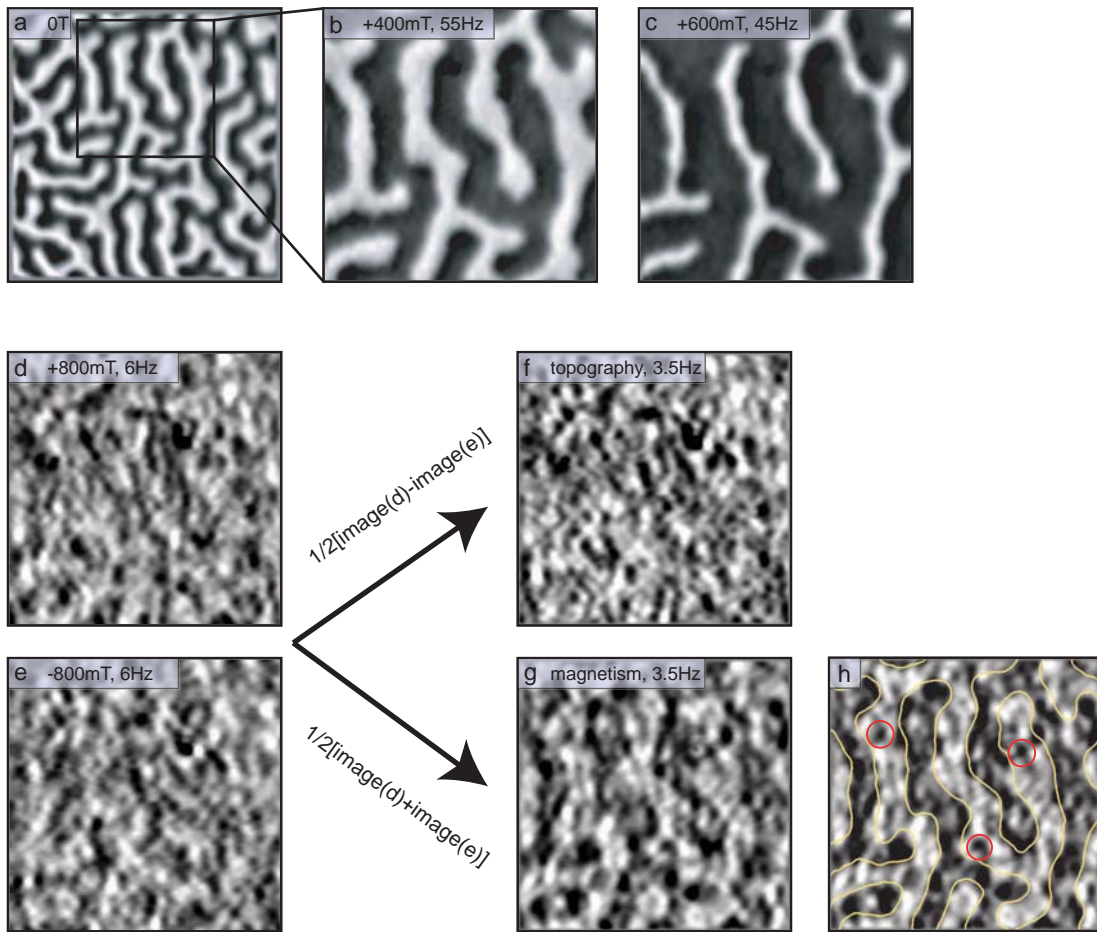


Figure 5.10: High resolution MFM images of the CoO/CoPt-multilayer sample: A  $2 \times 2 \mu\text{m}^2$  sized overview image taken after zero-field cooling the sample with the FM layers in their as-grown domain state is shown in (a). Panel (b) shows a  $1 \times 1 \mu\text{m}^2$  sized subimage, indicated by a black square in (a). The image (b) was taken in a field of +400 mT applied parallel to the tip magnetization at a tip-sample distance  $z = 10$  nm. The same area was imaged again in a field of +600 mT and at  $z = 13$  nm in (c). Finally, MFM images were acquired in +800 mT (d) and in -800 mT applied field (e), at the same tip-sample distances of  $z = 18$  nm. Sum and difference of the images (d) and (e) divided by two correspond to the topographic and magnetic contributions of the MFM signal and are shown in (f) and (g), respectively. In panel (h), the contour lines of the FM domains (b) were overlaid to the magnetic contrast (g). By comparing (b) with (h) it becomes apparent that the average contrast under the black and white domains is white and black, respectively, indicating an antiparallel alignment of the UCS in the AFM and the FM magnetization.

tip magnetisation. As the total area of the white domains became slightly smaller their magnetisation direction has to be antiparallel to the applied field. The image is taken at a tip-sample distance of 10 nm and the frequency shift contrast is about 55 Hz. The field

is then further increased to +600 mT where an MFM image is acquired at a tip-sample distance of 13 nm. The corresponding MFM image has a  $\Delta$ -f-range of 45 Hz and is shown in Fig. 5.10 (c). At +800 mT, the ferromagnetic layers are completely saturated such that they do not contribute to the measured MFM contrast. The measured frequency shift in Fig. 5.10 (d) thus arises from the UCS in the AFM layers as well as from sample topography. The above described procedure is now applied to separate topographic and magnetic signal. The images taken at +800 mT (d) and -800 mT (e) both exhibit a contrast of about 6 Hz. The difference of the images (d) and (e), divided by two, reflects the topography induced  $\Delta$ f-signal, about 3 Hz, which corresponds to half of the original signal (see Fig. 5.10 (f)). The magnetic contribution is then obtained by adding images (d) and (e) and dividing by two. It is shown in Fig. 5.10 (g) and is characterised by the slightly “smoother” contrast, typical for magnetic images. The contour lines of the initial ferromagnetic domains (see (b)) are extracted and superimposed to the magnetic contrast attributed to uncompensated magnetisation in the AFM (h). From a comparison of (b) and (h) it becomes clearly visible that the uncompensated moments in the AFM are aligned antiparallel to the adjacent ferromagnetic spins as found earlier by Kappenberger et al. It is important to note that at some locations (see red circles in (h)), a ferromagnetic alignment of the UCS of the AFM and the spins of the FM is observed. This, and the considerable variation of the contrast strongly suggests that the interfacial coupling between FM and AFM is rather inhomogeneous. However, as the MFM signal arises from the UCS contained in the 11 antiferromagnetic layers of this sample, it becomes impossible to isolate the variations of the UCS-density of a single FM/AFM interface.

For a more quantitative conclusion, we calculate the average AFM-contrast under the initial domains of the FM. The averaged frequency shift signal under the white domains was determined to be  $\Delta f_{white} = -0.49$  Hz, whereas the average contrast under the black domains is  $\Delta f_{black} = +0.41$  Hz. This again shows that the UCS of the AFM couple antiferromagnetically to the FM spins, in average. The small difference of only 0.08 Hz found between the average values under the black and white domains can be explained as follows: The MFM image from which the domain contour lines were deduced (b) was measured in +400 mT. Therefore the white domains only cover 44 % of the total surface.

### MFM Images of the IrMn/CoFePd-Multilayer Sample

Here, the MFM measurements performed on the IrMn/CoFePd-multilayer sample (see section 5.2.1) are presented. To be able to compare the results of the IrMn/CoPt-multilayer sample with the ones of the CoO/CoPt-multilayer sample, the experimental procedure is repeated. First, the sample is imaged in a demagnetised stripe domain state as first done by Kappenberger et al. and described in section 5.3. Second, the sample is investigated in its as grown domain state.

In the first experiment, the sample is demagnetised at room temperature by applying an oscillatory and decaying magnetic field parallel to the sample plane. Then the sample is zero-field cooled to 8.3 K. The  $3 \times 3 \mu\text{m}^2$  sized MFM-images are shown in Fig. 5.11: The image shown in panel (a) is taken in a magnetic field (parallel to the tip magnetization) of +50 mT to stabilise the tip magnetisation, the tip-sample distance is 25 nm and the total frequency shift range is 35 Hz. After increasing the field to +300mT, the total area of the white domains starts to shrink and contrast range decreases to 33 Hz (b). In a field of +500

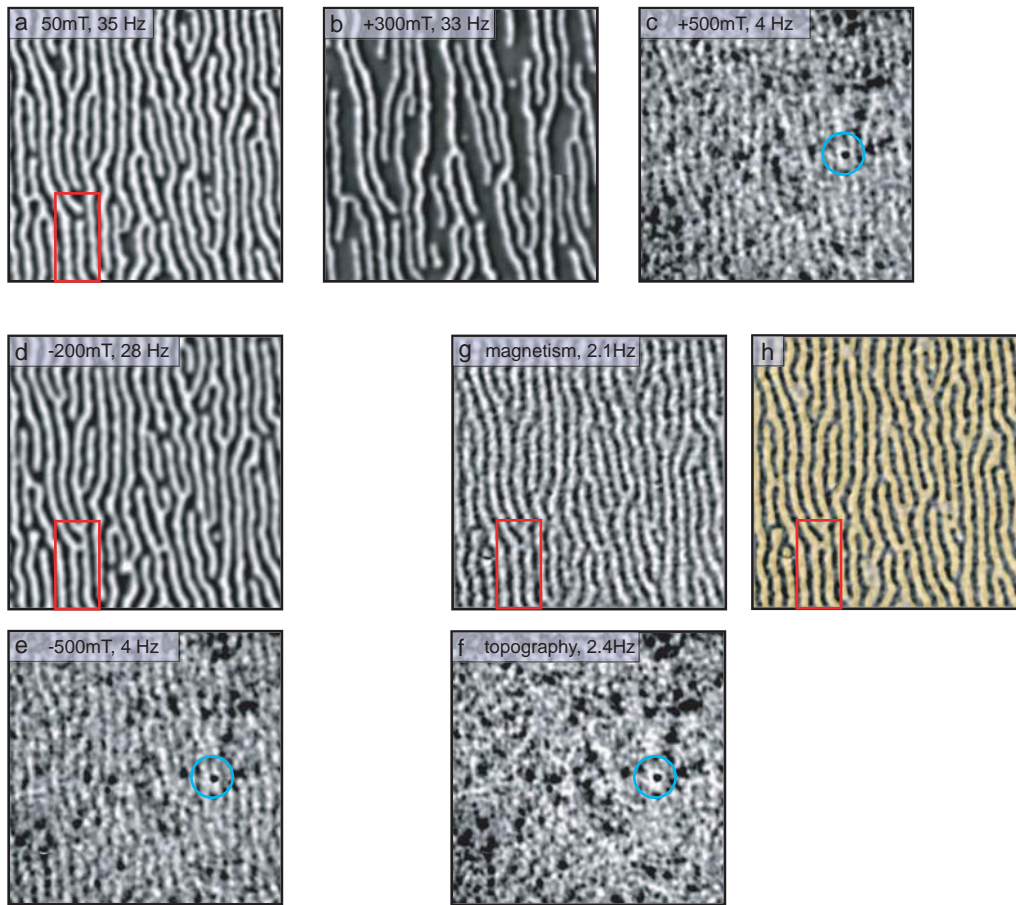


Figure 5.11: MFM images of the IrMn/CoFePd-multilayer sample in a stripe domain state: All images shown are  $3 \times 3 \mu\text{m}^2$  sized. Panel (a) shows the ferromagnetic stripe domain pattern after zero-field cooling, the image was taken in a field of +50 mT to stabilise the tip magnetisation. In a field of +300 mT, the white domains that have a magnetisation opposite to the applied field begin to vanish. In +500 mT the FM-layers are saturated and a weak, grainy contrast becomes visible (c). However, the dark spots (e.g. the one indicated by a blue circle) are a strong indication for a local contrast variation due to a topographical feature. To be able to separate topography from magnetism, additional measurements were taken in negative fields: The image in (d) was taken in -200 mT and shows a stripe domain pattern which is nearly equal to the inverted pattern of image (a). The contrast inversion is due to the reversed tip magnetisation direction (see red boxes in (a) and (d)). Finally an image was taken in a negative saturation field of -500 mT (e). The purely magnetic and topographic contributions are shown in (f) and (g), respectively. The black and white domains of the initial pattern (a) were coloured in semi-transparent yellow and transparent, respectively, and overlaid to the magnetic contrast (g). From the resulting image (h), it becomes apparent that the “yellow” domain pattern completely coincides with the inverted initial domain pattern, i.e. the pinned UCS of the AFM layers couple antiparallel to the adjacent FM spins. The measurements distance of the “ferromagnetic” images ((a), (b) and (d)) was between 25 and 30 nm, whereas the images (c) and (e) were taken at 17 nm.

mT the FM layers are completely saturated and a weak and grainy stripe domain pattern becomes visible (c). The imaging distance is decreased to  $z = 17$  nm and the frequency shift signal is 4 Hz. The numerous black spots, such as the ones highlighted by a blue circle, very likely originate from the sample topography. As explained in section 5.3.1, it is possible to separate contribution from topography and magnetism by taking a second image with reversed tip magnetisation direction. Therefore the field was first reversed to -200 mT, where a ferromagnetic stripe domain pattern recovers (d). The observed stripe domain pattern is nearly equal to the inverse of the original domain pattern observed after field cooling (shown in (a)). Note that the contrast inversion only arises from the inverted tip magnetisation (see red boxes in (a), (d) and (g)). Then the field is increased to the negative saturation field of -500 mT (e). The imaging distance is chosen to be equal to that of image (c) such that the measurement signal become equal (4 Hz). Again, a weak, grainy stripe domain contrast becomes visible. Some of the black spots (see blue circle in (e)) can now clearly be attributed to topographical features because their contrast is not inverted. The magnetic and topographic contributions to the contrast are separated and shown in (g) and (f), respectively. In the purely magnetic contribution (g), a stripe domain pattern becomes apparent and can be compared to the initial domain pattern of the FM (see (a)). When the initial domain pattern is overlaid (semi-transparent yellow) onto the AFM-contrast (g), an antiferromagnetic alignment of the UCS with the spins of the FM (see (h)) can be easily identified. This agrees with our previous observations [19] on the CoO/CoPt-multilayer sample.

As for the CoO/CoPt-multilayer sample, the measurements series is repeated for the sample being in its as-grown domain state. After zero-field cooling to 8.3 K,  $3 \times 3 \mu\text{m}^2$  sized MFM images are taken and are shown in Fig. 5.11. Images are taken in 0 T (a), in +300 mT field (b) and in +400 mT field (c) and show a maze like domain state and its changes with increasing field. Then, the field is increased to +500 mT where the FM layers are saturated and finally lowered to +50 mT where the FM domains remained saturated. This ensures that the pinned UCS remained in their original orientation and were not rotated towards the direction of the externally applied magnetic field. However, the difference between the  $\Delta f$ -signal of the AFM-contrast measured in the saturation field (+500 mT) and in +50 mT field is very small. The AFM-contrast only starts to decrease significantly above a field strength of 1 T. A systematic study of the frequency shift signal of the AFM-contrast versus applied field, as done for the CoO/CoPt-multilayer sample [60], still needs to be done.

The AFM-contrast imaged in +50 mT is weak (1.4 Hz) and grainy. Note that the AFM-contrast is imaged at a quite large the tip-sample distance of 31nm. This helps to reduce strong contributions of topography artefacts to the frequency shift signal (as seen in Fig. 5.11 (c) and (e)). In order to compare the grainy contrast of the UCS spins with the original FM-domain pattern (a), contour lines of image (a) were drawn and superimposed to image (d). The result is shown in (e). As expected, the alignment of the pinned UCS of the AFM by the adjacent FM spins is again antiparallel.

When decreasing the field back to zero, another interesting observation was made: The originally observed ferromagnetic domain pattern (a) recovers almost completely, which indicates that the sample has a very low remanence also at low temperatures. In order to

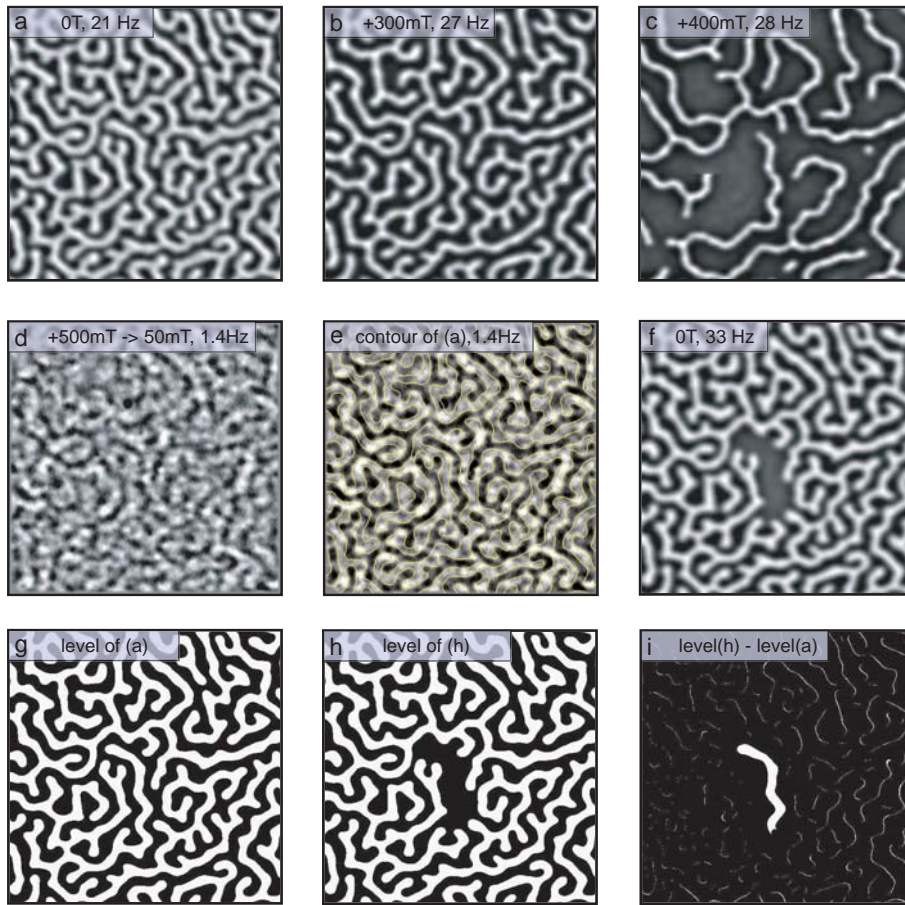


Figure 5.12: MFM images of the IrMn/CoFePd-multilayer sample in a as grown domain state: All images shown are  $3 \times 3 \mu\text{m}^2$  sized. Panel (a), (b) and (c) show the FM domain patterns obtained after zero-field cooling, and in the applied fields of +300 mT and +400 mT, respectively. Image (d) was taken in a field of +50 mT after having applied a saturating field of +500 mT. The contour lines of the initial FM domain pattern shown in (a) are overlaid to the AFM-contrast (d). The resulting image (e) again reveals an antiparallel alignment of the uncompensated AFM spins by the FM spins. By decreasing the field back to zero, the original domain pattern (a) recovers almost completely (f). To see eventual discrepancies between the original (a) and the recovered domain pattern (f), “level patterns” were determined by applying a discrimination procedure and are shown in (g) and (h) respectively. The difference of (g) and (h) is shown in (i). Besides one missing domain part in (f), the recovered domain pattern exactly matches the original pattern (a).

detect eventual discrepancies between the original (a) and the recovered domain pattern (f), level patterns of (a) and (f) were determined by applying a discrimination procedure. The resulting black and white level patterns of the original and the recovered FM domains are shown in panel (g) and (h), respectively. The difference, (g)-(h), was calculated and is

shown in (f). The recovered FM domain pattern exactly matches the original one of image (a), up to one domain fragment. The complete recovery of the original domain state was obtained by applying a small negative field (not shown).

### 5.3.2 New Microscopic Model Based on our Experimental Data

All MFM measurements performed on the CoO/CoPt- and IrMn-multilayer samples confirm the MFM data of Kappenberger et al., indicating an antiparallel alignment of pinned UCS of the AFM with the spins of the FM. Thus, a contradiction between all our MFM data and all our magnetometry data (section 5.2.3), which reveal a parallel alignment of the UCS by the FM spins, becomes apparent. This apparent contradiction can be resolved by introducing a new model in which, in addition to the compensated antiferromagnetically ordered spins of the AFM and to the non-pinned (freely rotating) UCS, two groups of pinned UCS exist. From our magnetometry data we draw the following conclusion: A first group of pinned spins with a total pinned uncompensated magnetic moment  $m_{bulk}$  is located in the bulk of the AFM. These spins would couple to any magnetic field applied to the AFM while cooling below  $T_N$ . The cooling-field  $H_{cool}$  can be externally applied but may also arise from a non-uniform magnetization distribution (i.e. domains) in the FM. The existence of pinned UCS that couple solely to an external magnetic field was proven by Takano et al. [13, 38] who measured pinned magnetic moments as a thermoremanent magnetisation (TRM) (see section 2.2.2) even for an antiferromagnetic CoO thin film that was not coupled to any ferromagnetic layer. The second group of pinned UCS has a total magnetic moment  $m_{int}$  and is (strongly) exchange-coupled and antiferromagnetically aligned to the adjacent FM spins. These spins must thus be located in the vicinity of the AFM/FM interface. Clearly, this second group also couples parallel to an external magnetic field, but the antiferromagnetic exchange coupling to the FM will dominate and such that these UCS remain aligned antiparallel to the FM spins. The existence of pinned UCS aligned antiparallel to the spins of the FM is unmistakably visible in our MFM images (see section 5.3.1). A schematic of the model introduced above is shown in Fig. 5.13 (a).

In the following, our magnetometry and MFM data are explained in depth by the above-introduced model: The magnetometry experiments (see section 5.2.3) were performed on samples that were field-cooled to 8.3 K in a field of 1.5 T (in accordance with experiments performed by other groups). According to our model, the saturated FM layers are expected to generate sheets of pinned UCS interfacial spins aligned antiparallel to the cooling-field. In addition, pinned UCS that are co-linear with the cooling field will appear in the bulk of the AFM layers. The positive vertical shift of the hysteresis loop  $m_{vs}$  measured for both samples reveals that

$$m_{vs} = m_{bulk} + m_{int} > 0, \quad (5.1)$$

and our model implies that  $m_{int} < 0$ . Hence,  $m_{bulk} > |m_{int}|$ .

The MFM senses the stray field emanating from the sample. It arises from the spatial distributions of the pinned UCS existing in the bulk and at the interfaces of each of the AFM layers. A detailed calculation (see section 3.3.1 and 5.3.4) reveals that for thin AFM layers, the bulk and interfacial UCS contribute to the measured stray field proportionally to their moments  $m_{bulk}$  and  $m_{int}$ . Our MFM data reveals that the stray field due to the pinned uncompensated spins  $H_{UCS}^{total}(x,y,z)$  is more granular than that of the stray field

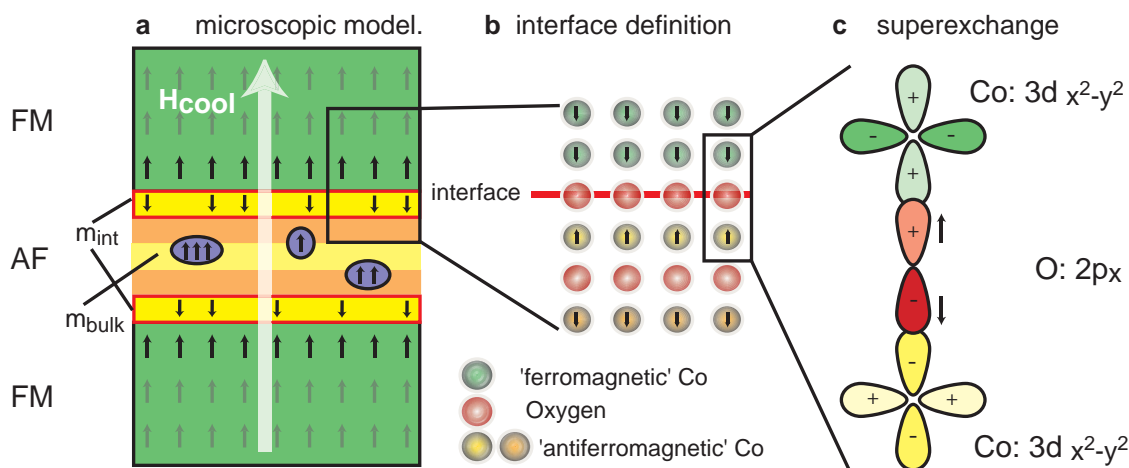


Figure 5.13: New microscopic model and superexchange coupling: Panel (a) shows the microscopic model deduced from measurements done in this thesis. The position of the AFM/FM interface is defined at the first Oxygen layer separating the AFM from the FM layer (b). The antiferromagnetic alignment of the pinned interfacial spins of the AF to the ferromagnetic spins can then be explained by superexchange coupling (c).

distribution  $H_{FM}^{total}(x,y,z)$  of the ferromagnetic domains of the FM layers. Furthermore, the MFM images clearly show that for most  $xy$ -positions,  $H_{UCS}^{total}(x,y,z)$  and  $H_{FM}^{total}(x,y,z)$  have opposite directions. This leads to the conclusion that

$$m_{bulk} + m_{int} < 0 \quad \text{and} \quad m_{int} < 0, \quad \text{hence} \quad |m_{int}| > m_{bulk}, \quad (5.2)$$

in apparent contradiction to the UCS configuration of the magnetometry experiments.

The dominance of the interfacial spins is explained as follows: for the MFM experiments the samples were zero-field cooled with the FM layers in a (demagnetized) stripe domain state. The stripe domains in the FM layers generate a corresponding magnetic field pattern of about 220 mT amplitude for the CoO/CoPt-multilayer sample and 210 mT for the IrMn/CoPd-multilayer sample. This field is locally applied to the AFM layer. Thus,  $m_{bulk}$  in the MFM experiment is expected to be non-zero but small compared to the amount of bulk moment “created” by the a about 10 times higher cooling field applied in the magnetometry experiment.

A possible mechanism for the antiparallel alignment of the interfacial UCS in the AFM to the neighbouring ferromagnetic spins in the CoO/CoPt-multilayer sample is the so-called *superexchange coupling*. In ferromagnets, the electrons on neighbouring magnetic atoms interact via an exchange interaction known as *direct exchange*. However, the magnetic coupling in magnetic oxides cannot be explained by the mechanism of direct exchange. The ions on which the magnetic moment is known to be located are too far apart and there is an insufficient direct overlap between “magnetic” orbitals. Kramers (1934) [62] and Anderson (1950) [63] proposed the superexchange mechanism in which the spins of a transition metal ion (here  $\text{Co}^{2+}$ ) are coupled indirectly through an intervening non-magnetic ion (here  $\text{O}^{2-}$ ), having a  $p$ -orbital in the ground state. The  $p$ -orbital of



the Oxygen ion can exchange an electron with each of the adjacent  $3d$  orbitals of the transition metal ions. In most cases the direct exchange between two adjacent atoms in a FM is stronger than the indirect superexchange between two moments in an AFM, that is mediated via the oxygen. This is reflected by the fact that  $T_C > T_N$ . Therefore the “last” atom that is directly coupled to its neighbour is attributed to be part of the FM. The position of the FM/AFM-interface is thus defined through the first oxygen layer separating the FM from the bulk of the AFM as indicated in Fig. 5.13 (b). A schematic of the orbitals involved in the superexchange coupling is shown in Fig. 5.13 (c). The doubly occupied  $p_x$  orbital of the  $O^{2-}$  ion has two electrons of opposite spin and stretches towards the neighbouring Co ions. The  $3d$  orbitals of the (green)  $Co^{2+}$  ion already contains 5 electrons and must therefore (Hund’s rule) accept an electron of opposite spin. The remaining electron in the  $p$  orbital of the oxygen must have a spin antiparallel to that already transferred and is given to the second neighbouring  $Co^{2+}$  ion (yellow). As a result, the total spins of the two  $Co^{2+}$  ions becomes antiparallel.

### 5.3.3 Verification of the New Microscopic Model

In the previous section the apparent contradiction between our MFM and magnetometry data is attributed to the different cooling fields  $H_{cool}$  acting on the AFM layers in the MFM and the magnetometry experiment. In the MFM experiment, the cooling field is generated by a domain pattern in the FM layer and remains relatively small. In most cases, the cooling fields applied in the magnetometry experiments are much higher (1.5 - 2 T). The number of bulk spins which align parallel to the cooling field is roughly proportional to the magnitude of the applied cooling field. This is deduced from the measurement of  $m_{vs}$  versus  $H_{cool}$ , the applied field.  $m_{vs}$  versus  $H_{cool}$  shows a strong linear increase for small and medium field, then saturates and becomes constant for high cooling fields. This behaviour is observed for both FM/AFM-multilayer samples (not shown) and was also described in literature for similar systems [34]. In contrast, the number of antiparallel aligned interfacial spins remains roughly constant with increasing cooling field. Therefore, conform results can be expected (i.e. a negative horizontal loop shift), if the vertical hysteresis loop shift is determined for a sample that was cooled in a similarly low field as the one generated from the FM domain pattern. However, in the case of our samples this strategy is not applicable: a closer look at the hysteresis loops taken at room temperature shown in Fig. 5.5 and 5.6 (a) reveals that both multilayer samples only saturate in field above 200 mT. If the samples are cooled in a field below 200 mT, the FM layers will decay in a domain state and the interpretation of an eventual vertical shift determined from a hysteresis loop becomes non trivial.

To further test the validity of our model we design a new exchange biased sample which exhibits a high remanence at room temperature. Such a sample can be cooled in zero-field in an almost saturated state. Thus,  $m_{bulk}$  will remain small and  $m_{int}$  is maximised. Therefore a negative vertical shift of the hysteresis loop can be expected. This third sample of the structure Si:Pt(200nm)CoO(12Å)[Co(4Å)Pt7Å]<sub>10</sub> Co(4Å) CoO(12Å)Pt(2nm) was prepared using a higher sputtering pressure. In earlier experiments it was found that this leads to a higher remanence at room temperature. The sample is first driven into saturation (applied field 2T) at room temperature and then cooled in various fields between 0 T and 7 T. Fig. 5.14 (a) shows the hysteresis loops of the multilayer sample at room

temperature (red), after zero-field cooling (green) and after field-cooling in 2 T (blue) to 8.3 K . The remanence achieved at room temperature is about 70 % of the saturation magnetisation. Due to the high remanence, the majority of the domains in the FM layers will have a magnetization parallel to the field used for saturation. Thus, the majority of the interfacial moments  $m_{int}$  will be antiparallel to the saturation field, when the sample is zero-field cooled. According to our model, the bulk moments are affected by the cooling field only, being negligible in zero-field cooling, and the alignment of the interfacial spins will be governed by the competition of the cooling field and the exchange field. The latter is expected to dominate, leading to an antiparallel orientation of the interfacial UCS with the FM spins. Consequently, for low external fields we expect a negative vertical shift of the magnetization loop, while for high fields we expect a positive shift.

Fig. 5.14 (b) shows the vertical shift of the hysteresis loop as a function of cooling field. Note that  $m_{vs}$  is the average value obtained from positive and negative cooling fields. The data confirms the predicted transition from a negative to a positive vertical loop shift for cooling in zero and in sufficiently high fields. For sufficiently small cooling fields the loop shift is negative. This proves that the UCS arising from exchange interaction between the AFM and FM spins are indeed aligned antiparallel to the FM spins. In addition, the loops show an exchange bias field that slightly decreases with increasing cooling fields. This can be explained by a reduction of the interfacial moments which start to cant due to the external field.

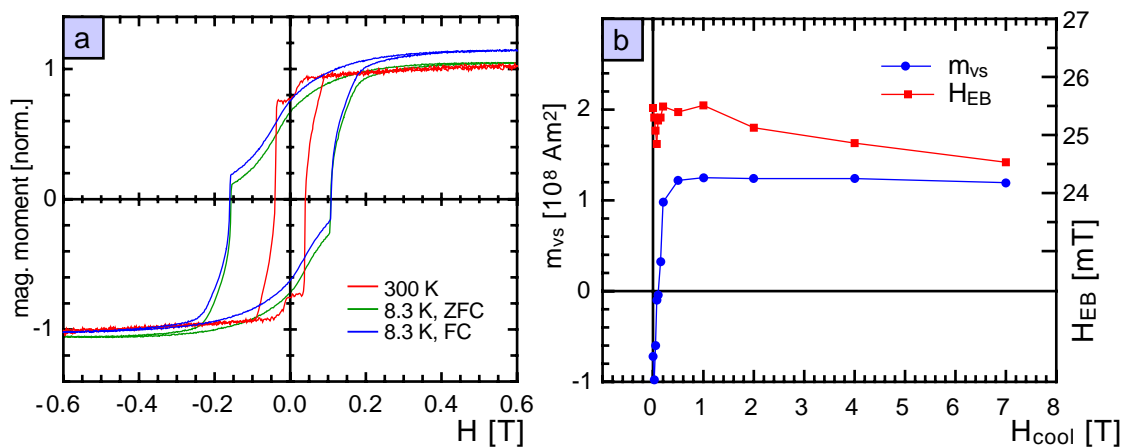


Figure 5.14: Hysteresis loops and vertical shift of a FM/AFM-multilayer sample exhibiting a high remanence at room temperature: Hysteresis loops acquired at room temperature (red), at 8.3 K after zero-field cooling (green) and after field-cooling in 2 T are shown in (a). Panel (b) shows the vertical hysteresis loop shift  $m_{vs}$  as a function of applied cooling field (blue curve). As expected, a transition from negative to positive values can be observed. The exchange bias field slightly decreases for high cooling fields (red curve).

### 5.3.4 Determination of the Averaged UCS-Density in the AFM

A quantitative analysis of the contrast due to the pinned uncompensated spins in the AFM layer (AFM-contrast) can be obtained by means of quantitative magnetic force microscopy (QMFM) techniques introduced in section 3.3.3. Kappenberger et al. [19, 60] quantitatively analyzed the AFM-contrast measured in +800 mT field (see Fig. 5.8 (b)) and found that it can be simulated by an average uncompensated spin density at each FM/AFM interface of 7% of a fully uncompensated monolayer. It has to be emphasised that according to our new model (5.3.2) the reported density of UCS does not solely reflect the interfacial spins but rather to the sum of interfacial and bulk moments. If the number of parallel aligned bulk spins in the AFM layers differs from zero, the “real” number of uncompensated spins located at the interface is even larger than the 7%.

Here we present a new quantitative analysis of the AFM-contrast which can be divided in the following steps:

- (1) Simulating the stray field of the UCS with Eq. 3.20, which calculates the stray field of a “atomically” thin AFM layer.
- (2) take into account contributions of interfacial and bulk spins as shown in the new model described in 5.3.2.

#### Calculation of the Stay Field Generated by the UCS in a Single AFM Layer

In order to calculate the stray field emanating from the UCS of the  $i$ -th AFM layer, the following quantities are defined:

$m_{bulk}^i(x, y, z)$  is the spacial distribution of the UCS bulk moments in the  $i$ -th AFM layer and  $m_{int}^i(x, y, z)$  is the spacial distribution of the UCS interfacial moments coupled to the spins of the FM layer. The antiferromagnetic layers investigated in this thesis are thin ( $d_{AFM} \leq 2.2$  nm) and the “thickness” of the interfacial spin layer coupled to the FM spins is even smaller. Thus, magnetic moments existing at different  $z$ -positions within a single AFM layer can all be projected onto the  $z$ -position in the middle of the AFM layer. Then the UCS of each layer are characterised by

$$m_{bulk}^i(x, y) = \int_{i-thAFMlayer} m_{bulk}^i(x, y, z) \quad (5.3)$$

$$m_{int}^i(x, y) = \int_{i-thAFMlayer} m_{int}^i(x, y, z), \quad (5.4)$$

where  $m_{bulk}^i(x, y)$  is the magnetic moment of the bulk and  $m_{int}^i(x, y)$  of all interfacial spins. As a further approximation we assume that all AFM layer have the same distribution of bulk and interfacial spins. Hence, the index defining a specific layer can be omitted. A further simplification is made by assuming that

$$m_{bulk}(x, y) = \alpha m_{int}(x, y), \quad (5.5)$$

where  $\alpha \in \mathfrak{R}$  depends on the externally applied cooling field, but also on the internal field during cool-down.

The stray field generated by all the pinned UCS in the  $i$ -th AFM layer,  $H_{AFM}^i(\mathbf{k})$ , is now calculated according the model described in section 5.3.2. With the two simplifications

and Eq. 3.20, the 2-D Fourier transform of the stray field distribution  $H_{AFM}^i(\mathbf{k})$  can be calculated:

$$H_{AFM}^i(\mathbf{k}) = \frac{ke^{-kz}}{2A} \cdot [m_{int}^i(\mathbf{k}) + m_{bulk}^i(\mathbf{k})] \quad (5.6)$$

$$=: \frac{ke^{-kz}}{2} \cdot \left[ \frac{m_{AFM}^i(\mathbf{k})}{A} \right]. \quad (5.7)$$

### Calculation of the Stray Field of a FM/AFM Multilayer Sample

In order to qualitatively analyse the MFM data of FM/AFM-multilayer samples, the expression of the total stray field generated by all ferromagnetic layers,  $H_{FM}^{multi}$ , as well by all antiferromagnetic layers,  $H_{AFM}^{tot}$ , of such a sample must be calculated. We consider a general FM/AFM-multilayer sample with  $n$  AFM layers of the thickness  $d_{AFM}$  and  $(n+1)$  FM layers of the thickness  $d_{FM}$ . The period length then is  $d = d_{AFM} + d_{FM}$ . First the total stray field of the perpendicularly magnetised FM layers at a distance  $z$  above the sample surface is calculated using Eq. 3.18:

$$\begin{aligned} H_{FM}^{multi}(\mathbf{k}) &= \frac{(1 - e^{-kd_{FM}})M_{FM}(\mathbf{k})}{2} e^{-kz+0d} + \dots + \frac{(1 - e^{-kd_{FM}})M_{FM}(\mathbf{k})}{2} e^{-k(z+nd)} \\ &= \frac{(1 - e^{-kd_{FM}})M_{FM}(\mathbf{k})}{2} \cdot \left[ \sum_{i=0}^n e^{-k \cdot id} \right] \end{aligned} \quad (5.8)$$

$$= H_{FM}(\mathbf{k}) \cdot \left( \frac{e^{-kd(n+1)} - 1}{e^{-kd} - 1} \right), \quad \text{where} \quad (5.9)$$

$$H_{FM}(\mathbf{k}) = \frac{e^{-k \cdot z} \cdot (1 - e^{-k \cdot d_{FM}})}{2} \cdot M_{FM}(\mathbf{k}).$$

Eq. 5.9 shows that the stray field generated by the FM layers in a FM/AFM-multilayer can be calculated by multiplying the stray field of a single ferromagnetic layer with a structural factor. The latter depends on the period given by the thickness of the FM and AFM layer, on the number of FM layers  $n$  and on the spacial wave vector  $k$ .

A similar expression for the stray field of the AFM layers in an FM/AFM-multilayer sample can be derived using Eq. 5.7.

$$H_{AFM}^{multi}(\mathbf{k}) = ke^{-kz+d_{FM}} \left[ \frac{m_{AFM}^i(\mathbf{k})}{A} \right] \cdot \left[ \sum_{i=0}^{n-1} e^{-k \cdot id} \right] \quad (5.10)$$

$$= H_{AFM}(\mathbf{k}) e^{-kd_{FM}} \cdot \left( \frac{e^{-kdn} - 1}{e^{-kd} - 1} \right), \quad \text{where} \quad (5.11)$$

$$H_{AFM}(\mathbf{k}) = \frac{ke^{-kz}}{2} \cdot \left[ \frac{m_{AFM}^i(\mathbf{k})}{A} \right].$$

Eq. 5.9 is used for the calibration of the MFM tip whereas Eq. 5.11 is used to calculate the total uncompensated spin density per AFM layer  $m_{AFM}/A$  by simulating the AFM-contrast imaged by MFM.

### Evaluation of the Uncompensated Spin Density

The image formation process of an MFM experiment is best described in form of a transfer function theory which is described in section 3.3.2. The so-called instrument calibration function  $ICF$ , defined in Eq. 3.31, transforms the z-component of the magnetic stray field into the measurement quantity which is the frequency shift signal. Once the transfer function is known, information on the micromagnetic state of the sample can be gained. Kappenberger et al. used the transfer function theory to calculate the average density of UCS in the CoO/CoPt-multilayer sample. In the following section, the procedure used by Kappenberger et al. is applied to the MFM measurements performed on the IrMn/CoFePd-multilayer sample. The main steps of the procedure used by Kappenberger et al. are resumed here:

The micromagnetic state of the sample is described by a model with a few free parameters: In practice, a discrimination procedure is applied to the measured MFM image, resulting in a “black and white” pattern which represents the spatial down/up distribution of the USC. An average uncompensated spin density is then attributed to the obtained magnetisation structure and becomes the sole free parameter that can be determined as follows.

First, the stray field is calculated using Eq. 5.11. Then, the frequency shift signal measured by MFM can be simulated using Eq. 3.31 and the previously determined ICF. The only free parameter, the UCS-density is then optimised to obtain the best match between the simulated and the measured MFM image.

Unfortunately, the above described procedure only allows for the determination of an average uncompensated spin density. In section 5.4.2, a newly developed procedure is introduced which for the first time is able to determine the local density of the UCS.

### Average Density of UCS of the IrMn/CoFePd-multilayer sample

The average density of UCS of the IrMn/CoFePd-multilayer sample is calculated using the above described method first used by Kappenberger et al. As a first step, the MFM tip is calibrated as explained in section 3.3.3. Then, a discrimination procedure is applied to the measured AFM-contrast of the IrMn/CoFePd-multilayer sample shown in Fig. 5.15 (a), resulting in a black and white magnetisation pattern shown in (b). The values attributed to the black and white areas in (b) correspond to  $-\overline{m_{AFM}/A}$  and  $+\overline{m_{AFM}/A}$ . Note that  $+\overline{m_{AFM}}$  and  $-\overline{m_{AFM}}$  are the spatial averages of  $m_{AFM}(x, y)$  within all “white” and “black” domains, respectively. The value of  $|\overline{m_{AFM}/A}|$  is optimised in order to obtain the best match between the simulated image (c) and the measured image (a). Line sections of the measured and the simulated image are shown in Fig. 5.15 (e), in red and blue lines, respectively. The best agreement of the ranges of the measured and the simulated image is obtained with the value  $|\overline{m_{AFM}/A}|=2.4 \times 10^{-4}$  [Am<sup>2</sup>/m<sup>2</sup>] as indicated by the line section shown in (d).

For comparison, the moments per unit area in the [001]-plane of IrMn were calculated based on its crystalline structure shown in Fig. 5.2 (c). Yamaoka et al. [57, 58] found an average magnetic moment of  $2.6 \pm 0.2 \mu_B$  on the Mn atom and  $0 \mu_B$  on the Ir atom for a composition of  $Mn_{1-x}Ir_x$  with  $x=0.204$ . Thereof, the magnetic moment density in the [001]-plane is calculated to be  $m_{IrMn}^{[001]}/A = 3.38 \times 10^{-4}$  [Am<sup>2</sup>/m<sup>2</sup>]. By comparison one finds that the value of  $|\overline{m_{AFM}/A}|=2.4 \times 10^{-4}$  [Am<sup>2</sup>/m<sup>2</sup>] determined from our experimental

data corresponds to about 70% of the moment density in a fully uncompensated [001]-plane of IrMn. However, it has to be re-emphasised that this value does not correspond to the number of interfacial spins, but, according to Eq. 5.7, is equal to  $|(m_{int} + m_{bulk})|$ . To be able to compare to the results obtained by Kappenberger et al., we first assume that  $m_{bulk}=0$ . The interfacial uncompensated spin density then becomes 35% of a fully uncompensated 001]-plane of IrMn. However, as discussed in section 5.3.2, it is very unlikely that no uncompensated bulk spins exist in this sample: The domains of the FM layers generate a field inside the AFM layers, even when the sample is zero-field cooled. Thus the real interfacial UCS density is probably even larger than 35 %.

The interfacial UCS-density of the CoO/CoPt-multilayer sample was recalculated using the procedure described above. A magnetic moment density  $m_{CoO}^{[111]}/A = 4.48e-4$  [ $\text{Am}^2/\text{m}^2$ ] in the [111]-plane of CoO of was calculated using an average magnetic moment of  $3.8 \mu_B$  per  $\text{Co}^{2+}$  ion [54]. Comparing this value to the value attributed to a level pattern of the AFM-contrast used for the simulation, we found 14 % of pinned UCS per AFM layer, i.e. 7 % per interface, compared to a fully uncompensated [111]-plane of CoO. This corresponds to the value calculated by Kappenberger et al. [19]. Again the 14 % reflect the sum of the interfacial and bulk UCS moments per AFM layer.

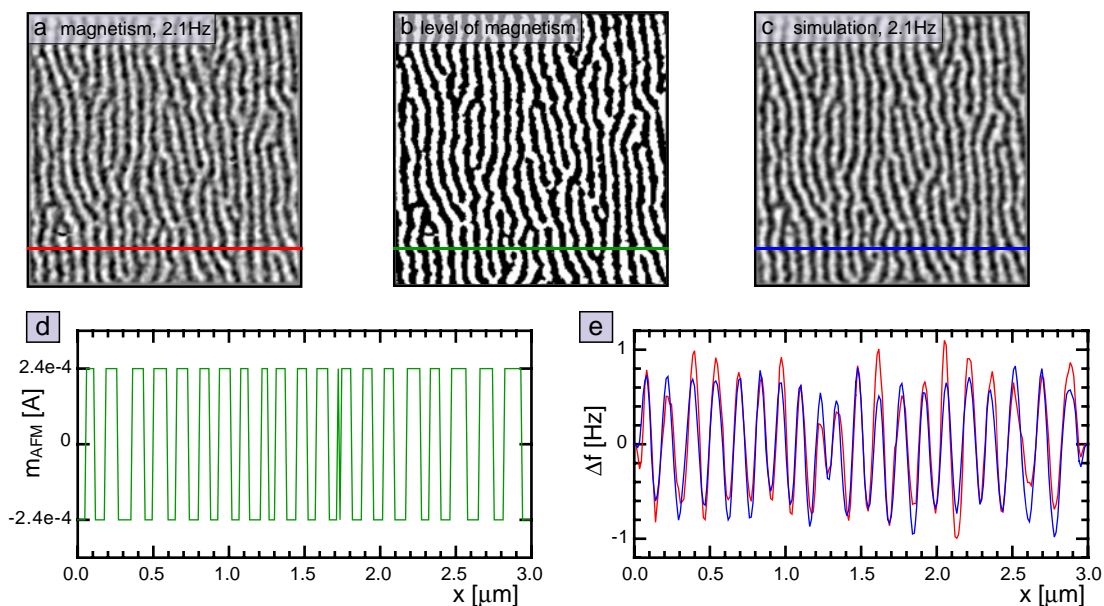


Figure 5.15: Simulation of the uncompensated spin density in the IrMn/CoFePd-multilayer sample: Panel (a) shows the measured MFM image of the AFM-contrast, (b) shows a black and white magnetisation pattern determined from (a). The best match between simulated and measured images is obtained by attributing an average magnetic moment per unit area of  $|m_{AFM}/A|=2.4 \times 10^{-4}$  [ $\text{Am}^2/\text{m}^2$ ] to the magnetisation pattern (d). Line sections of the measured (red) and the simulated image (blue) are presented in (e).

## 5.4 The Local Distribution of the Uncompensated spins

In this section we present the MFM measurements obtained on the CoO/CoPt-singlelayer sample with the structure presented Fig. 5.2.1. This sample contains only one antiferromagnetic CoO layer. Our MFM measurements reveal, as expected, a large spatial variation of the UCS-density in the CoO layer. However, the spacial average of the UCS-density still presents an antiparallel alignment of the pinned UCS in the AFM layer with the FM spins. A more quantitative evaluation reveals that the average UCS-density corresponds to about 30 % of a fully uncompensated monolayer.

In contrast to the multilayer sample, the UCS in the bulk of the AFM can be neglected here as the field generated by the FM layer is only about 100 mT. Hence, the evaluated density of UCS can be attributed to the interfacial spins only. Locally, strong variations of the UCS-density are found. In some locations up to 140 % of the interfacial AFM spins are pinned and uncompensated. In addition, the spatial distribution of the UCS presents another remarkable feature: locations with a strong positive (i.e. ferromagnetic) coupling are visible (see blue circles in Fig. 5.17). These areas seem to weaken the overall exchange bias field and are thus defined as “anti-biasing” regions. A possible interpretation of the anti-biasing regions is illustrated in section 5.4.3.

### 5.4.1 MFM Images of the CoO/CoPt-Singlelayer Sample

A series of of  $2 \times 2 \mu\text{m}^2$  sized MFM images was taken after zero-field cooling the sample in a demagnetised stripe domain state (see Fig. 5.16 (a) to (f)). A first image taken directly after zero-field cooling (a) shows a stripe domains pattern with an average stripe width of about 100 nm. MFM images taken in +100 mT and +200 mT applied fields are shown in (b) and (c), respectively. The average width of the ferromagnetic “white” domains decreases with increasing field as they are aligned antiparallel to it. In a field of +300 mT, the FM layer is saturated and the measured MFM signal mainly arises from the UCS in the AFM (d). Considering that the AFM-contrast only arises from a single, only 1 nm thick CoO layer, it is surprising to observe a quite strong (4.2 Hz at  $z = 11$  nm) frequency shift signal. A quantitative analysis of the AFM-contrast is presented in section 5.4.2. Qualitatively, an antiparallel coupling between the pinned UCS of the AFM and the adjacent FM spins is observed: The ferromagnetic domain marked with a red square (in images (a) to (c)) can clearly be re-identified with an inverted contrast in the AFM-contrast image (d).

In addition, MFM images are taken in reversed fields of -100 mT and -200 mT and shown in (e) and (f), respectively. It is interesting to note that the original orientation of the tip magnetisation is preserved even in fields up to -100 mT. It is only reversed in a field between -100 mT and -200 mT (compare magnetic domains in yellow boxes in (e) and (f)). This high coercivity of the MFM tip is very likely due to the exchange biased structure of its magnetic coating (see chapter 4).

In this sample, the local exchange bias effect is much weaker than in the previously investigated multilayer samples. The FM domain patterns observed in (a) and (e) are therefore not identical. The recovered FM domains observed in -100 mT (e) exhibit a strongly increased average domain width if compared to the FM domains observed in (a). However, the FM domain patterns observed in strong positive (+200 mT) and strong negative (-200

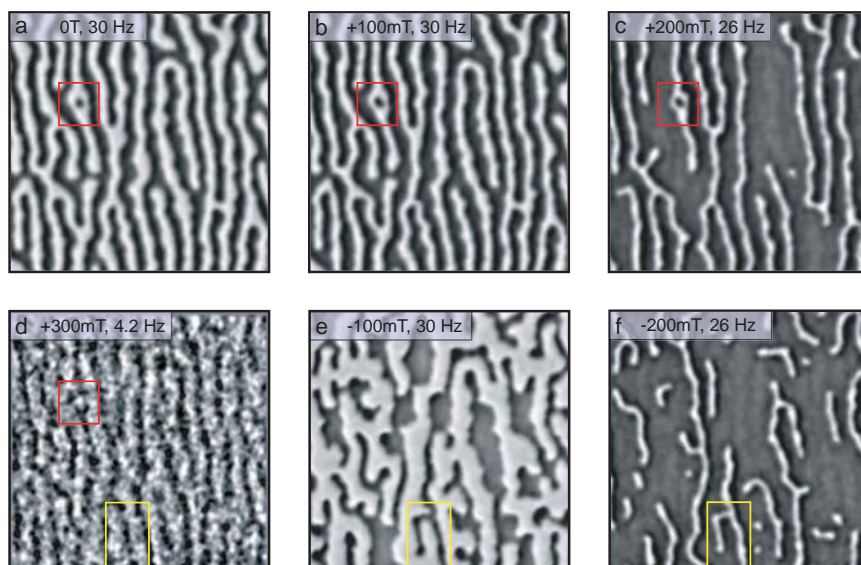


Figure 5.16:  $2 \times 2 \mu\text{m}^2$  sized MFM images of the CoO/CoPt-singlelayer sample in a stripe domain state: The evolution of the stripe domain pattern after zero-field cooling (a) is shown in panels (b) and (c) at fields of +100 mT and +200 mT, respectively. In +300 mT the FM layer is saturated and the contrast is solely due to UCS in the AFM (AFM-contrast). A contrast inversion between the FM domain pattern and the AFM-contrast can be observed (red box) from which an antiparallel alignment of the UCS spins of the AFM layer with the FM spins must be deduced. By reversing the field direction to -100 mT (e), an FM domain pattern recovers which does not correspond to the original stripe domain pattern of (a). In -200mT the domains width again becomes smaller and “stripe domain like”. Note that the tip magnetisation direction remained stable even in -100 mT field (compare yellow boxes in (e) and (f)).

mT) fields, are partially identical. Note that all images of the FM-contrast were taken at a tip-sample distance of  $z = 15 \pm 1\text{nm}$  and the image of the AFM-contrast in (d) was taken at  $z = 11\text{nm}$ .

Further MFM measurements of the CoO/CoPt-singlelayer sample were taken after zero-field cooling the sample in its as-grown domain state. MFM images were taken in 0 T, +100 mT, +200 mT and +300 mT fields and are shown in Fig. 5.17 (a) to (d), respectively. The images of the FM domain contrast shown in (a), (b) and (c) are taken at tip-sample distances of  $z = 5.0\text{nm}$ ,  $z = 5.3\text{nm}$  and  $z = 10.7\text{nm}$ , respectively. In +300 mT applied field, the FM layer becomes completely saturated and the AFM-contrast (d) appears. The image was taken at  $z = 13.1\text{nm}$ .

Contour lines of the initial domain pattern (a) and the domains remaining in a +100 mT field (c) are superimposed to the AFM-contrast (d) and are shown in (e) and (f), respectively. It becomes apparent that the average AFM-contrast under the “white” FM domain of (a) is negative (i.e. “black”). However, locally also “grey” regions, indicating



the absence of pinned UCS in the AFM, and even “white” areas (blue circles in (e)), indicating a parallel alignment of the local pinned UCS to the FM spins, can be observed. In (f) it can be observed that the “white” FM domains have a strong tendency to retract from location where the UCS are oriented parallel to the FM spins. The fact that the FM domains retract from these areas suggests that the “wrongly” oriented spins are not due to an increased local density of bulk spins, but rather to “wrongly” aligned interfacial spins. Bulk spins indeed prefer to align parallel to the FM spins (see section 5.3.2) and therefore they would even enhance the local stability of the “white” FM domains. However, this is clearly not observed. One may therefore conclude the areas containing “wrongly” oriented interfacial spins also weaken the “macroscopic” exchange field. A quantitative analysis of these qualitative observations is presented in section 5.4.2.

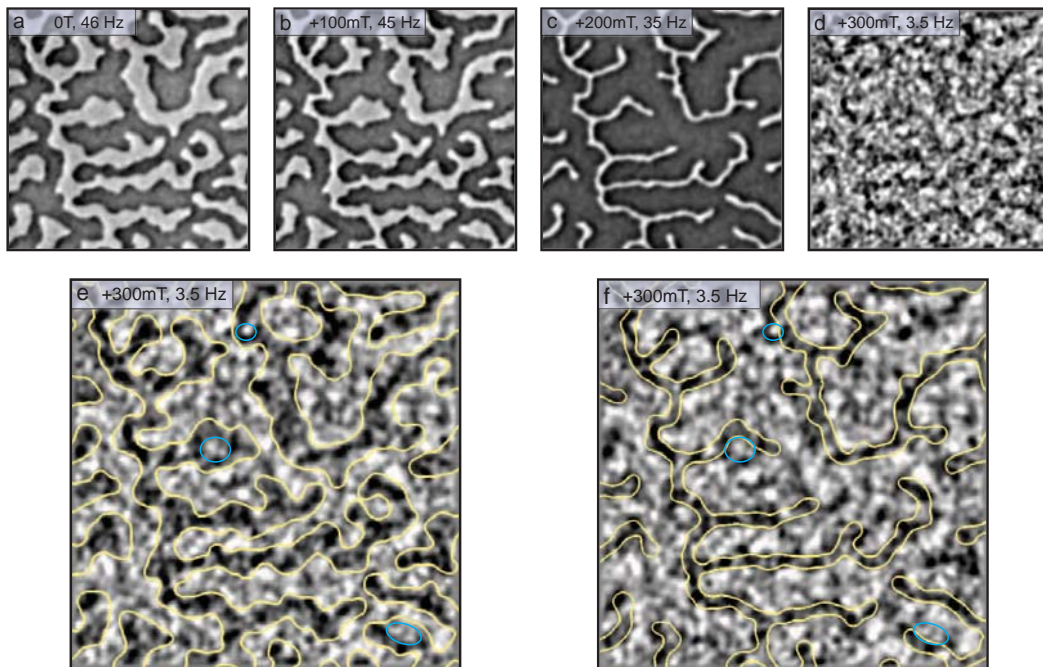


Figure 5.17: MFM images of the as-grown CoO/CoPt-singlelayer sample: The  $2 \times 2 \mu\text{m}^2$  sized MFM images are, taken in 0 mT (panel (a)), +100 mT (panel (b)) and +200 mT (panel (c)), respectively. Panel (d) shows the AFM-contrast observed in +300 mT when the FM layer is saturated. The contour lines of the FM domains in (a) and (c) were overlaid to the AFM-contrast of (d) and are shown in (e) and (f), respectively. By increasing the field from 0 to +200 mT the “white” FM domains show the tendency to retract from locations with positive coupling (anti-biasing regions, marked by blue circles) and the average AFM-contrast below these domains (see (f)) becomes more negative.

### 5.4.2 Determination of the Local Uncompensated Spin Density in the AFM

Our MFM data reveal strong local variations and thus a non-uniform spatial distribution of the pinned, uncompensated interfacial spins (see Fig. 5.17). However, the procedure described section 5.3.4 is only suitable to calculate the average distribution of UCS in an AFM layer. In the following, a new method, able to calculate the local UCS-density, is introduced. The main prerequisite thereof, is an instrument calibration function  $ICF$  with a sufficiently high signal-to-noise ratio, particularly for smaller spatial wavelengths.

In theory it is rather easy to calculate the local UCS density from the measured AFM-contrast image. The measured frequency shift is related to the total UCS distribution by

$$\Delta f(\mathbf{k}) = ICF(\mathbf{k}) \cdot \frac{d}{dz} H_{AFM} \quad (5.12)$$

$$= -ICF(\mathbf{k}) \cdot k^2 \cdot e^{-k} \left[ \frac{m_{AFM}(\mathbf{k})}{A} \right], \quad (5.13)$$

which is found by introducing Eq. 5.7 into Eq. 3.31. Solving Eq. 5.12 for  $[m_{AFM}(\mathbf{k})/A]$  results in

$$\left[ \frac{m_{AFM}(\mathbf{k})}{A} \right] = -\frac{\Delta f(\mathbf{k})}{ICF(\mathbf{k}) \cdot k^2 \cdot e^{-k}}. \quad (5.14)$$

The direct calculation of the local magnetic dipole density,  $[m_{AFM}(\mathbf{k})/A]$  thus requires the division of the Fourier transform of the measured MFM image  $\Delta f(\mathbf{k})$  by the instrument calibration function  $ICF$ , itself containing the tip transfer function  $\sigma_{tip}(\mathbf{k})$ . The tip transfer function  $\sigma_{tip}(\mathbf{k})$  is 2-dimensional complex function that describes how a specific Fourier component of the  $z$ -component of the stray field  $H_z(\mathbf{k}, z)$  is transformed into the corresponding  $z$ -component of the force,  $F_z(\mathbf{k}, z)$  (see Eq. 3.26). For large  $k$ -vectors, i.e. small spatial wavelengths, the sensitivity of the MFM tip rapidly decays (see Fig. 4.4) what limits the spatial resolution of the MFM. In other words, the signal-to-noise ratio of the MFM image becomes smaller for smaller spatial wavelengths. Consequently, the tip-transfer function also suffers from a low signal-to-noise ratio at short wavelengths as it is determined from MFM calibration images.

The calculation of the local UCS-density using Eq. 5.14 thus suffers from numerical problems generated by a small denominator with a poor signal-to-noise ratio. These problems can be overcome by the a newly developed procedure that makes use of the good rotational symmetry of the used high-aspect ratio MFM tips (see section 4.1.1). The Fourier-back-transform of the tip-transfer function is the stray field distribution of the tip in a plane located at the tip apex. Fig. 4.5 (a) clearly shows the good rotational symmetry of the tip-field and hence of the tip-transfer function. In the 2-dimensional complex tip-transfer function, the centre point reflects the tip's sensitivity for the largest spatial wavelength in the MFM image. The  $k_x, k_y$ -positions further away from the centre describe the sensitivity for shorter wavelengths, i.e. larger  $k$ -vectors.  $k_x, k_y$ -positions with a common  $k = \sqrt{k_x^2 + k_y^2}$  are elements of a circle with radius  $k$ , i.e. represent the tip's sensitivity for one specific spatial wavelength, but different direction of the  $k$ -vector. Obviously, a tip with a good circular symmetry will show only neglectable sensitivity

variations for  $k_x, k_y$ -pairs on one specific k-circle. Hence, an average over all  $k_x, k_y$ -pairs on the k-circle can be calculated. For larger k-vectors, the circumference of the k-circle is correspondingly larger which additionally improves the signal-to-noise ratio of the average. It is easy to understand that the circular averaging procedure described above generates a 1-dimensional tip-transfer function  $\sigma_{tip}(k)$  from the initially 2-dimensional function  $\sigma_{tip}(\mathbf{k})$ . In order to evaluate  $[m_{AFM}(\mathbf{k})/A]$ , a 2-dimensional function is required. Such a 2-dimensional function  $\sigma_{tip}(\mathbf{k})$  is easily calculated from the 1-dimensional  $\sigma_{tip}(k)$ ,

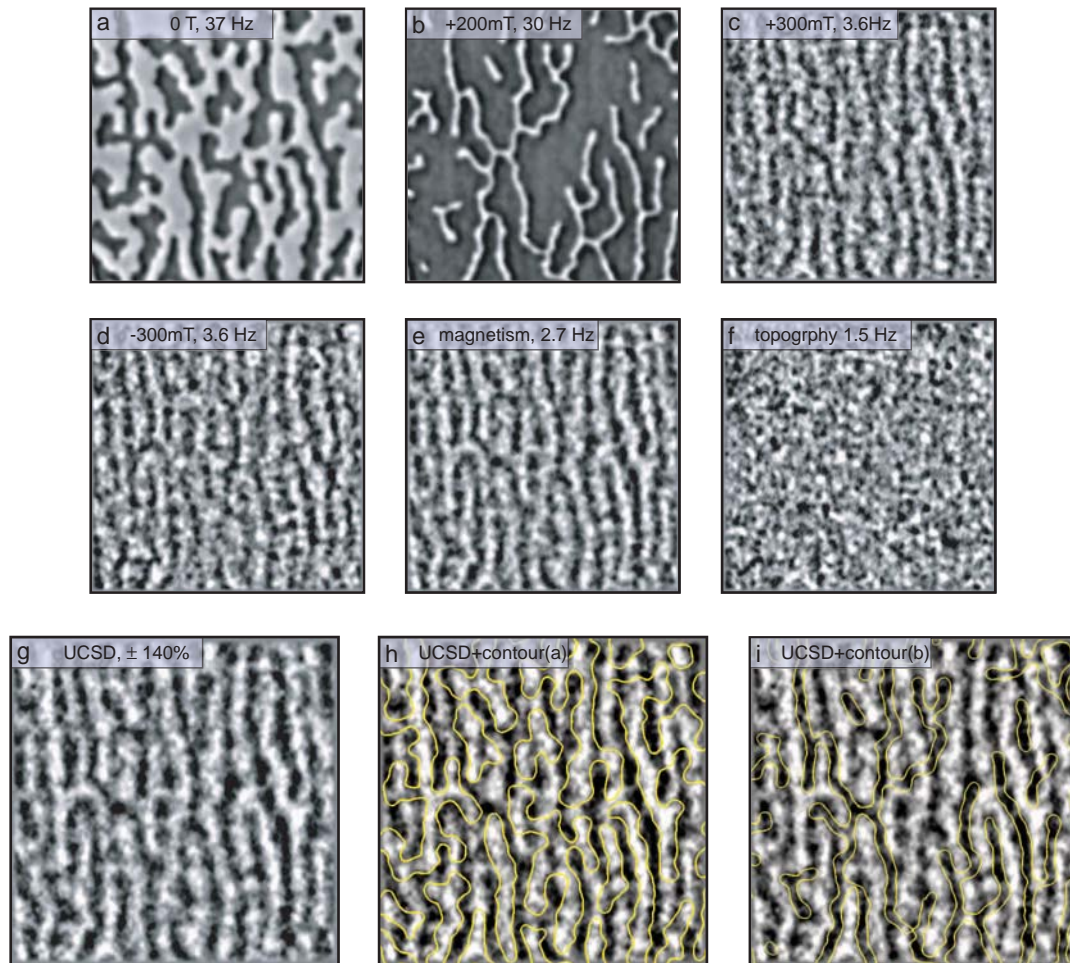


Figure 5.18: Determination of the local UCS-density in the CoO/CoPt-multilayer sample: A series of  $2 \times 2 \mu\text{m}^2$  sized MFM measurements were taken in fields of 0 T, +200 mT, +300 mT and -300 mT and are shown in panel (a) to (d) respectively. Magnetic and topographic contribution to the AFM-contrast were separated using (c) and (d) and are shown in (e) and (f), respectively. From the magnetic contrast (e), the UCS-density was calculated (g). Locally, UCS-densities of up to 140 % of a fully uncompensated monolayer do exist in the AFM layer. The average values under the FM domain pattern in zero-field (a) and +200mT are 30.5 % and 57 %, respectively.

by defining  $\overline{\sigma_{tip}(\mathbf{k})} = \sigma_{tip}(k) \forall k_x, k_y$  with  $\mathbf{k} = (k_x, k_y)$ . However, the rapid decay of the tip-transfer function at small wavelengths, i.e. below 40 nm, remains problematic. The calculated  $[m_{AFM}(\mathbf{k})/A]$  is thus low-pass-filtered with a cut-off at 40 nm, before applying the inverse Fourier transform to obtain  $[m_{AFM}(x, y)/A]$ .

For the calculation of  $[m_{AFM}(x, y)/A]$ , a series of MFM data permitting the separation of topography and magnetism of the AFM-contrast, was chosen (see Fig. 5.18).  $2 \times 2 \mu\text{m}^2$  sized images were taken in fields of 0 mT, +200 mT, +300 mT and -300 mT and are presented in Fig. 5.18 (a) to (d), respectively. Note that the sample was originally cooled in a demagnetised stripe domain state, then a few hysteresis cycles were applied. This is why the FM domains have a maze like shape (a) whereas the AFM-contrast is characterised by the originally “imprinted” stripe domain pattern ((c) and (d)). Magnetic and topographical contribution to the AFM-contrast were separated and are shown in (e) and (f), respectively. Only the magnetic contribution was used for the following calculation of the UCS-density. It is noteworthy, that the UCS distribution is directly calculated from the measured  $\Delta f$ -contrast. No fitting procedure is used. The result of the calculation, compared to the magnetic moment density of a fully uncompensated CoO [111]-plane (a spin density of  $4.48\text{e}^{-4} [\text{Am}^2/\text{m}^2]$  is obtained when using  $+3.8 \mu_B$  per  $\text{Co}^{2+}$  ion [54]), is shown in Fig. 5.18 (g). Assuming that the number of bulk spins in this sample is negligible, we locally observe very high UCS-densities. In some regions, up to 140 % of the interfacial AFM spins are pinned and uncompensated. In order to calculate the average UCS-density, the contour lines of the original FM domain pattern (a) are first superimposed to (g). The result is shown in (h). The average UCS-density is then calculated under the “white” and “black” FM domains. Under the white and black domains -28 % and +33 % is found, respectively. This difference of 5 % agrees well with the difference of area between white and black domains of the initial domain pattern. Assuming an equal coverage of black and white domains, the average UCS-density value results in of 30.5 % . In addition, the averaged UCS-density is calculated under the remaining white domains in +200 mT field (c). Therefore, the contour lines of this domain pattern are superimposed to the calculated UCS-density (g) and is represented in (i). The average UCS-density under the +200mT white domains almost doubled to 57 %. This is explained by the high Zeeman energy of domains with a magnetisation opposite to the applied field. Thus only domains stabilised by a high local exchange field remain stable.

### 5.4.3 Interpretation of High UCS-Density and Antibiasing Regions

Compared to the commonly accepted values of pinned UCS [16], we find a surprisingly large number of pinned uncompensated spins. However, the exchange bias field remains small, i.e. comparable to the values reported in literature. Hence, the exchange coupling between the UCS and the FM spins must be reduced. This can be done by either reducing the actual coupling strength of the UCS to the FM spin or by reducing the number of UCS effectively coupled to the FM. Two possible scenarios are described in the following.

(1) Possibly, the UCS do not only arise from  $\text{Co}^{2+}$  spins which are directly located at the FM/AFM interface but also from spins which are located close to the FM/AFM interface but that are not directly coupled to the FM spins. Such spins could form small “pockets” located in the bulk of the AFM layer. The measured UCS-density is then the sum of “true” interfacial spins and of spins located in “pockets” not far away from the

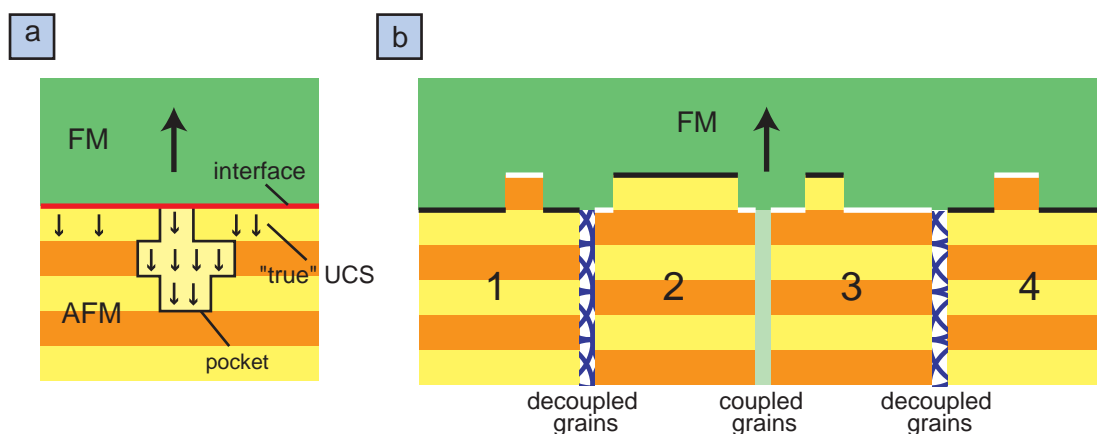


Figure 5.19: Model for the interpretation of a high local UCS-density and the antibiasing regions: panel (a) show a schematic of an FM/AFM interface where pinned UCS located close to the interface, forming small “pockets”, contribute to the high local UCS-density measured for the CoO/CoPt-singlelayer sample. Note that the spins contained in the pockets do not contribute to the exchange coupling of FM and AFM. The model in (b) explains regions where the UCS spins of the AFM align ferromagnetically to the FM spins. The net amount of UCS interfacial spins of Grain 3 are ferromagnetically aligned to the FM spins due to direct coupling to the neighbouring grains preventing a “free” alignment of this grain.

interface, (cf. Fig. 5.19 (a)). In this case, the exchange bias field would only be related to the “true” interfacial spins. Clearly, this density may be much smaller, leading to a low exchange bias field as determined from the hysteresis loop (see Fig. 5.7 (a)).

(2) In section 5.4.1 we showed that not all pinned uncompensated spins at the interface do align antiparallel to the FM spins. The fact that FM domains prefer to retract from these areas suggests that “wrongly” aligned interfacial spins, lead to a local weakening of the coupling between FM and AFM. The above findings can be explained as follows: the TEM images (Fig. 5.4) reveal that the FM/AFM interface can be described as suggested by Takano et al. (see section 2.2.2) as each AFM grain only shows a few atomic steps. Thus, at the FM/AFM interface one spin direction must dominate the other. In addition, the many different grain boundaries and misalignment angles revealed by our TEM images, indicate that a large range of inter-granular coupling strengths must exist. Fig. 5.19 (b) schematically illustrates four AFM grains biased by the FM layer. The first and the second grain, as well as the third and the fourth grain, are decoupled from each other, e.g. by a large angular misalignment. Other grains (2 and 3) are strongly coupled (small tilt-angle). Averaging the number of up- and down-spins over the terraces of decoupled grains results in a net excess of interfacial spins that are antiferromagnetically aligned to the spins of the FM. This produces a net “black” contribution to the AFM-contrast (below a “white” FM domain). However, in the case of coupled grains, one grain may “correctly” align with the FM spins, but the strong intergranular coupling may drive the neighbouring grain into a “wrongly” aligned state. This may considerably lower the strength of the coupling between

FM and AFM and produces a local net “white” contribution to the AFM-contrast. The coupling of the AFM grains not only explains the anti-biasing regions but also leads to a specific type of training effect. Zhang et al. (see section 2.2.3) showed the transition from a Type I to a Type II training effect (cf. section 2.1.3) is due to an increased strength of the intergranular coupling. Note that all the samples investigated in the thesis exhibit a Type II training effect, which corresponds to a rather strong intergranular coupling.

## Chapter 6

# Summary and Conclusions

The spin configuration on each side of the FM/AFM interface is considered as a key element in exchange biased systems and is still open to debate. It is widely accepted that pinned uncompensated spins in the AFM or at the FM/AFM interface are responsible for the exchange coupling observed in these systems. Several experiments were able to prove the existence of such pinned uncompensated spins. However, some of these experiments give conflicting results on the orientation of the UCS relative to the ferromagnetic spins. It is thus not surprising that a wide range of values of the density of UCS is found in literature [13, 14].

We investigated two different types of FM/AFM systems, with CoO and IrMn as anti-ferromagnetic layers, by high resolution quantitative magnetic force microscopy (QMFM) at low temperatures, magnetometry and transmission electron microscopy (TEM). During the course of these studies, and the analysis of the results, several before-developed procedures to obtain quantitative information from MFM measurements had to be improved. In order to prevent hysteretic modifications of the tip magnetisation by strong stray fields emanating from the sample, the coercivity of the magnetic coating of the MFM tip was improved. This was done by the oxidation of an initial cobalt layer to CoO, forming an FM/AFM bilayer system with a coercivity increased by about a factor of two, such that stable imaging conditions were obtained (see chapter 4).

One condition for obtaining high resolution MFM images is to measure at close tip-sample distances. However, at such distances the interpretation of high resolution MFM images becomes difficult because the measured contrast contains magnetic and topographic contributions. A method that allows the separation of magnetic and topographic signal is introduced in section 5.3.1.

Analytical expressions for the magnetic stray field emanating from FM/AFM-multilayer samples were derived in section 5.3.4. These expressions are necessary for a quantitative analysis of the measured MFM contrast. Until now, the procedure to quantify the measured MFM contrast was the following: the MFM contrast is simulated by using a magnetisation pattern estimated from the MFM image, the instrument calibration function (*ICF*) containing the imaging properties of the MFM tip and a few additional parameters as the saturation magnetisation or the domain wall thickness. The best parameter set is found by fitting the simulated image to the measured data (see section 3.3.3). This method works reliably if the imaged sample magnetisation can be modelled with only a

few free parameters. For example, a domain pattern in a FM material with perpendicular anisotropy consisting of up-down domains. If the FM up-down domains are clearly distinguishable in the MFM image then the magnetisation and the domain wall thickness become the only free parameters. In contrast, the distribution of spins of an FM/AFM interface is very difficult to model, because of its strong local variations. Thus, for the quantitative analysis of the this AFM-contrast, a new method, directly calculating the magnetic surface charge density or the magnetic surface dipole density, was developed in section 5.4.2. For a successful application of this method, a “noise reduction procedure” was previously applied to the *ICF*.

We analysed MFM and magnetometry data of two different FM/AFM-systems: a CoO/CoPt-multilayer and a IrMn/Co<sub>0.9</sub>Fe<sub>0.1</sub>Pd-multilayer sample. The small positive vertical shifts of the hysteresis loops found for both samples arises from pinned magnetic moments aligned parallel to the cooling field and the FM spins (see section 5.2.3). However, MFM images presented in 5.3.1, obtained after zero-field cooling the samples, indisputably revealed an antiferromagnetic coupling between the pinned UCS of the AFM and the adjacent spins of the FM. This apparent contradiction is resolved by introducing a new model (5.3.2) in which two groups of pinned UCS co-exist in the AFM. The pinned UCS responsible for the EB-effect are aligned antiparallel to the ferromagnetic spins. Additionally, pinned UCS aligned parallel to the spins of the FM do also exist, but are not responsible for the EB-effect.

In MFM measurements performed on the CoO/CoPt-singlelayer sample, a correlation between the local exchange bias field and the local UCS-density was observed (cf. 5.4.1). The dependence of the FM domain structure in the applied magnetic field and the distribution of the pinned, uncompensated spins were measured. Our data revealed a strong local variation of the spatial distribution of the pinned, uncompensated interfacial spins. The spatial average of the UCS-density in the areas initially covered by the “white” FM domains of the zero-field cooled image and of the 200 mT-image was determined to 30 % and 57 %, respectively. In addition, the local UCS-density map shows another remarkable feature, an “antibiasing-effect” ( see section 5.4.3): locations with a strong positive (i.e. ferromagnetic) coupling are visible. These areas seem to weaken the overall exchange bias field and were thus named as “antibiasing” regions. In increasing external fields, the FM domains were found to retract from these antibiasing regions. These location of “wrong” contrast are caused by “wrongly” aligned interfacial spins and not due to a locally enhanced density of bulk spins.

Surprisingly, even larger local values of the UCS-density are found. In some regions up to 140 % of the interfacial AFM spins are pinned and uncompensated. Taking into account the usually low exchange bias field the following conclusions must be drawn from the surprisingly high values of the UCS-density: the measured signal is due to few interfacial spins which are stabilized by spins in larger “pockets” near the interface. The UCS-density is consequently the sum of “true” interfacial spins and of spins located in small or large “pockets” not far away from the interface. We can speculate that the exchange bias field is mainly related to the “true” interfacial spins (see section 5.4.3)

The above findings can be explained within a simple statistical approach. The TEM images reveal that our sample satisfies the conditions of the model proposed by Takano et



al. (section 2.2.2): sharp grain interfaces with only a few crystalline, atomic steps. For our FM/AFM systems the small number of steps per grain generates a limited distribution of terrace sizes which leads to poor statistics and as a consequence to a strong local variation of the UCS-density, as indeed measured. Additionally, due to the wide range of grain boundary tilt-angles, we expect that in some cases a direct coupling between the AFM grains would be possible as proposed by Zhang et al. (section 2.2.3). Averaging the number of up- and down-spins over the terraces of decoupled grains results in a net excess of interfacial spins that are antiferromagnetically aligned to the spins of the FM. However, in the case of coupled grains, the net spins at the interface can on average be ferromagnetically ordered because of the direct coupling to the neighbouring grain. This prevents many spins from antiferromagnetically aligning, considerably lowering the exchange bias and producing a net white contribution to the AFM-contrast (i.e. an antibiasing region). From this simple picture we conclude that an appropriate design of the grain boundaries that reduces the intergranular coupling may increase the exchange bias effect.

# Bibliography

- [1] W. H. Meiklejohn and C. P. Bean. New magnetic anisotropy. *Phys. Rev.*, 102(5):1413, 1956.
- [2] W. H. Meiklejohn and C. P. Bean. New magnetic anisotropy. *Phys. Rev.*, 105(3):904, 1957.
- [3] W. H. Meiklejohn. Exchange anisotropy - a review. *J. Appl. Phys.*, 33(3):1328, 1962.
- [4] M. N. Baibich, J. M. Broto, A. Fert, F. Nguyen Van Dau, F. Petroff, P. Etienne, G. Creuzet, A. Friedrich, and J. Chazelas. Giant magnetoresistance of (001) Fe/(001)Cr magnetic superlattices. *Phys. Rev. Lett.*, 61(21):2472, 1988.
- [5] G. Binasch, P. Grünberg, F. Saurenbach, and W. Zinn. Enhanced magnetoresistance in layered magnetic structures with antiferromagnetic interlayer exchange. *Phys. Rev. B*, 39(7):4828, 1989.
- [6] T. M. Hermann, W. C. Black, and S. Hui. Magnetically coupled linear isolator. *IEEE Trans. Magn.*, 33(5):4029, 1997.
- [7] J. Daughton, J. Brown, E. Chen, R. Beech, A. Pohm, and W. Kude. Magnetic field sensors using GMR multilayer. *IEEE Trans. Magn.*, 30(6):4608, 1994.
- [8] F. B. Mancoff, J. Hunter Dunn, B. M. Clemens, and R. L. White. A giant magnetoresistance sensor for high magnetic field measurements. *Appl. Phys. Lett.*, 77(12):1879, 2000.
- [9] S. S. P. Parkin et al. Exchange-biased magnetic tunnel junctions and application to non-volatile magnetic random access memory. *J. Appl. Phys.*, 85:5828, 1999.
- [10] Yimin Guo et al. MRAM array with coupled soft-adjacent magnetic layer. *J. Appl. Phys.*, 97(10):506, 2005.
- [11] A. E. Berkowitz and K. Takano. Exchange anisotropy \* a review. *J. Magn. Magn. Matter*, 200(552), 1999.
- [12] J. Nogués and I. K. Schuller. Exchange bias. *J. Magn. Magn. Matter*, 192:203, 1999.
- [13] K. Takano, R. H. Kodama, and A. E. Berkowitz. Interfacial uncompensated antiferromagnetic spins: Role in unidirectional anisotropy in polycrystalline Ni<sub>81</sub>Fe<sub>19</sub> bilayers. *Phys. Rev. Lett.*, 79(6):1130, 1997.

- [14] W. J. Antel, F. Perjeru Jr., and G. R. Harp. Spin structure at the interface of exchange biased FeMn. *Phys. Rev. Lett.*, 83(7):1439, 1998.
- [15] H. Ohldag, T. J. Regan, J. Stöhr, A. Scholl, F. Nolting, J. Lüning, C. Stamm, S. Anders, and R. L. White. Spectroscopic identification and direct imaging of interfacial magnetic spins. *Phys. Rev. Lett.*, 87(24):247201, 2001.
- [16] H. Ohldag, A. Scholl, F. Nolting, E. Arenholz, S. Maat, A. T. Young, M. Carey, and J. Stöhr. Correlation between exchange bias and pinned interfacial spins. *Phys. Rev. Lett.*, 91(1):17203, 2003.
- [17] T. P. A. Hase, B. D. Fulthorpe, S. B. Wilkins, B. K. Tanner, C. H. Marrows, and B. J. Hickey. Weak magnetic moment on IrMn exchange bias pinning layers. *Appl. Phys. Lett.*, 79(7):985, 2001.
- [18] T. Eimüller, T. Kato, T. Mizuno, S. Tsunashima, C. Quitmann, T. Ramsvik, S. Iwata, and G. Schütz. Uncompensated spins in a micro-patterned CoFeB/MnIr exchange bias system. *J. Appl. Phys.*, 85(12):2310, 2004.
- [19] P. Kappenberger, S. Martin, Y. Pellmont, H. J. Hug, J. B. Kortright, O. Hellwig, and Eric E. Fullerton. Direct imaging and determination of the uncompensated spin density in exchange-biased CoO/(CoPt) multilayers. *Phys. Rev. Lett.*, 91(26):267202, 2003.
- [20] H. J. Hug, B. Stiefel, P. J. A. van Schendel, A. Moser, S. Martin, and H.-J. Güntherodt. A low temperature ultrahigh vacuum scanning force microscope. *Rev. Sci. Instrum.*, 70(9):3625, 1999.
- [21] G. Binnig, C. F. Quate, and Ch. Gerber. Atomic force microscopy. *Phys. Rev. Lett.*, 56:930, 1986.
- [22] Y. Martin and H. K. Wickramasinghe. Magnetic imaging by "force microscopy" with 1000 Å resolution. *Appl. Phys. Lett.*, 50:1455, 1987.
- [23] J. J. Saenz, N. Garcia, P. Grütter, E. Meyer, H. Heinzelmann, R. Wiesendanger, L. Rosenthaler, H. R. Hidber, and H.-J. Güntherodt. Magnetic domain structure by measuring magnetic forces. *J. Appl. Phys.*, 62:4293, 1987.
- [24] D. Rugar, H. J. Mamin, P. Guethner, S. E. Lambert, J. E. Stern, I. McFadyen, and T. Yogi. Magnetic force microscopy: general principles and application to longitudinal recording media. *J. Appl. Phys.*, 68(3):1169, 1990.
- [25] Hans J. Hug, B. Stiefel, P. J. A. van Schendel, A. Moser, R. Hofer, S. Martin, and H.-J. Güntherodt. Quantitative magnetic force microscopy on perpendicularly magnetized samples. *J. Appl. Phys.*, 83(11):5609, 1998.
- [26] P. J. A. van Schendel. *Investigation of Magnetization Structures in Ferromagnetic and Superconducting samples by magnetic force microscopy*. PhD thesis, University of Basel, 1999.

- [27] P. J. A. van Schendel, H. J. Hug, B. Stiefel, S. Martin, and H.-J. Güntherodt. A method for the calibration of magnetic force microscopy tips. *J. Appl. Phys.*, 88(1):435, 2000.
- [28] H. N. Fuke, K. Saito, Y. Kamiguchi, H. Iwasaki, and M. Sahashi. Spin-valve giant magnetoresistive films with antiferromagnetic Ir-Mn layers. *J. Appl. Phys.*, 81(8):4004, 1997.
- [29] D. Paccard, C. Schlenker, and O. Massenet. A new property of ferromagnetic-antiferromagnetic coupling. *Phys. Stat. Solidi*, 16:301, 1966.
- [30] J. Nogués, C. Leighton, and Ivan K. Schuller. Correlation between antiferromagnetic interface coupling and positive exchange bias. *Phys. Rev. B*, 61(2):1315, 2000.
- [31] N. C. Koon. Calculations of exchange bias in thin films with ferromagnetic/antiferromagnetic interfaces. *Phys. Rev. Lett.*, 78(25):4865, 1997.
- [32] H. Fujiwara, K. Zhang, T. Kai, and T. Zhao. Effect of direct exchange coupling between antiferromagnetic grains on magnetic behavior of ferro/antiferromagnetic exchange coupled polycrystalline layer systems. *J. Magn. Magn. Matter*, 235:319, 2001.
- [33] K. Zhang, T. Zhao, and H. Fujiwara. Training effect in ferro (f)/antiferromagnetic (af) exchange coupled systems: Dependence on af thickness. *J. Appl. Phys.*, 91(10):6902, 2002.
- [34] J. Keller, P. Miltényi, B. Beschoten, and G. Güntherodt. Domain state model for exchange bias. II. experiments. *Phys. Rev. B*, 66(1):014431, 2002.
- [35] S. Roy and et al. Depth profile of uncompensated spins in an exchange bias system. *Phys. Rev. Lett.*, 95(4):047201(4), 2005.
- [36] R. L. Stamps. Mechanisms for exchange bias. *J. Phys. D: Appl. Phys.*, 33:R247, 2000.
- [37] R. Jungblut, R. Coehoom, M. T. Johnson, J. aan de Stegge, and A. Reinders. Orientational dependence of the exchange biasing in molecular-beam-epitaxy-grown Ni<sub>80</sub>Fe<sub>20</sub>/Fe<sub>50</sub>Mn<sub>50</sub> bilayers. *J. Appl. Phys.*, 75:6659, 1994.
- [38] Kentaro Takano, R. H. Kodama, A. E. Berkowitz, W. Cao, and G. Thomas. Role of interfacial uncompensated antiferromagnetic spins in unidirectional anisotropy in Ni<sub>81</sub>Fe<sub>19</sub>/CoO bilayers invited. *J. Appl. Phys.*, 83(11):6888, 1998.
- [39] D. C. Khan and R. A. Erickson. Temperature dependence of the sublattice magnetization in cobaltous oxide. *J. Phys. Chem. Solids*, 29(12):2087, 1968.
- [40] K. Zhang, T. Zhao, and H. Fujiwara. Training effect of exchange biased iron-oxide/ferromagnet systems. *J. Appl. Phys.*, 89(11):6910, 2001.
- [41] E. Fulcomer and S. H. Charap. Thermal fluctuation aftereffect model for some systems with ferromagnetic-antiferromagnetic coupling. *J. Appl. Phys.*, 43(10):4190, 1972.

- [42] H. J. Hug, A. Moser, Th. Jung, O. Fritz, A. Wadas, I. Parashikov, and H.-J. Güntherodt. Low temperature magnetic force microscopy. *Rev. Sci. Instrum.*, 64(10):2920, 1993.
- [43] S. Foss, R. Proksch, E. D. Dahlberg, B. Moskowitz, and B. Walsh. Localized micro-magnetic perturbation of domain walls in magnetite using a magnetic force microscope. *Appl. Phys. Lett.*, 69(22):3426, 1996.
- [44] Ch. Loppacher, M. Bammerlin, E. Battiston, M. Guggisberg, D. Müller, H. R. Hidber, R. Lüthi, E. Meyer, and H.-J. Güntherodt. Fast digital electronics for application in dynamic force microscopy using high-Q cantilevers. *Appl. Phys. A*, 66:215, 1998.
- [45] R. Garcia and R. Perez. Dynamic atomic force microscopy methods. *Surf. Sci. Rep.*, 47:197, 2002.
- [46] J. D. Jackson. *Classical Electrodynamics*. J. Wiley and sons, New York, 1975.
- [47] E. Meyer, H. J. Hug, and R. Bennewitz. *Scanning Probe Microscopy*. Springer, 2004.
- [48] *Webpage: [www.team-nanotec.de](http://www.team-nanotec.de)*.
- [49] Eberhard Jäger and Rolf Perthel. *Magnetische Eigenschaften von Festkörpern*. Akademie Verlag, 1996.
- [50] E. P. Wohlfarth. *Ferromagnetic materials. A handbook on the properties of magnetically ordered substances*. North-Holland, 1980.
- [51] Z. Y. Liu. Exchange bias and vertical loop shifts in a  $\text{Co}(32\text{\AA})/\text{NiO}(10\text{\AA})/[\text{Co}(4\text{\AA})/\text{Pt}(6\text{\AA})]_4$  multilayer. *J. Appl. Phys.*, 85(21):4971, 2004.
- [52] D. Lacour, H. Jaffres, F. Nguyen Van Dau, F. Petroff, A. Vaures, and J. Humbert. Field sensing using the magnetoresistance of IrMn exchange-biased tunnel junctions. *J. Appl. Phys.*, 91(7):4655, 2002.
- [53] O. Hellwig, S. Maat, J. B. Kortright, and E. E. Fullerton. Magnetic reversal of perpendicularly-biased Co/Pt multilayers. *Phys. Rev. B*, 65:144418, 2002.
- [54] W. L. Roth. Magnetic structures of MnO, FeO, CoO, and NiO. *Phys. Rev.*, 110(6):1333–41, 1958.
- [55] B. van Laar. Multi-spin-axis structure for CoO. *Phys. Rev.*, 138(2A):A584, 1965.
- [56] D. Herrmann-Ronzaud, P. Burlet, and J. Rossat-Mignod. Equivalent type-II magnetic structures: CoO, a collinear antiferromagnet. *J. Phys. C*, 11:2123, 1978.
- [57] T. Yamaoka, M. Mekata, and H. Takaki. Neutron diffraction study of antiferromagnetism in face-centered cubic Mn-Ir alloys. *J. Phys. Soc. Japan*, 31:301, 1971.
- [58] T. Yamaoka, M. Mekata, and H. Takaki. Neutron diffraction study of  $\gamma$ -phase Mn-Ir single crystals. *J. Phys. Soc. Japan*, 36(2):438, 1974.

- [59] K. Steenbeck, R. Mattheis, and M. Diegel. Antiferromagnetic energy loss and exchange coupling of IrMn/CoFe films: experiments and simulations. *J. Magn. Magn. Matter*, 279:317, 2004.
- [60] P. Kappenberger. *Exchange Bias Effect and Hard Disk Media Studied by Means of Quantitative Magnetic Force Microscopy*. PhD thesis, University of Basel, 2005.
- [61] I. Schmid. Potentiale und grenzen der magnetkraftmikroskope bei raumtemperatur. Master's thesis, University of Basel, 2001.
- [62] H. A. Kramers. On the exchange interaction in magnetic crystals. *Physica*, 1:182, 1934.
- [63] P. W. Anderson. Antiferromagnetism. Theory of superexchange interaction. *Phys. Rev.*, 79:350, 1950.

# List of Symbols and Abbreviations

$EB - effect$	exchange bias effect
$FM$	ferromagnet, ferromagnetic
$AFM$	antiferromagnet, antiferromagnetic
$H$	magnetic field
$H_{EB}$	exchange field
$H_C$	coercive field
$H_{cool}$	cooling field
$H_{sw+}$	positive switching field
$H_{sw-}$	negative switching field
$T_C$	Curie temperature of the FM
$T_N$	Neel temperature of the AFM
$T_B$	blocking temperature of the AFM
$M_S/M_{FM}$	saturation magnetisation(of the FM)
$t_{FM}$	thickness of the FM layer
$t_{AFM}$	thickness of the AFM layer
$m_{vs}$	vertical hysteresis loop shift
$K_{FM}, K_{AFM}$	anisotropy constants of FM and AFM respectively
$J_{FM/AFM}$	interfacial anisotropy energy per unit area
$\Delta E$	interface anisotropy energy/unit area
$L$	AFM crystallite diameter
$Q$	quality factor
$z$	tip/sample distance
$A$	(unit) sample area
$A_{osz}$	amplitude of cantilever oscillation
$L$	AFM crystallite diameter
$c_L$	spring constant of free cantilever
$c_{eff}$	spring constant of cantilever
$f_0$	resonance frequency of free cantilever

$f_{eff}$	resonance frequency of cantilever
$\Delta f$	frequency shift
$\omega$	angular frequency
$\phi$	magnetic potential
$F_n$	force normal to a surface
$F_{exc}$	excitation force
$F_{ts}$	tip/sample interaction force
$F_z$	force in z-direction
$\sigma_{tip}(k)$	Fourier transform of a tip-equivalent surface charge pattern
$\mathbf{k}$	k-vector: $(k_x, k_y)$
$\mathbf{r}$	r-vector: $(x, y)$
$M_{rem}$	remanent magnetisation
UCS	uncompensated spins
TRM	thermoremanent magnetisation
XMCD	x-ray magnetic circular dichroism
FC, ZFC	field cooled, zero-field cooled
VSM	vibrating sample magnetometer
GMR	giant magnetoresistance
MFM	magnetic force microscopy
SFM	scanning force microscopy
DFM	dynamic force microscopy
UHV	ultra high vacuum
PLL	phase-locked loop
LTSFM	low temperature scanning force microscope
LCF	lever canting function
ICF	instrument calibration function



# Acknowledgements

This thesis would not have been possible without the cooperation and support of many collaborators and friends. I'd like to express my gratitude to all of them.

I would like to express my gratitude to Prof. Dr. Hans-Joachim Güntherodt for making this project possible and for his continuous interest in my work. Further I thank Prof. Dr. Gernot Güntherodt for being co-referee and Prof. Dr. Ernst Meyer for being the chairman of the dissertation committee.

I am especially grateful to my supervisor Prof. Dr. Hans Josef Hug for giving me the opportunity to do my Ph.D. work in his group at the University of Basel. He has not only profound knowledge in magnetism and remarkable experimental skills but is in addition an excellent teacher. In hard times he knew how to motivate and spent time and patience in discussing experiments and results.

I would like to thank all the members of the LTSFM Group: Regina Hoffman who introduced me in the deepness of the LTSFM system and Jörg Rychen who revealed me the secrets of PLLs and controllers. Peter Kappenberger for his introduction in MFM and SXM, his continuous computer support and the numerous hysteresis loop measurements he did for me at Empa. Tim Ashworth for “english support” and Nicolas Pilet.

Special thanks go to our two technicians Sacha Martin and Yves Pellmont: They always managed to fix all the broken things in the lab! In addition they built new parts if necessary, filled helium, helped with bake-out glued many things together and much more.

I would like to thank many other people from the institute of physics: Jean-Pierre Ramseyer for helping me with SEM-imaging and for knowing and finding everything that ever had existed in the institute. The people from the mechanical and electronics workshop and all the secretaries, Germaine Weaver, Audrey Fischer, Astrid Kalt and Barbara Kammermann for being so patient with us.

Furthermore I want to acknowledge all the external collaborators: Olaf Hellwig from Hitachi in San Jose (USA) and Sara Romer from Empa for the preparation of numerous samples. Magdalena Parlinska from Empa for doing excellent TEM images.

Finally I want to express my gratitude to family and friends who supported me morally

during all these long years. Special thanks and a big hug go to Peter Mühlshlegel and to my son Silvan: They patiently tolerated the endless working hours that I needed to finish this thesis and gave me the force, the motivation and the inspiration that I desperately needed.

# Scientific Publications

## **Investigation of the Exchange Bias Effect by Quantitative Magnetic Force Microscopy**

P. Kappenberger, I. Schmid and H. J. Hug  
*Adv. Eng. Mater.*, 7(5): 332-338, 2005.

## **The role of uncompensated spins in exchange biasing**

I. Schmid, P. Kappenberger, O. Hellwig, M. J. Carey, E. E. Fullerton and H. J. Hug  
*Europ. Phys. Lett.*, 81: 17001-17005, 2008.

## **Observation of the coupling of ferromagnetic spins to antiferromagnetic spins on the single grain scale**

I. Schmid, P. Kappenberger, S. Romer, M. Parlinska, O. Hellwig, M. J. Carey, E. E. Fullerton and H. J. Hug  
*In preparation*

## Contributed Talks

### **High Resolution Imaging and Determination of the Uncompensated Spin Density in Exchange-Biased FM/AF thin Films**

I. Schmid, P. Kappenberger and H. J. Hug  
*NC-AFM*, Seattle, USA 2004.

### **The Role of Uncompensated Spins in Exchange Biasing**

I. Schmid, P. Kappenberger, S. Romer, M. Parlinska, O. Hellwig, M. J. Carey, E. E. Fullerton and H. J. Hug  
*JEMS*, San Sebastian, Spain 2006.

### **Observation of the Coupling of Ferromagnetic Spins by Antiferromagnetic Spins with a Spatial Resolution of Single Grains**

H. J. Hug, I. Schmid, P. Kappenberger, S. Romer, M. Parlinska, O. Hellwig, M. J. Carey and E. E. Fullerton  
and

**The Role of Uncompensated Spins in Exchange Biased Systems**

I. Schmid, P. Kappenberger, S. Romer, M. Parlinska, O. Hellwig,  
M. J. Carey, E. E. Fullerton and H. J. Hug  
*Intermag*, San Diego, USA 2006.

**The Role of Uncompensated Spins in Exchange Biasing**

I. Schmid, P. Kappenberger, S. Romer, M. Parlinska, O. Hellwig,  
M. J. Carey, E. E. Fullerton and H. J. Hug  
*NSS4*, Rathen, Germany 2006.

# Curriculum Vitae

## Iris Schmid

Born on August 30th 1975 in Frutigen, Switzerland.

06/2002-04/2006	Ph.D. thesis in the group of Prof. Dr. H. J. Hug and Prof. Dr. H.-J. Güntherodt at the University of Basel, Switzerland.
07/2001-05/2002	Language courses and travelling in South America
10/1996-07/2001	Studies of Physics at the University of Basel.
1994-1996	Gymnasium section C at the “Gymnase Cantonal de Neuchâtel”.
1991-1994	Business school, “Ecole supérieure de Commerce” in La Neuveville.
1982-1991	Primary and secondary school in Frutigen.

The following Professors have contributed to my education:

- Basel Ph.D.: H. J. Hug, E. Meyer, M. Hegner, H.-J. Güntherodt.
- Basel studies: I. Sick, C. Schönenberger, P. Oelhafen, E. Meyer, H.J. Hug, L. Tauscher, C. Bruder, F.-K. Thielemann, D. Trautmann, D. Loss, A. Bussmann-Holder, J. Jourdan, G. Tammann, B. Binggeli, R. Buser, H. Kraft, D. Masser, C. Bandle.